Electronic Theses and Dissertations   Theses, Dissertations, and Major Papers

10-19-2015

Wear Mechanism Maps for Magnesium Alloy AM60 and Composite AM60-9% (Al2O3)f

Muhammad Zafar Ullah Khan
University of Windsor

Follow this and additional works at: https://scholar.uwindsor.ca/etd

Wear Mechanism Maps for Magnesium Alloy AM60 and Composite AM60-9% (Al$_2$O$_3$)$_f$

By

Muhammad Zafar Ullah Khan

A Thesis

Submitted to the Faculty of Graduate Studies

through Engineering Materials

in Partial Fulfillment of the Requirements for

the Degree of Master of Applied Science at the University of Windsor

Windsor, Ontario, Canada

2015

Wear Mechanism Maps for Magnesium Alloy AM60 and Composite AM60-9% $(Al_2O_3)_f$

By

Muhammad Zafar Ullah Khan

APPROVED BY:

_____

D. Green, Outside Program Reader
Department of Mechanical, Automotive & Materials Engineering

_____

H. Hu, Program Reader
Department of Mechanical, Automotive & Materials Engineering

_____

A.T. Alpas, Advisor
Department of Mechanical, Automotive & Materials Engineering

October 2, 2015

DECLARATION OF ORIGINALITY

I hereby certify that I am the sole author of this thesis and that no part of this thesis has been published or submitted for publication whatsoever all across engineering lines.

I certify that, to the best of my knowledge, my thesis does not infringe upon anyone's copyright nor does it violate any proprietary rights and that any ideas, techniques, quotations, or any other material from the work of other people included in my thesis, published or otherwise, are fully acknowledged in accordance with the standard referencing practices. Furthermore, to the extent that I have included copyrighted materials that surpasses the bounds of fair dealing within the meaning of the Canada Copyright Act. I certify that I have obtained a written permission from the copyright owner(s) to include such material(s) in my thesis and have included copies of such copyright clearances to my appendix. I truly declare that this is a genuine copy of my thesis, including any final revisions, as approved by my thesis committee and the Graduate Studies office, and that this thesis has not been submitted for a higher degree to any other University or Institution all across the world.

ABSTRACT

The purpose of this work was to study the tribological behaviour of squeeze cast Mg alloy AM60 and its composite AM60-9% $(Al_2O_3)_f$. Dry sliding wear tests were performed on specimens of these materials using a block-on-ring tribometer which was equipped with a COF and temperature measurement system. Wear, COF and temperature maps were constructed to illustrate the effect of temperature and COF on the wear behaviour of the Mg alloy and it's composite.

Four wear regimes namely low, mild, transient and severe wear were identified. The transition from mild to severe wear regime was found to be dependent on the bulk temperature of the specimen. Oxidational wear prevailed in low and mild wear whereas plastic deformation induced wear and melt wear controlled the wear rates in transient and severe wear regimes, respectively. This study shows that the incorporation of Al_2O_3 fibres in AM60 alloy improved the wear resistance of the resulting composite by delaying the transition from mild to severe wear.

DEDICATION

To my parents,

Muhammad Razi Ullah Khan and Saeeda Khan,

and my siblings

for their love, encouragement and support throughout.

ACKNOWLEDGEMENTS

Table of Content

List of Tables

List of Figures

xiv

Chapter 1: Introduction

1.1 Background

The reduction in the weight of vehicles, which directly results in the reduction of fuel consumption, has been one of the main foci of the automotive industry. The use of lightweight materials is the most effective way of reducing fuel consumption and air pollution. Lightweight metals like aluminum and magnesium are considered as suitable materials to replace steel and cast iron which were primarily used to manufacture the vehicle body and powertrain systems[1]. The use of magnesium in the powertrain systems has been of great interest as it has been shown that the use of magnesium in the powertrain system helps to reduce the weight of an automotive body by more than 40% compared to cast iron [2-4]. Mg alloys exhibit creep resistance, castability and resistance to hot-cracking which makes them suitable for use in small hybrid engines [5]. Poor wear resistance poses a great hindrance to the use of magnesium alloys in automotive powertrain applications. Tribological properties of Mg alloys can be improved by tailoring the surface topography and composition and also by the addition of particulate and/or fibre reinforcements to the alloy [6-9].

1.2. Objectives of Current Research

A wear database is required by engineers and designers to forecast the wear behaviour of materials intended to be used for manufacturing of automotive engine blocks. However, there is a lack of such database for Mg based composites, despite their promising performance in such applications. This thesis presents the research work carried out to determine the tribological behaviour of magnesium alloy AM60 and a composite with

AM60 alloy matrix reinforced with Al_2O_3 (AM60-9%$(Al_2O_3)_f$) under dry sliding conditions.

1.3 Scope of this work

1. Construction of wear map for AM60 alloy and AM60-9%$(Al_2O_3)_f$ composite showing the various wear regimes under dry sliding conditions.

2. To investigate the microstructural changes corresponding to each wear regime and to investigate the wear mechanisms operating in each wear regime as shown in the wear map.

3. To determine how transition occurs between two wear regimes by considering changes in wear rates, coefficient of friction values, subsurface temperatures and surface roughness.

4. To provide a wear database and to facilitate designers and engineers to predict the tribological behaviour of Mg alloy and its composite under oil starvation conditions.

The scope of this work includes the characterization of Mg (AM60 alloy) matrix and its composite with 9% reinforcement (Al_2O_3fibre) fabricated using preform and squeeze casting techniques. It also includes construction of wear map for AM60 alloy and its composite indicating various wear regimes and corresponding wear mechanisms in operation that are responsible for the characteristic microstructural features which are particular to the respective wear mechanisms.

1.4 Organization of the Thesis:

This thesis comprises of five chapters, the contents of which are briefly described below:

Chapter 1 provides a brief introduction by providing a short perspective of the background and scope of the work.

Chapter 2 provides a review of the work that has already been published on the tribological properties of Al and Mg (composites and alloys). The chapter starts with a description of strengthening mechanisms in alloys and metal matrix composites, followed by a survey of fabrication processes that can be employed to produce metal matrix composites along with their merits and demerits. The evolution of the wear mapping approach and its effectiveness in describing the tribological behaviour of materials has also been stated. The chapter is then focused on description of the wear mechanisms exhibited by Mg alloys and composites subjected to dry and lubricated sliding under different sliding conditions.

Chapter 3 describes the experimental methodology used in this research work. First, the squeeze casting technique employed to produce the AM60-9%$(Al_2O_3)_f$ composite is described. This is followed by the metallographic characteristics of AM60 alloy and AM60-9%$(Al_2O_3)_f$ composite used for this research work. A description of the block-on-ring tribometer and the test parameters used in this work has been provided.

Chapter 4 states the results of the wear tests conducted on AM60 alloy and AM60-9%$(Al_2O_3)_f$ composite. The tribological properties of the two materials have been compared in detail along with the discussion of the effect of load on the wear of the two materials followed by the wear maps for the respective materials.

Chapter 5 is the discussion of the wear mechanisms identified on the wear map for AM60 alloy and AM60-9%$(Al_2O_3)_f$ composite. The effect of temperature on the

transition from mild to severe wear has been explained in detail. A detailed analysis of

the characteristics of transient wear has also been given.

Chapter 2: Literature Survey

2.1. Introduction to this survey

This chapter reviews previous studies conducted in order to investigate the dry sliding behaviour of metals. It also accounts for the evolution of wear mapping approach to explain the tribological properties of metals under dry and lubricated sliding conditions. The studies carried out on the manufacturing aspects of Mg alloy and Mg-based composites are summarized and the effects of manufacturing processes on microstructures of Mg alloy and composites are described prior to a review of their tribological behaviour. The phenomena of wear transitions and their relevance for wear mechanism maps are reviewed. Also, temperature maps are described as a tool to complement the wear mechanism maps.

2.2. Necessity of lightweight materials

A lot of research work is being done to develop light-weight materials such as non-ferrous materials (Al, Mg) for engine and powertrain materials as a suitable alternative to current heavy-weight cast iron blocks [10,11]. Due to the poor wear resistance of aluminum, the use of cast iron sleeves is required which adds to the cost of engine block [12]. The use of aluminum alloy 390 in manufacturing monolithic cylinder blocks is, however, an exception [13]. Researchers are, therefore, presently developing Al-Si alloys[14], Mg composites [15,16] and wear resistant coatings on piston skirts and aluminum cylinder bores for alternatives [17,18].

2.3. Use of Mg in automotive applications

Magnesium, with a density of 1.74 g/cm^3 is one of the lightest of engineering materials. Mg is 35% lighter than aluminum and 78% lighter than steel [19].Magnesium is rarely

used in engineering applications in its pure form as it can be strengthened by adding alloying elements like aluminum, manganese, zinc, thorium or zirconium [20,21]. The American Society for Testing Materials has developed a method for designating Mg alloys in which the first two letters indicate the principal alloying elements according to the following code:A—aluminium; B—bismuth; C—copper; D—cadmium; E—rare earths; F—iron; G—magnesium; H—thorium; K—zirconium; L—lithium; M—manganese; N—nickel; P—lead; Q—silver; R—chromium; S—silicon; T—tin; W—yttrium; Y—antimony; Z—zinc [22].The first letter corresponds to the element present in greater quantity e.g. AZ91 indicates the alloy Mg–9Al–1Zn. Mg-Zr alloys are not sufficiently strong for commercial applications. Therefore , addition of other alloying elements is necessary. The selection of these elements depends on the compatibility of these materials with Zr which implies the absence of elements such as Al and Mn that effectively suppress the liquid solubility of zirconium in Mg. Among Zirconium-free casting alloys, Mg-Al alloys are most widely used. In the as-cast condition, the β-phase $Mg_{17}Al_{12}$ appears in the form of network around the grain boundaries in alloys containing more than 2% Al while ductility decreases rapidly above 8% Al. Mg-Al alloys have good castability, satisfactory corrosion resistance and can be used at temperatures up to 110–120°C above which creep rate becomes unacceptable.This behaviour is attributed to the fact that magnesium alloys undergo creep mainly by grain boundary sliding and the phase $Mg_{17}Al_{12}$,which has a melting point of approximately 460 °C. However, magnesium alloys do not possess mechanical properties, like hardness, yield strength (YS) and Young's modulus that may enable them to replace aluminum and steel in powertrain applications. Luo [23] fabricated Mg matrix composites by adding preheated SiC

particulate (10 vol%) to molten commercially pure AZ91 alloy. Tensile tests were done to determine mechanical properties like Young's modulus, tensile strength, yield strength and elongation to failure, while Scanning Electron Microscope (SEM) was used to analyze the fracture surfaces. The improvement noted in the mechanical properties of the unreinforced alloy matrix (AZ91) due to the addition of SiC particles are summarized in table 2-1, which shows a significant increase (56%) in the yield strength and a slight increase (5%) in the Young's modulus of the composite over the unreinforced magnesium alloy. However, a decrease in the UTS of the composite is noticed as compared to that of the unreinforced magnesium alloy. Hu [24] employed squeeze casting technique for the fabrication of AZ91 alloy and its composite AZ91/SiC. It was observed that the use of squeeze casting technique improved the mechanical properties of AZ91 in comparison with other casting techniques, like sand casting, gravity die-casting and pressure die-casting, which were further improved by reinforcing AZ91 with SiC particles. In as-cast condition, squeeze cast AZ91 showed an improvement in UTS of up to 25 % (200 MPa) in comparison with sand cast AZ91 (154 MPa). Yield strength was improved by 18 % (115 MPa) in comparison with sand cast AZ91 (83 MPa). Zhang et al. [25] fabricated hybrid composites $((Al_2O_3)_f +(Al_2O_3)_p /AM60)$ by preform-squeeze casting process in which the liquid magnesium alloy AM60 was infiltrated into preform under an applied pressure of 90 MPa. The mechanical properties evaluation indicates that reinforcing AM60 alloy with Al_2O_3 fibres and particles improved elastic modulus, tensile strengths and hardness in comparison to the matrix alloy. In particular, the elastic modulus, yield strength (150 MPa) of the hybrid composite was observed to be 88% higher than that of the matrix alloy. With almost no increase in density, the elastic

modulus of the hybrid composite (59 GPa) showed 40% improvement over the matrix alloy (40 GPa). The UTS (199 GPa) was 16 % higher than that of the unreinforced AM60 alloy.

2.3.1. Strengthening mechanism in Mg based composites

The increase in strain hardening behaviour of AZ91 (Mg-9Al-0.9Zn) alloy reinforced with SiC is the basic strengthening mechanism in comparison to that of the unreinforced AZ91 alloy. When considering the as-cast composite, the microstructure consists of a eutectic phase ($Mg_{17}Al_{12}$) and the hard reinforcing SiC particles. The SiC particles have an elastic modulus and fracture strength of 440 GPa and 2000 MPa, while AZ91 matrix alloy has an elastic modulus and fracture strength of 42.7 GPa and 203 MPa. The intragranular and intergranular SiC particles may constrain the slip behaviour of the Mg-grains as the particles, along with the eutectic β phase ($Mg_{17}Al_{12}$), may act as barriers to the slip lines (Figure 2.1) increasing the strain hardening rate and yield strength of the composite. Another study on SiC reinforced Al (A356) matrix composite [26] showed that the distribution of the internal stress is complicated and usually creates triaxiality of the real stress state in the composite material depending on the particle distribution, particle size, matrix grain size, and relative strength of the particle to the metal matrix. The high strain hardening rate of the composite is due to the triaxiality of internal stresses. In cases where these localized (internal and applied) stresses are sufficiently high, localized damage, in terms of particle/matrix cracking and interfacial debonding, occurs. The fracture of the composites occurs as a result of these local damages. A significant number of SiC particles were located within the primary Mg grains, which suggests that heterogeneous nucleation of primary magnesium on SiC particles serves as

the primary grain refinement mechanism, thereby reducing the grain size by a factor of 3 as shown in figure 2.2 [23, 27]. The presence of SiC particles around primary Mg also restricts the grain growth. So the SiC particles acting as barriers for the grain growth can also be attributed as a grain refinement mechanism which provides sufficient time for the melt to generate more nuclei, leading to smaller grain size in the finally solidified microstructure.The grain refinement resulting from the above described mechanisms contribute to the strengthening of the composite material by the grain boundary strengthening mechanism as described by the relationship between yield stress(σ_o) and grain size (D) using Hall-Petch equation[28,29]:

$$\sigma_o = \sigma_i + kD^{-1/2} \tag{2.1}$$

where σ_o is the yield stress, σ_i is the friction stress, k is the dislocation locking parameter and D is the grain diameter.

Grain refinement process similar to AZ91 reinforced with SiC, was observed in a composite with anAM60 matrix alloy reinforced with Al_2O_3fibres [30], due to nucleation of the eutectic phase($Mg_{17}Al_{12}$) on the reinforcement fibres. Zhang et al. [31] studied the effect of different cooling rates using sections with different thicknesses as shown in figure 2.3. The effect of different cooling rates on the microstructural evolution of AM60 alloy is shown in figure 2.4. It was shown that decreasing the section thickness of the casting increases the cooling rate, which results in finer grains. In another study [32], AM50A alloy was shown to undergo supercooling of about 0.9 °C to reduce the grain size as shown in figure 2.5. Upon reinforcement of AM50A alloy matrix with SiCparticles, finer grains were produced without any significant amount of supercooling as shown in figure 2.6.

The various possible strengthening mechanisms include i) load transfer mechanism; ii) matrix strengthening due to grain size reduction iii) Orowan mechanism and iv) increase in dislocation density due to geometrical and thermal mismatch. The shear lag model (Figure 2.7) [29,33,34] assumes that fibres are the principal load carriers and the load transfer occurs between the reinforcement and the matrix via shear stress at the reinforcement-matrix interface. Assuming uniform matrix deformation, the flow stress σ_{LT} necessary for composite deformation due to load transfer is calculated by Eqn.2.4. The strengthening component depends on the reinforcement volume fraction in the following way [29]:

$$\Delta\sigma_{LT} = \sigma_m\, 0.5_f \qquad (2.2)$$

Due to the difference in thermal properties of the fibre and matrix, a strain mismatch is generated as the composite is cooled from a higher processing temperature. This strain mismatch leads to the generation of new dislocations at the fibre-matrix interface. In short, the dislocation density increases upon cooling in a composite. The new dislocation density and corresponding strengthening may be calculated using Eqn.2.5 [33].

$$\rho_T = \frac{Bf\Delta f\Delta\alpha}{b(1-f)}\frac{1}{t\prime} \qquad (2.3)$$

where t` is the minimum size of the reinforcing phase particles, b is the magnitude of the Burgers vector of the newly created dislocations, B is a geometrical constant, $\Delta\alpha$ is the difference between the two thermal expansion coefficients and ΔT is the temperature variation. On the other hand, geometrically necessary dislocations (GND) are also generated upon the addition of the reinforcement phase as these geometrically necessary dislocations accommodate the mismatch in plastic deformation of the matrix. The density of geometrically necessary dislocation may be calculated by [34]:

$$\rho g = \frac{f\,8\,\varepsilon_p}{bt} \tag{2.4}$$

where ε_p is plastic strain. Apart from thermally formed and geometrically necessary dislocations, the introduction of the reinforcement phase also induces the generation of dislocations stored in the reinforcement phase. Hence, the total dislocation density in a composite is given by Eqn.2.7 [34].

$$\rho_{total} = \rho_t + \rho_G + (\rho_S + \rho_a) \tag{2.5}$$

where ρ_s is the statistically stored dislocation density in an unreinforced matrix and ρ_a is the diminished part of the statistically stored dislocations due to the addition of a reinforcing phase. Closely-spaced hard alumina fibres and dislocation pile-ups in the vicinity of fibres provide resistance to dislocation motion. The resultant strengthening due to this mechanism may be calculated as follows:

$$\Delta\sigma_{OR} = \frac{Gb}{\Lambda} + \frac{5}{2\pi}Gf\varepsilon_p \tag{2.6}$$

where Λ is the distance between fibres and ε_p is plastic deformation. Due to large interfacial spacing and coarse particles in composites, Orowan strengthening [34] is generally not considered as a significant strengthening mechanism. At higher temperatures, stresses can attain yield stress and the composite undergoes plastic deformation owing only to temperature cycling. The thermal stress in the fibre-matrix interphase may be calculated by:

$$\Delta\sigma_{TS} = \frac{E_f E_m}{(E_f f + E_m(1-f))} f \Delta\alpha\Delta T \tag{2.7}$$

Wwhere E_f and E_M are Young's moduli of the reinforcing phase (fibres or particles) and the matrix, , respectively. The thermal stress is dependent on the distance from the fibre

and decreases with distance from the fibre (or particle). Volume-averaged residual stresses in the matrix reach their maximum value($<\sigma_m>_{max}$):

$$< \sigma_m >_{max} = \frac{2}{3}\sigma_y \ln(\frac{1}{f})\frac{f}{1-f} \tag{2.8}$$

where σ_y is the yield stress of the matrix.

At elevated temperatures, the probability of dislocation climb increases which causes variation in the flow stress of the composite. Moreover, thermal softening at elevated temperatures occurs due to dislocation motion as a result of cross-slip and dislocation climb [33,34].

In summary, it has been described that the flow stresses of the composites are substantially higher than those of the unreinforced alloy. Load transfer from matrix to reinforcement phase due to shear stresses at the fibre-matrix interface was significant in the fibre reinforced composite. On the other hand, in the particle-reinforced composites, small grain size plays a predominant role. The increment in dislocation density owing to the resultant thermal and geometrical mismatch is also important while considering the strengthening of the matrix.

Table 2-1. Tensile properties of AZ91 alloy and AZ91/SiC composite [16,18].

Material	Elastic Modulus (GPa)	0.2% Yield Strength (MPa)	UTS (MPa)	Elongation %
AZ91	42.6	86.7	203	7.1
AZ91/SiC	44.7	135	152	0.8
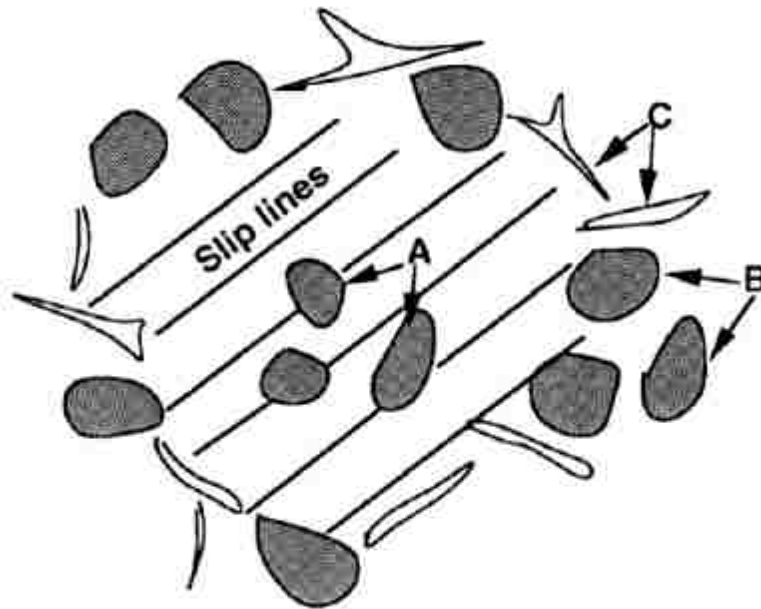
A - intragranular SiC particles
B - intergranular SiC particles
C - eutectic β phase ($Mg_{17}Al_{12}$)

Figure 2.1.Schematic diagram showing the particle-matrix interaction in the AZ91/SiC composite [23,27].
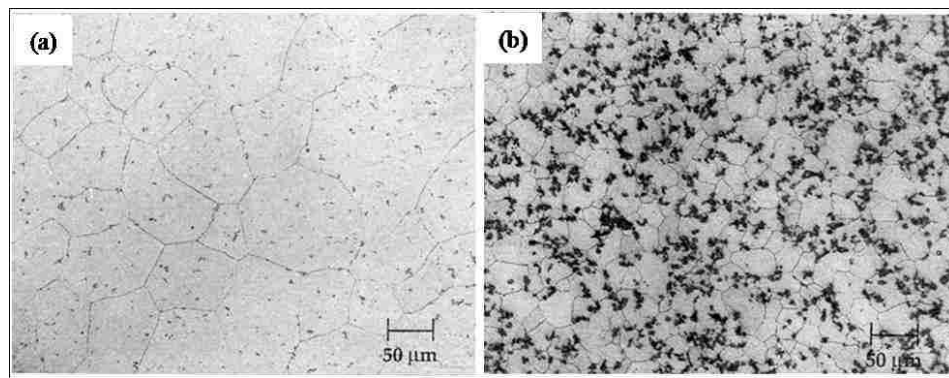
Figure 2.2.Optical micrographs of (a) unreinforced AZ91 alloy and (b) AZ91/SiC composite [23,27].
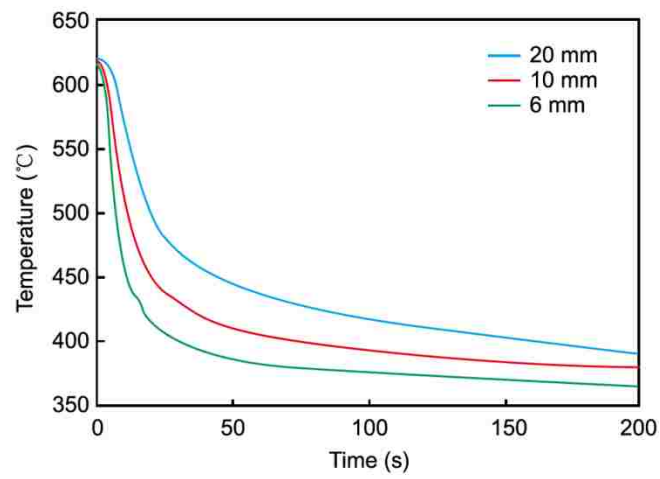
Figure 2.3.Cooling curves of samples with 6, 10 and 20 mm thick sections [31].
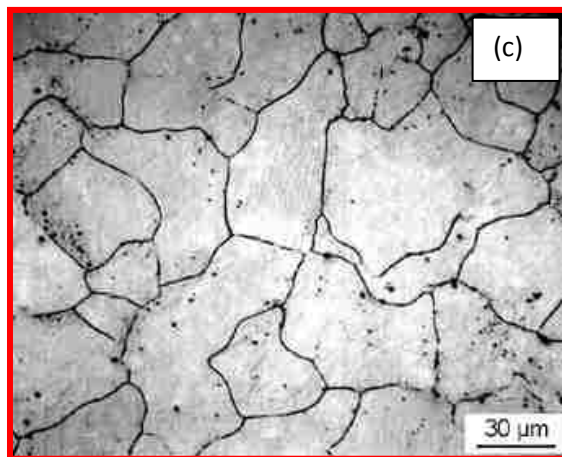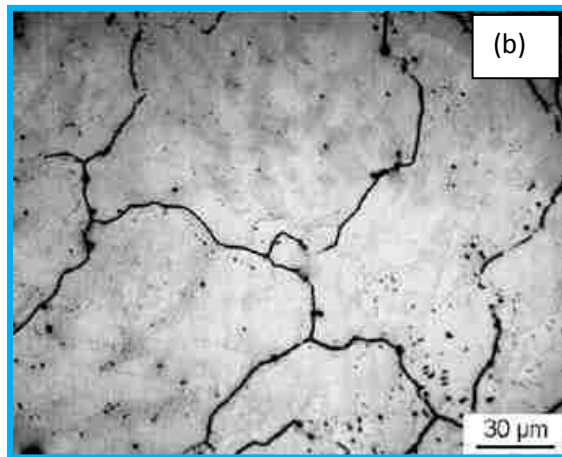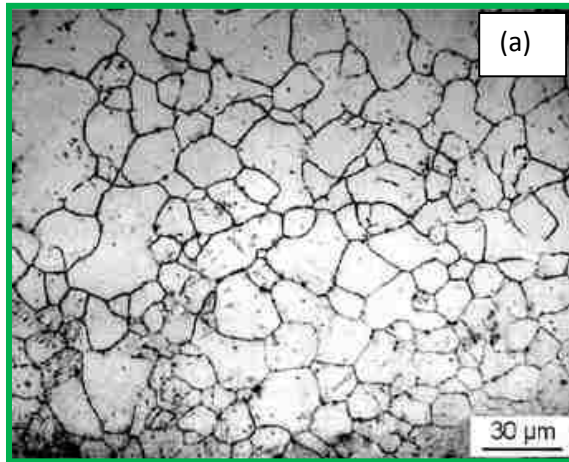
Figure 2.4. Optical micrograph showing grain size of specimens with (a) 6 mm, (b) 10 mm and (c) 20 mm section thickness [31].
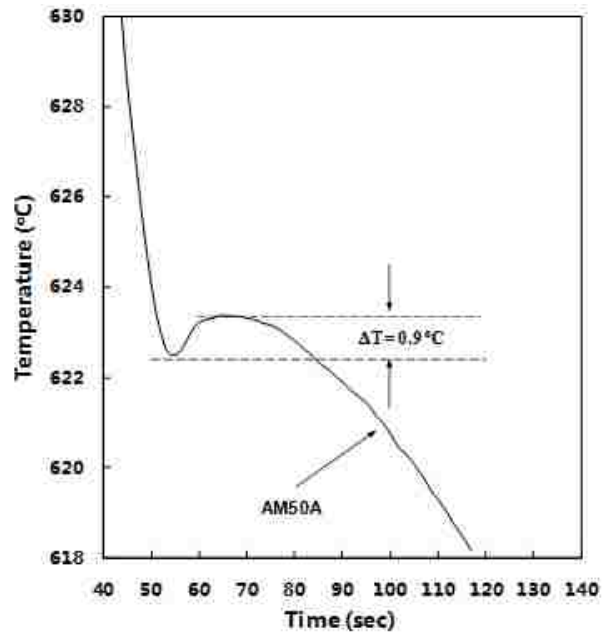
(a)
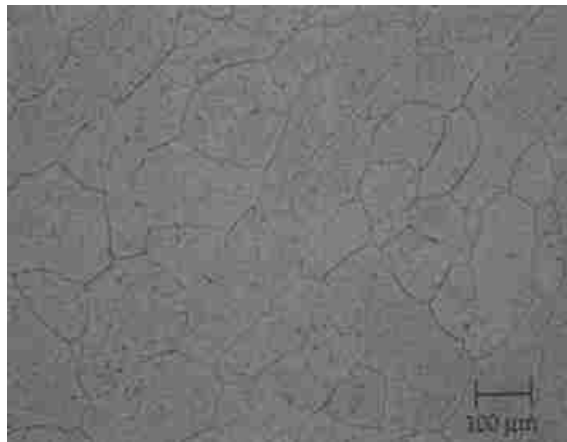
(b)

Figure 2.5.(a) Enlarged liquidus temperature region of AM50A (b)Optical micrograph showing grain structure of AM50A alloy [32].
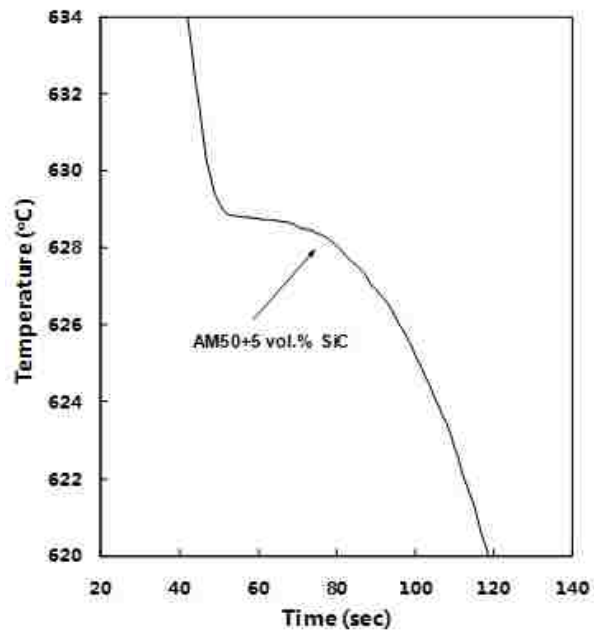
(a)
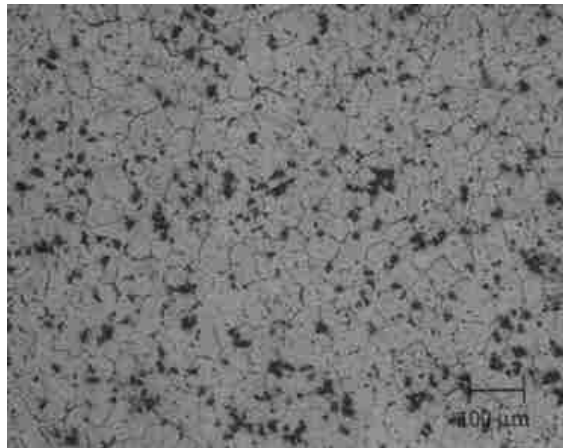
(b)

Figure 2.6.(a) Enlarged liquidus temperature region of AM50A/SiC$_p$ composite (b) Optical micrograph showing grain structure of AM50A/SiC$_p$ composite in T4 condition [32].
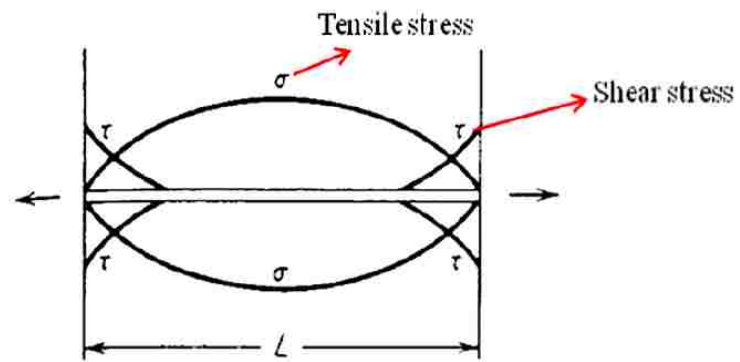
Figure 2.7. Variation of stress along a fibre in a fibre reinforced composite [29].

2.4. Fabrication of Metal Matrix Composites (MMCs)

Conventional methods for the fabrication of magnesium matrix composites are similar to aluminum matrix composites. There are 3 conventional methods that are predominantly used for the processing of magnesium matrix composites [35]:

1. Stir casting

2. Squeeze casting

3. Powder metallurgy

2.4.1. Stir casting

Stir casting process involves uniformly distributing the reinforcing phase into molten magnesium by means of mechanical stirring [36]. Different steps involved in a stir casting process are shown in figure 2.8 [37]. The metal and the reinforcement particles are preheated and charged into a furnace where the mixture is heated above the liquidus temperature of the matrix. At this point, metal stirring is done to uniformly distribute the reinforcement particles in the molten matrix. Mechanical stirring is the most important step of this process because the uniformity of the particle distribution, which is critical for achieving a high strengthening effect, depends on it. Finally, the mixture is poured into a mold to give a certain shape to the composite.

A further development in the stir casting process was suggested by Zhou et al. [38] in which A356 aluminum alloy was reinforced with SiC particles via stir casting in a two-step mixing process. In this process, the metal matrix is completely brought into its molten state initially by heating it up above the liquidus temperature after which it is cooled down to a temperature between liquidus and solidus points. This makes the metal to get into a semi-solid state at which particles are added and mixed into it. The mixture

is again heated up above the melting point of matrix and the particles are thoroughly mixed into the molten liquid. The molten mixture is then transferred into a mold and is also solidified to give a certain shape to the composite. Magnesium composites with various matrix compositions, such as AZ31, Z6 [39], CP-Mg (chemically pure magnesium) [40], ZC63 [41], ZC71 [42], and AZ91 [43], have been produced using this method.

2.4.2. Squeeze casting

The squeeze casting process involves making a preform out of the reinforcement. The preform is then placed into a casting mold into which the molten matrix is added and solidified under high pressure. The different steps involved in a squeeze casting process are illustrated in figure 2.9 [44].The application of pressure induces several unique phenomena which affect the microstructure and mechanical properties of the resulting composite[35]. These phenomena are discussed as follows:

1. High-pressure reduces the freezing temperature of the composite. According to the Clausius-Clapeyron equation (Eq. 2.9) the solidifying temperature of an alloy depends on the amount of pressure applied, the difference in its liquid and solid specific volumes, and solidification latent heat. It was found that the eutectic temperature and composition of Al-Si alloy was changed from 660°C and 12.6% Si to 613°C and 17.4%Si respectively at 1300MPa [45].

$$\frac{dT}{dP} = \frac{T_f(V_s - V_l)}{L_f} \tag{2.9}$$

2. Due to high applied pressure, the closer contact between the mold walls and the solidifying surface increases the cooling rate due to the enhanced heat transfer. It

has been found that the cooling rate was increased from 11°C/s for permanent mold casting to 282°C/s for squeeze casting [46].

3. Shrinkage upon solidification, which poses a problem in conventional casting processes, is compensated in squeeze casting process at high temperature. Hence, a squeeze cast material has finer grains which improve the mechanical properties of the composite. For example, an increment of 15 to 40% in the tensile strength and hardness was shown in case of Mg-4.2% Zn Rear Earth (RE) alloy reinforced with alumina fibres produced using squeeze casting process as compared to that produced using permanent mold casting [47].

2.4.3. Powder metallurgy

In the powder metallurgy process, powdered metal matrix and reinforcement particles are mixed, pressed, degassed and sintered at a certain temperature in a protective environment. The steps involved in a powder metallurgical process are shown in figure 2.10 [48]. The major disadvantage of this process is the high cost of the metallic powder used.

A comparison of the above discussed processes is shown in table 2-2 [48]. The volume fraction of the reinforcement that can be added in each of these processes is limited to 30% for stir casting and 40 to 50% for squeeze casting while the volume fraction of the reinforcement for powder metallurgy is not limited. Castings of any shape can be produced through stir casting while it is limited in case of squeeze casting and powder metallurgy method due to the preform shape and size of the product.
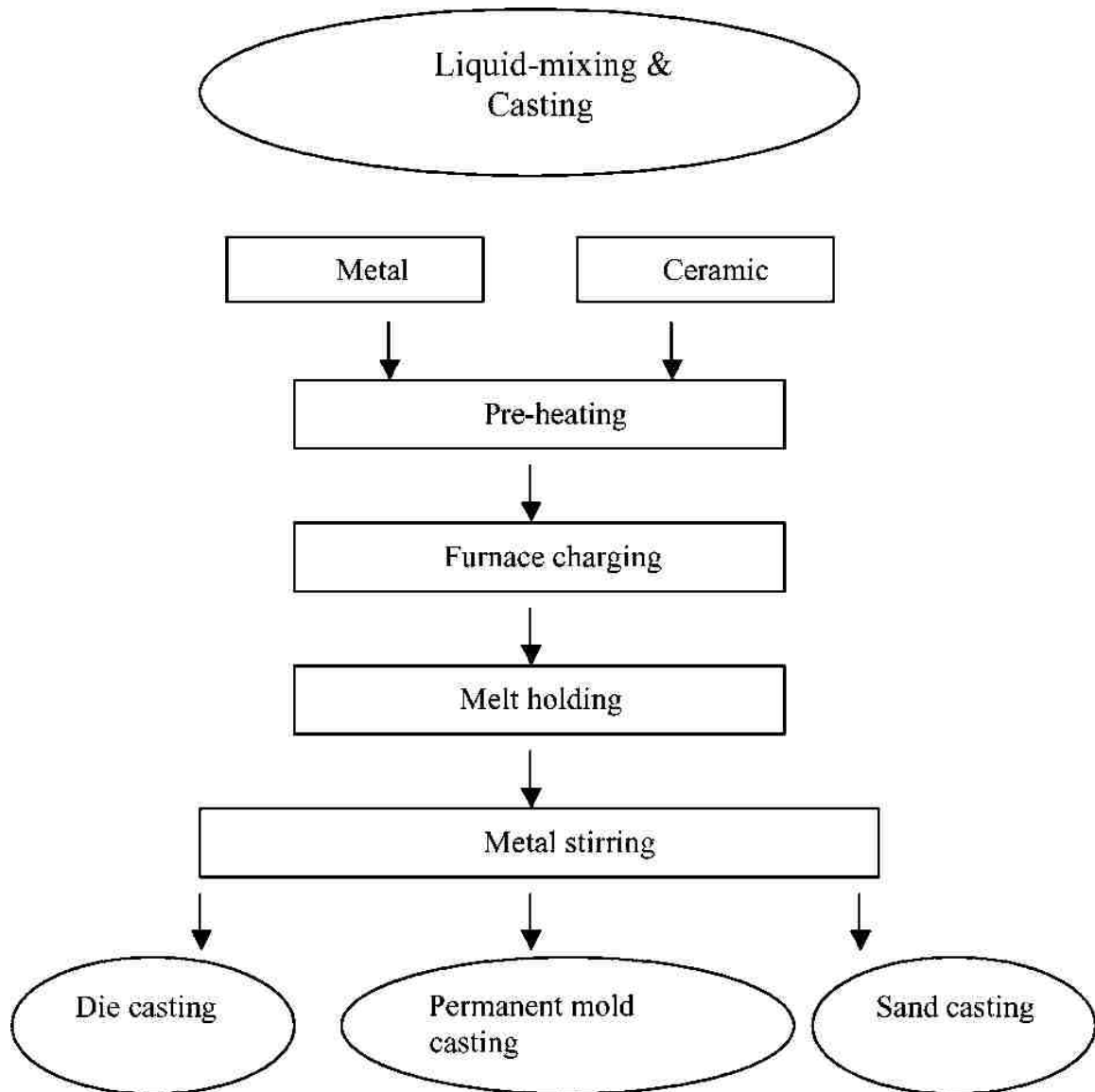
Figure 2.8.Flowchart of stir casting process [37].
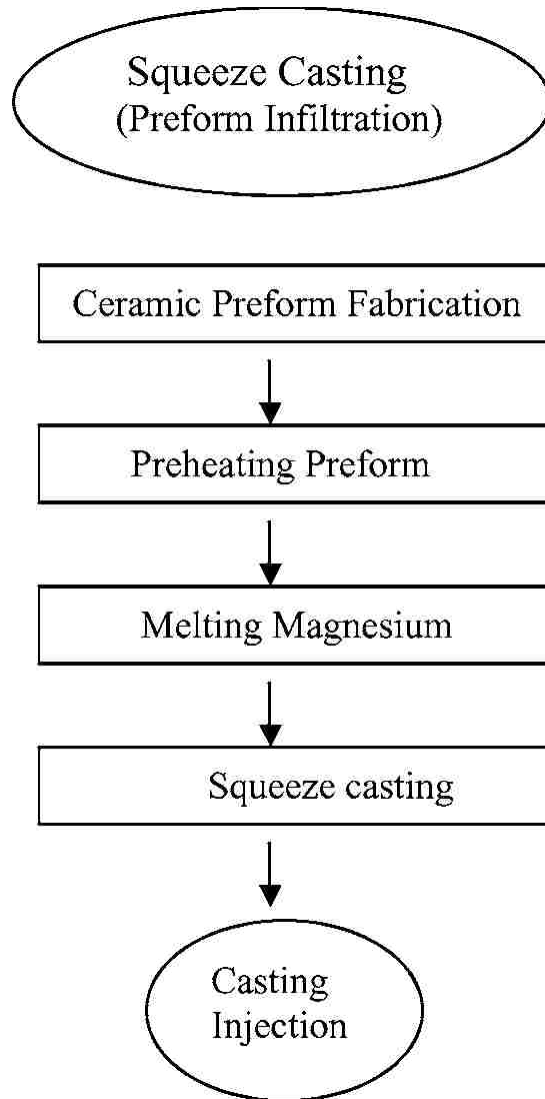
Figure 2.9.Flowchart of squeeze casting process [44].
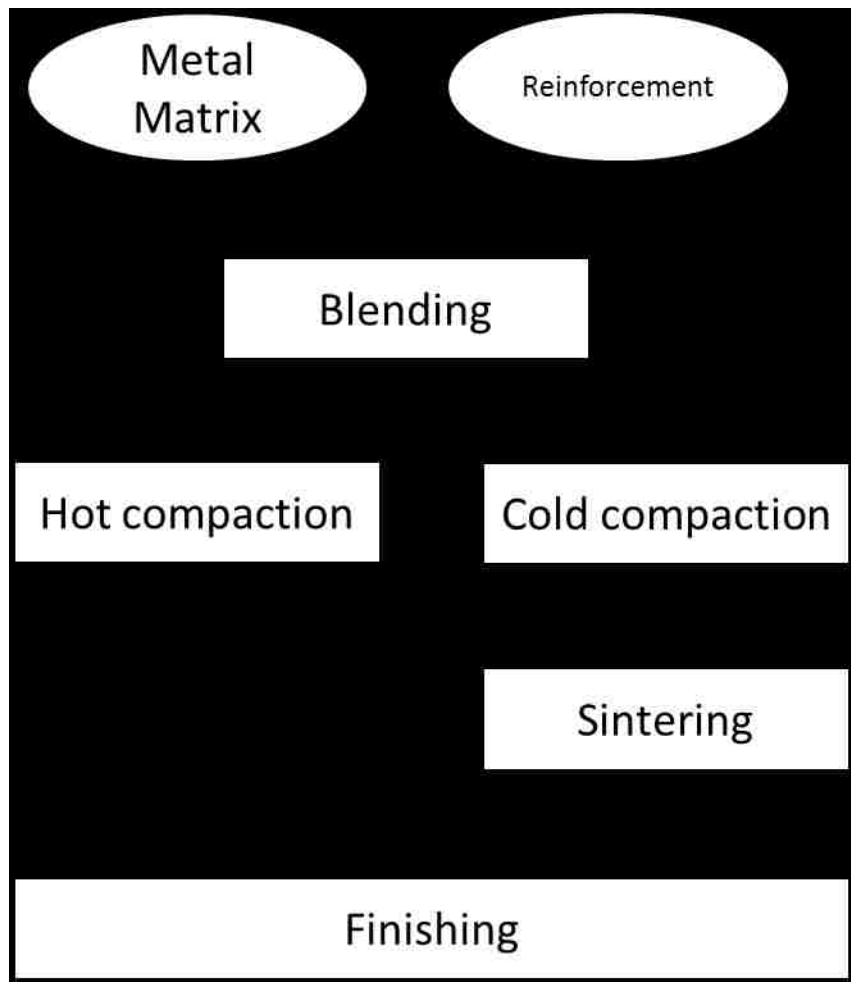
Figure 2.10.The process of powder metallurgy [48].

Table 2-2. Comparison of stir casting, squeeze casting and powder metallurgy [48]

Method	Working range	Metal yield	Reinforcement fraction (vol%)	Fabrication cost
Stir casting	Wide range of shape, larger size (up to 500 kg)	Very high, >90%	~30	Least expensive
Squeeze casting	Limited by preform shape, (up to 2 cm height)	Low	~45	Moderately expensive
Powder metallurgy	Wide range, restricted size	High	-	Expensive

2.5. Wear mapping approach

2.5.1. Wear transitions and wear mapping approach for ferrous and non-ferrous materials

Wear is defined [ASTM G40] as "damage to a solid surface, generally involving progressive loss of material due to relative motion between the surfaces and a contacting substance or substances." Further, ASTM G40 defines sliding wear as "wear due to the relative motion in the tangential plane of contact between two solid bodies." The damage due to sliding is caused to both of the sliding bodies,which is evident on the adjacent sliding surfaces of the two bodies. As the two surfaces slide together, another phenomenon besides wear, namely friction, occurs [49].

In 1955, Archard and Hirst [50], showed the variation of wear with time for a number of materials undergoing sliding wear using pin on ring configuration when the pin and ring were each of the same or of different materials. After an initial transitional period, a constant wear rate was observed in the mild wear regime. Once the equilibrium condition is attained, the wear rate was found to be independent of the apparent area of contact for a wide range of materials. Figure 2.10 shows the volume of the material removed against sliding distance curves for ferritic stainless steel pins slid against hardened tool steel rings at speed of 1.8 m/s for loads ranging from 80 g to 2000 g. From the slopes of these plots, equilibrium wear rates were obtained which were plotted against the applied load as shown in figure 2.11. It is observed that the materials exhibit two forms of wear, mild, at lighter loads, and severe, at heavier loads. A sharp increase in the wear rate was observed as the load was increased which was identified as the transition from mild to severe wear. The subsurface damage caused by the two different forms of wear was also

distinguishable as shown in figure 2.12. Figure 2.12 (a) shows the cross-sectional microstructure of the worn surface indicating small subsurface damage in the mild wear regime while larger deformation of the subsurface region was observed in the severe wear regime as shown in figure 2.12 (b). An empirical rule was established as follows:

$$W = \frac{KL}{H} \qquad (2.10)$$

where W is the volume worn per unit distance, L is the normal load, K is the coefficient of wear and H is the hardness of the softer surface. The value of the coefficient of wear 'K' determines the severity of the damage caused by wear is shown in table 2-3 for various materials at a constant load of 400 g. The value of K is not dependent on the applied load but on the material used its hardness and surface condition. The deficiency of Eqn. 2.9 is that it only incorporates hardness as a material parameter.

In order to study the complex phenomena of wear in a more effective way, Tabor [51] suggested the construction of wear mechanism maps to summarize the data and models of wear, identifying the boundaries of the dominant wear mechanisms. Lim and Ashby [52] constructed an empirical wear mechanism map for steel which defined various wear mechanisms as shown in figure 2.13. The map shows the dominant mechanisms on a normalised pressure vs. normalised velocity graph. Mechanisms like oxidational and delamination wear occur at low speed with low and high load, respectively. At higher speed and lower load, mild and severe oxidational wear prevailed. Melt wear prevails at higher loads and speeds at which surface melting is observed. Seizure indicates failure at sufficiently high loads at which the effect of sliding speed is negligible on the operating wear mechanism.

Ashby et al. [53] suggested that increase in surface temperature during dry sliding would affect the friction and wear rate. Temperature maps were constructed for different materials using the tests results carried out using pin-on-disk configuration, one of which is shown in figure 2.14 with pin and disc both made of low carbon steel. The map was made out of the results from experiments done by different researchers under similar sliding conditions. The flash temperature is the temperature due to the heat at true contact area A_n, and is much higher than the bulk temperature. It can be expressed as:

$$T_f - T_{b'} = \frac{\mu FV}{A_r} \left(\frac{K_1}{l_{1f}} + \frac{K_2}{l_{2f}}\right)^{-1} \tag{2.11}$$

where T_o is the temperature of the remote sink, k_1 and k_2 are the thermal conductivities of the two materials, and l_{1f} and l_{2f} depend on the size of the asperities and factors on which l_{1b} and l_{2b} also depend. The sink temperature for individual asperities is usually T_b, however, when the seizure load F_s is approached, A_r gradually becomes equal to A_n, causing the distinction between bulk temperature and flash temperature to disappear. The bulk temperature, T_b, is the temperature that would appear at the surfaces due to frictional heat injected uniformly across the nominal area, hence, can be considered as an average surface temperature. For all geometries, it is given by:

$$T_b - T_o = \frac{\mu FV}{n} \left(\frac{K_1}{l_{1b}} + \frac{K_2}{l_{2b}}\right)^{-1} \tag{2.12}$$

where T_o is the temperature of the remote sink, k_1 and k_2 are the thermal conductivities of the two materials, and l_{1b} and l_{2b} are the equivalent linear heat-diffusion distance from the sliding surfaces to the heat sinks for surfaces 1 and 2. In almost all dry sliding tests, conduction is the most dominant mode of heat transfer. However, the equivalent lengths depend on various factors like geometry of heat flow (linear, radial, etc), mode of heat flow (transient or steady-state), thermal contact resistance between pin and its clamp.

Therefore, l_{1b} and l_{2b} cannot be equated to obvious physical lengths. At low sliding velocities, μ depends upon surface condition of the sliding surfaces, while at higher sliding velocities, it becomes velocity dependent, decreasing with increase in velocity. The flash and bulk temperature contours constructed showing the relation between the two temperatures. At lower velocities, none of the flash or bulk temperatures were significantly high, hence, this regime was termed as cold regime showing no significant rise in temperatures of the sliding surfaces. At higher velocities and lower loads, a rise in flash temperature is shown with no significant rise in bulk temperature. This was attributed to the asperity heating as a result of high velocity which was conducted away through the specimen holder, thereby, showing no rise in bulk temperature. Finally, at high loads and velocities, rise in both flash and bulk temperatures was noted which resulted in large scale melting of the surfaces.

Welsh [54] reported structural changes and intense hardening of the surface produced as a result of high frictional heating induced during dry sliding of steel. It was shown that the hardening of the sliding surfaces was a result of martensitic transformation induced by rapid thermal fluctuations on the sliding surface. The carbon content of the steel used for the experiment facilitated the hardening process. However, under imperfectly lubricated sliding condition, carbon or nitrogen from the atmosphere or the lubricant could also enter the surface and contribute in the hardening process. Wearing down of the hardened surface layer, covering almost the whole contacting surface, was found to be inevitable. However, the wearing down of the hardened surface layer occurred in patches. The process of formation of the hardened layer was found to be reversible as the hardened surface was regenerated following the wearing down of the previous layer.

The transition between mild to severe is delayed due to the introduction of Al_2O_3 particles in 6061 Al alloy as compared to the unreinforced 6061 Al alloy [55]. Figure 2.15 illustrates the progression of wear for unreinforced 6061 Al alloy and its composite (with 20% Al_2O_3 particles) tested against AISI 52100 steel counterface under dry sliding condition using a block-on-ring configuration. The mild wear (region II) and severe wear (region III) are evident in both the reinforced alloy and the composite with a significant delayed transition to severe wear as compared to the unreinforced alloy. Further, region I can only be observed for the composites due to the load bearing capacity of Al_2O_3 particles which remain unworn. Region II is initiated when the applied load exceeds the load bearing capacity of the fibres and oxide reinforcement does not provide beneficial effect in improving the wear because of the low fracture toughness of the composite. Subsurface delamination and abrasion are the dominant damage mechanisms in region II. Region III is marked by an abrupt increase in the wear rates induced by increase in frictional temperature. In another study [56], the effects of particle size, volume fraction, counterface and even the type of reinforcement on the wear rates of the composites were studied using 2014Al- 20% SiC, 6061 Al-10% Al_2O_3 and 6061 Al-20% Al_2O_3 composites and counterfaces made of AISI 52100 and mullite. It was observed that the wear resistance of the composites increased with the increase in particle size and volume fraction of the reinforcement. It was further observed that the use of a counterface with higher thermal conductivity delayed the transition to severe wear it contributes in conducting the frictional heat away from the composite sample, thereby, lowering the temperature of the sample below the critical temperature as shown in figure 2.16. Hence,

it was established that the transition from mild to severe wear occurred due to the rise in the bulk temperature above a critical temperature value of 397 K.

Zhang and Alpas [43] investigated mild and severe wear transitions for Al-Mg-Si alloy (6061 Al) by conducting dry sliding tests against SAE 52100 bearing steel rings at the load range of 1-450 N and sliding velocity of 0.1-5.0 m/s. Mild to severe wear transition was found to depend on surface temperature induced by sliding. A linear increase in the volumetric wear occurred in mild wear in which wear rates always attain equilibrium while an abrupt change in slope was termed as severe wear as shown in figure 2.17. For a constant velocity, the distance at which transition occurred increased with a decrease in applied load as shown in figure 2.18. It was observed that mild wear prevailed at lower bulk surface temperatures (T_b) while the transition to severe wear was observed when the bulk surface temperatures exceeded the critical temperature (T_c) of 395 K for this system (Figure 2.19). SEM revealed the presence of two types of wear debris in mild wear, suggesting two different types of wear mechanisms represented in the form of a wear map shown in figure 2.20: i) The first wear mechanism is spalling of mechanically mixed layers, where aluminum oxide forms at contact points due to oxidation of Al, acting as an abrasive. Fe particles transferred from the counterface led to the formation of dark discontinuous compacted layers of mechanically mixed wear particles on the contact surfaces. Formation of such layer allows mild wear to continue at a steady state. The wear debris is comprised of this mechanically mixed layer. ii) The second wear mechanism is delamination wear. The wear debris at higher loads and velocity, having plate-like morphology, consists of Al (observed by Electron Dispersive X-Ray Spectroscopy (EDS)) detached from the bulk 6061 Al. The mechanism identified was

delamination wear, where a subsurface crack develops and propagates until a wear fragment becomes detached. The bulk temperature for both mechanisms in the mild wear regime was found to be lower than the critical transition temperature. SEM micrograph of the worn surface (Fig. 2.23(a)) and wear debris (Fig. 2.23(b)) for severe wear regime show that the worn surface had a metallic and shiny appearance while the debris particles had a plate-like morphology but were considerably thicker (i.e. *50-2001lm* thick) and longer (i.e. typically 0.5-2 mm) than the plate-like particles produced in the mild wear. The map also shows an intermediate wear regime, termed as transient wear regime, where mild wear is initially observed but it transforms into severe wear after a certain sliding distance. The worn surfaces and wear debris indicating the two wear regimes are shown in figure 2.21 and 2.22. To obtain a better understanding of the effect of temperature on the transition from mild to severe, forced cooling experiment was performed at a severe wear sliding condition which showed that the wear rate and mechanisms were restricted to that of the mild wear at a sliding condition that would otherwise yield severe wear phenomena.

A detailed study to describe the subregimes within the mild wear regime was carried out by Elmadagli and Alpas [58], who conducted dry block-on-ring tests with as-cast 383 (with 9.5 wt.% Si), A390 (with 18.5 wt.% Si), and Al-25Si (with 25 wt.% Si) against SAE 52100 steel. The mild wear regime showed two subregimes: the first mild wear subregime (MW-1) and the second mild wear subregime (MW-2) (Fig.2.5). The steady state of mild wear regime and the relationship of wear rate (W) to load (L) are represented by the relation:

$$W = CL^n \qquad\qquad (2.13)$$

where C=wear coefficients comprising of C1 for MW-1 and C2 for MW-2 which were sensitive to microstructure, while n=wear exponent was independent of it. The following information was obtained: i) an increase in Si wt% from 9.5 to 25 wt.% increased transition load by 140%, but had only a minor effect on C; ii) an increase in alloy hardness from 31.6 to 53.5 HRB greatly increased transition load by 400%, but had only a minor effect on C; iii) a 47% decrease in the Si particle aspect ratio reduced wear coefficients C1 by 27% and C2 by 31%, with minor increase in transition load; iv) a 93% decrease in Si particle size reduced C1 by 35% and C2 by 58%, while L1 and L2 were increased by 71% and 33% respectively, where C is the wear coefficient. These subregimes were also observed in another study [59] as a function of applied loads for wear tests conducted on A390 blocks against 52100 steel rings in dry air (RH 5%). It was observed that the wear rate in MW-2 is greater than that in MW-1. Although tribolayer formation, generated by mixing and transfer of material from the counterface to the Al-Si contact surface, was detected in both the subregimes, the transition from MW-1 to MW-2 coincided with an increase in the amount of material transferred to the counterface. The high wear rate observed in MW-2 suggests that the aluminum matrix came in contact with the counterface through the fractured portions of the tribolayer in MW-2. The presence of Al layers on the tribolayer was observed in the MW-2. Both spallation of the thick tribolayers formed in MW-2, which caused transfer and back-transfer of the aluminum from the counterface (Fig.2.6), along with the extrusion of the exposed aluminum surface over the tribolayers caused the increased wear rate in MW-2 as compared to MW-1. Wilson and Alpas [60] investigated the role of temperature in

transition from predominant oxidation mechanism to delamination wear within the mild wear regime for A356 Al alloy. Besides the fact that a bulk temperature greater than the critical bulk temperature (T_c) results in a transition from mild to severe wear, it was found that asperity flash temperature exceeding the critical bulk temperature resulted in a transition from the predominant oxidation wear mechanism to delamination wear within the mild wear regime.

Similar studies of dry sliding wear were conducted on Mg-Al alloys. Chen and Alpas [60,61] conducted unlubricated block-on-ring tests on a Mg-9Al-0.9Zn (AZ91) alloy its composite AZ91-10%SiC_P and presented a wear map where the volumetric wear rates were plotted as a function of load and sliding velocity as shown in figure 2.24. The authors classified sliding wear of AZ91 alloy into two main wear regimes, mild wear and severe wear. In the mild wear regime, wear progressed under steady-state wear rate conditions with the two predominant wear mechanisms: i) oxidational wear, which is characterized by MgO debris formation, and ii) delamination wear, characterized by material transfer from the alloy to the steel counterface. In the severe wear regime, wear rates increased continuously with the sliding distance. The severe wear regime was also subdivided into two wear regimes: plastic deformation-induced wear and melt wear. The wear mechanisms were summarized in a wear mechanism map, which helped predict the load and sliding velocity marking the wear transitions.

Another prominent work regarding the wear mapping approach was the construction of wear map for grey cast iron as shown in figure 2.25 [62]. It was found that wear rates for mild wear were primarily controlled by surface oxidation. The transition from mild to severe wear was accompanied by an increase in the surface roughness and surface

temperatures of the sliding surfaces. The sharp increase in temperature due to frictional heating resulted in the softening of the surface which initiated the local welding of the large-sized cast iron debris, which were transferred to the counterface. Besides the mild and severe wear regime, another wear regime, with significantly lower wear rates either at low loads and/or low speeds, was identified for grey cast iron termed as ultra mild wear regime. The wear rates for ultra-mild wear regime were found to be of two orders of magnitude less than those in the mild wear regime. The worn surfaces were covered by continuous layers of compacted reddish iron oxide powder while continuous reddish strips were found on the surface of the steel counterface. The presence of oxide layer prevented the metal-to-metal contact between the cast iron samples and the steel rings except during the initial stages of wear.
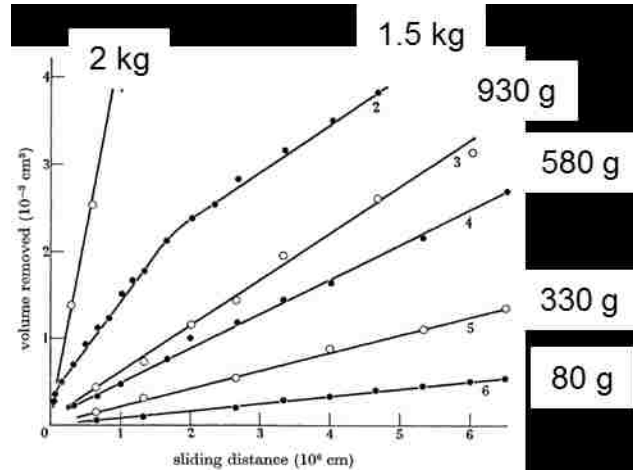
Figure 2.11.Volume removed against sliding distance plots for ferritic stainless steel pins on hardened tool steel rings at various loads [50].
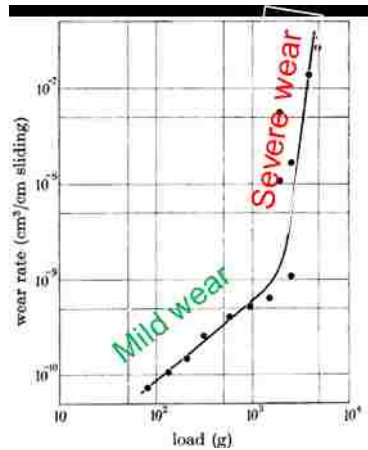
Figure 2.12.Wear rate against load for ferritic steel pins on high-speed tool steel rings at 1.8 m/s [50].
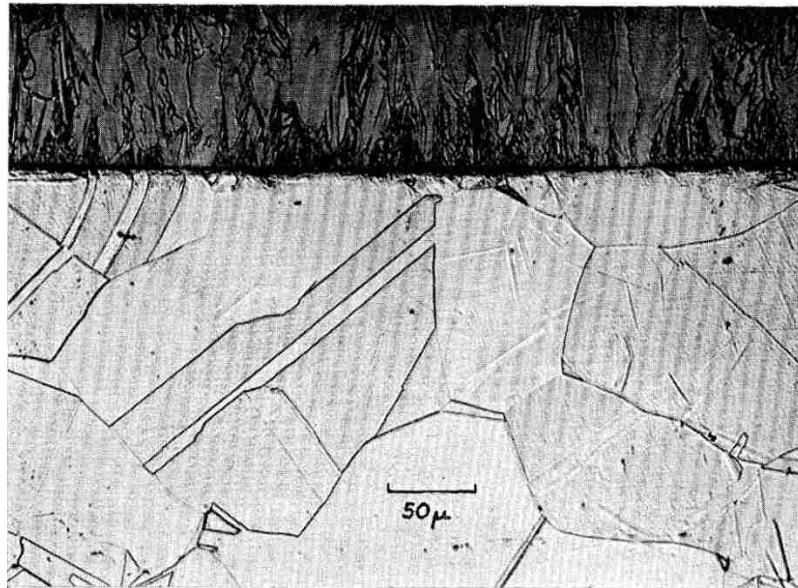
(a)

(b)

Figure 2.13.Metallographic sections of 70/30 brass pins (a) Mild wear after rubbing on hardened tool steel ring at 50 g and 0.195 m/s (b) Severe wear after rubbing on 70/30 brass ring at 240 g and 1.95 m/s [50].

Table 2-3 Wear rates of pins of different materials at a load of 400 g [50].
(Speed 180 cm/s. Rings are hardened tool steel except where stated otherwise)

combination of materials	wear rate $(10^{-10}\,\mathrm{cm^3/cm})$	hardness $(10^6\,\mathrm{g/cm^2})$	calc. value of K (from (1))
mild steel on mild steel	1570	18·6	7×10^{-3}
60/40 brass	240	9·5	6×10^{-4}
Teflon	200	0·5	$2·5 \times 10^{-5}$
70/30 brass	100	6·8	$1·7 \times 10^{-4}$
Perspex	14·5	2·0	7×10^{-6}
moulded Bakelite $\times$ 5073*	12·0	2·5	$7·5 \times 10^{-6}$
silver steel	7·5	32	6×10^{-5}
beryllium copper	7·1	21	$3·7 \times 10^{-5}$
hardened tool steel	6·0	85	$1·3 \times 10^{-4}$
Stellite grade 1	3·2	69	$5·5 \times 10^{-5}$
ferritic stainless steel	2·7	25	$1·7 \times 10^{-5}$
laminated Bakelite 292/16*	1·8	3·3	$1·5 \times 10^{-6}$
moulded Bakelite 11085/1*	1·0	3·0	$7·5 \times 10^{-7}$
sintered tungsten carbide on mild steel	0·9	18·6	4×10^{-6}
laminated Bakelite 547/1*	0·4	2·9	3×10^{-7}
polyethylene	0·3	0·17	$1·3 \times 10^{-7}$
sintered tungsten carbide on sintered tungsten carbide	0·03	130	1×10^{-6}
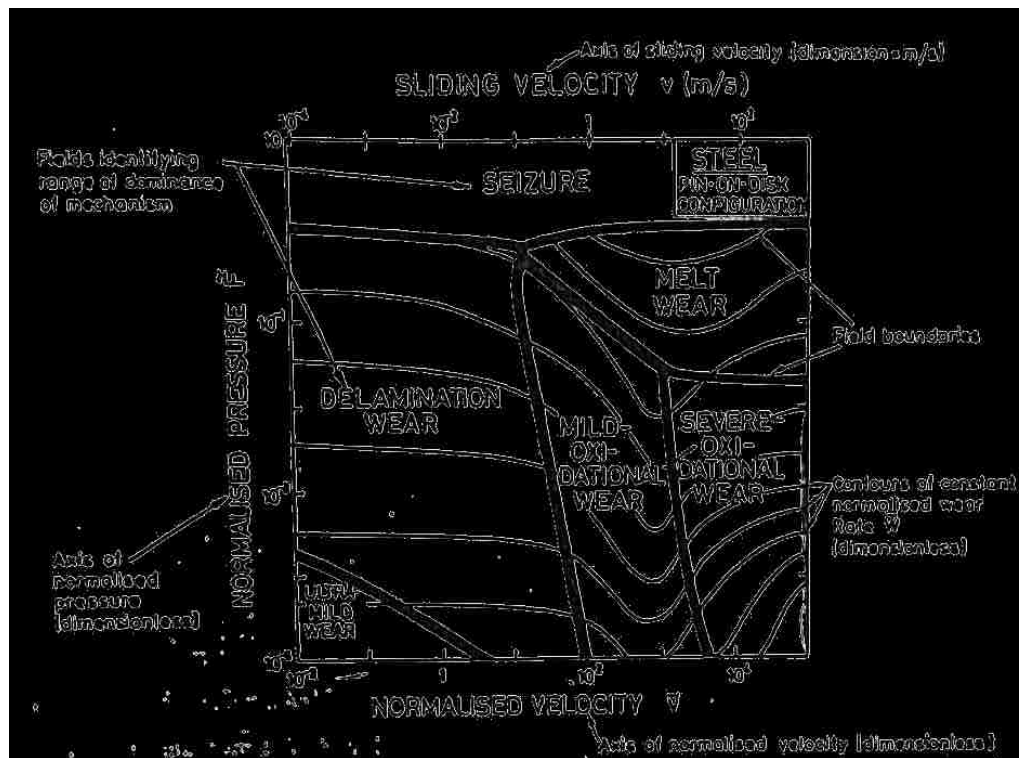
Figure 2.14. Empirical wear mechanism map for steel using the pin-on-disk configuration [52].
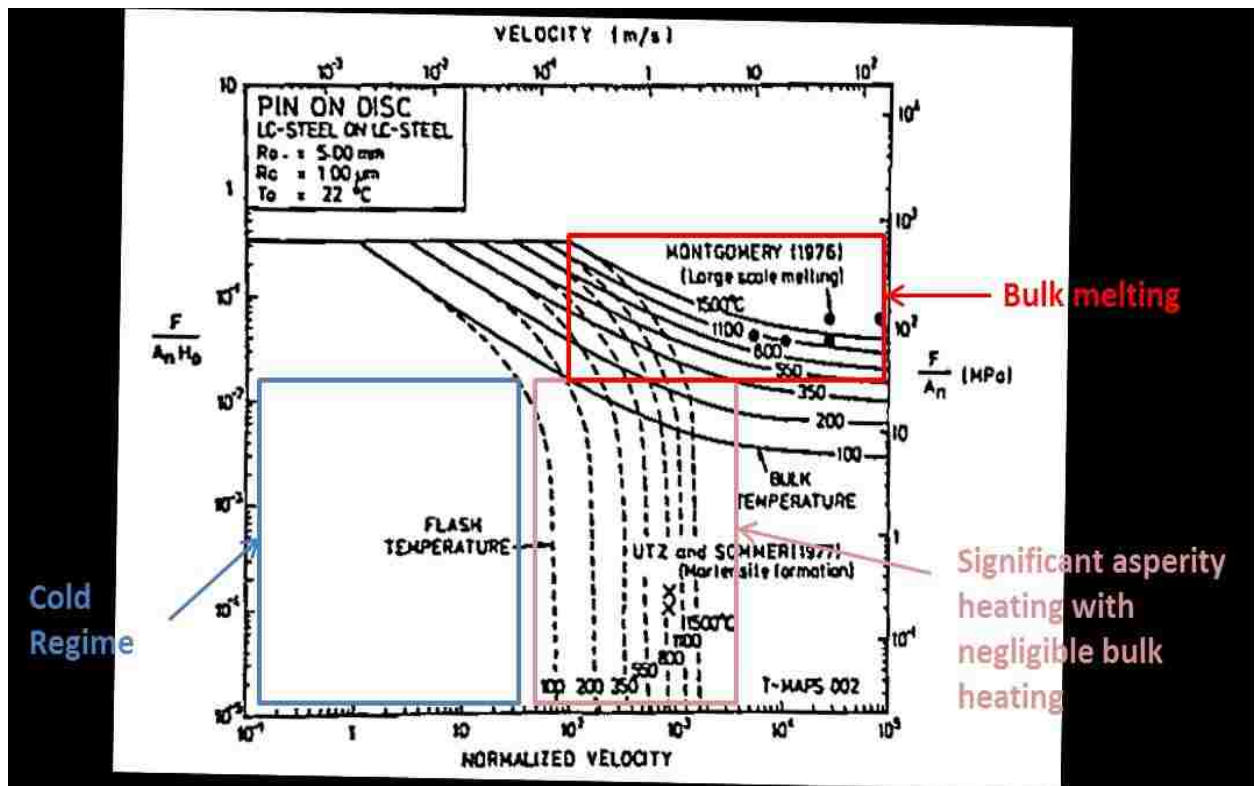
Figure 2.15.Temperature map for low carbon steel sliding on itself in a pin-on-disk configuration [53].
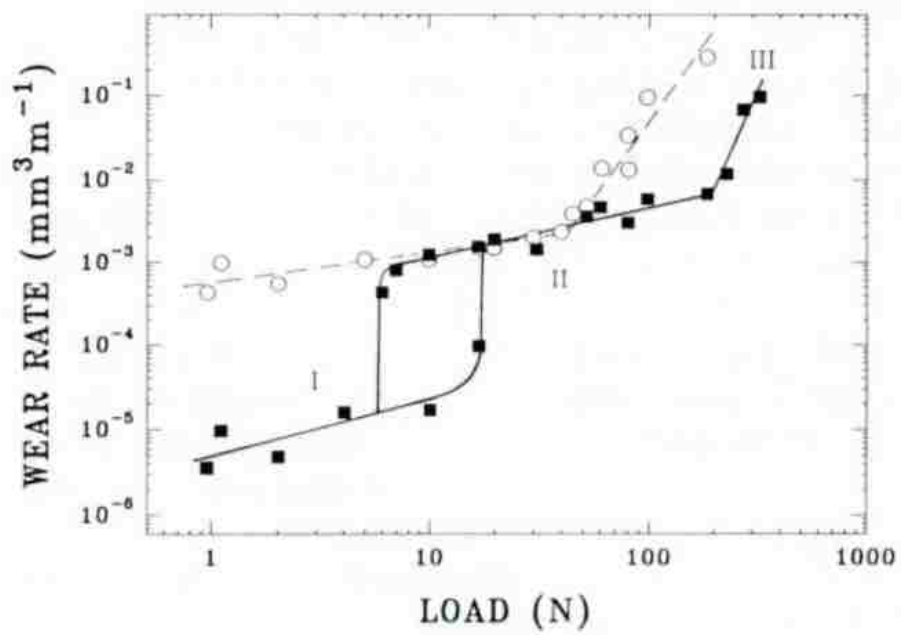
Figure 2.16. Wear rate vs. applied load diagram for (■) 6061-20% Al_2O_3; (○) 6061 Al [55].
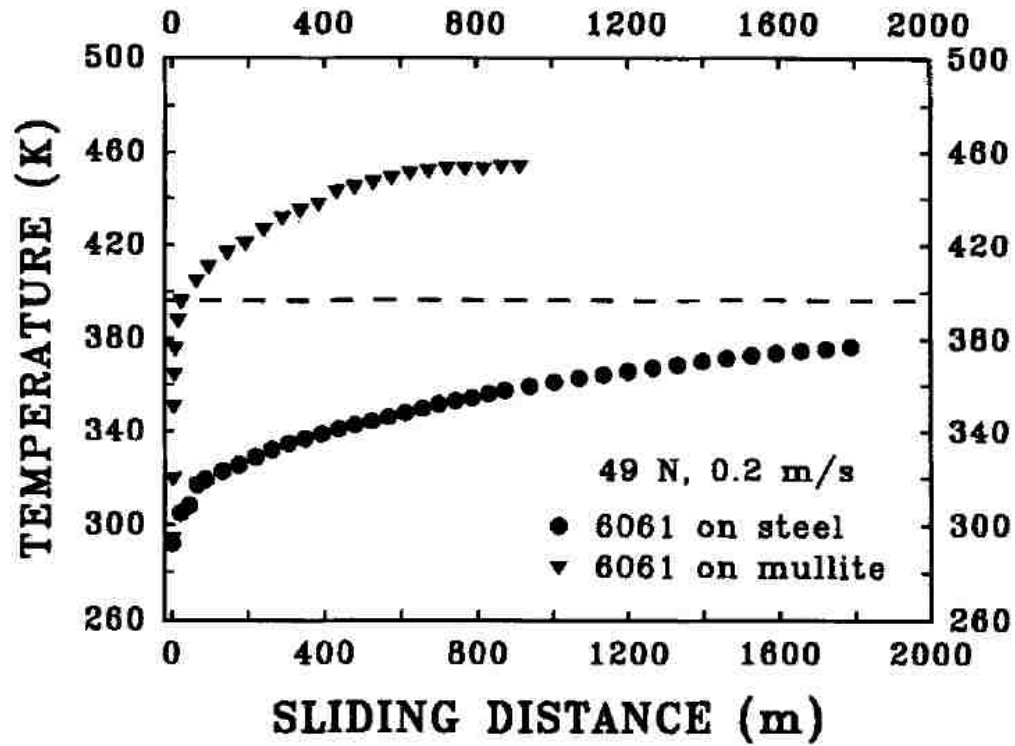
Figure 2.17. Temperature vs sliding distance diagram for 6061A1 (T) against a mullite slider and (O) against SAE52100 slider at an applied load of 49 N. The transition temperature (to severe wear) is indicated by the dashed line. [56]
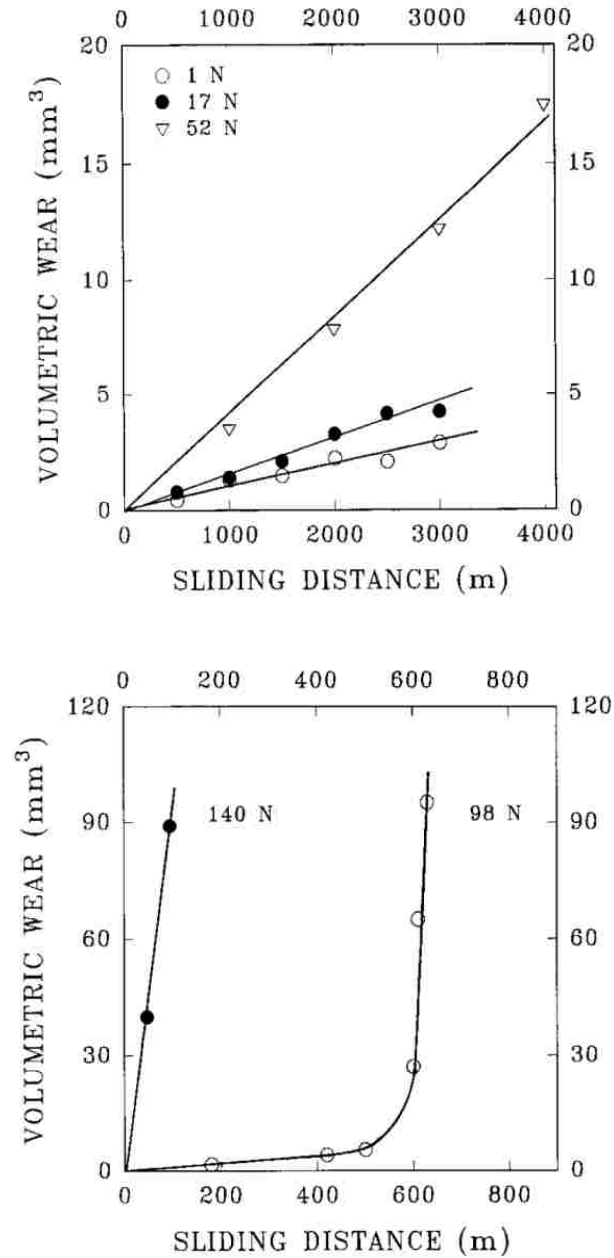
Figure 2.18. Typical volume loss versus sliding distance curves illustrating (a) steady-state nature of wear at loads 1 N, 17 N, 52 N in the mild wear regime; (b) transient nature of wear at 98 N where mild to severe wear transition occurs at 500 m and at 140 N when severe wear initiates almost immediately [57].
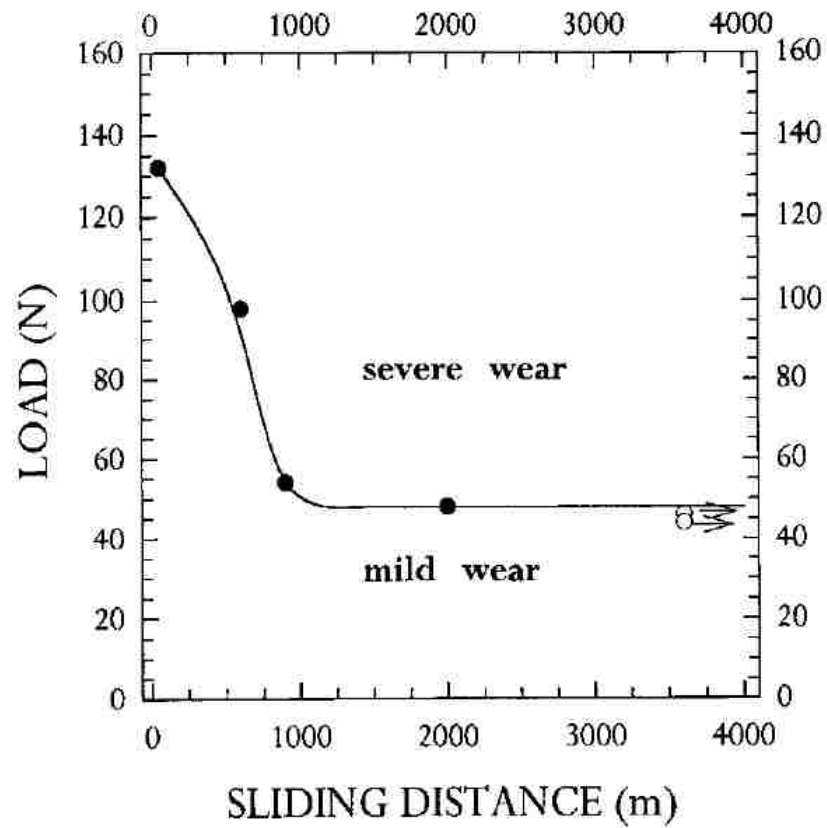
Figure 2.19.Effect of load on the sliding distance at which the mild to severe wear transition initiates. Only mild wear occurred under the conditions indicated by the open circles (0). $v = 0.8$ m s^{-1} [57].
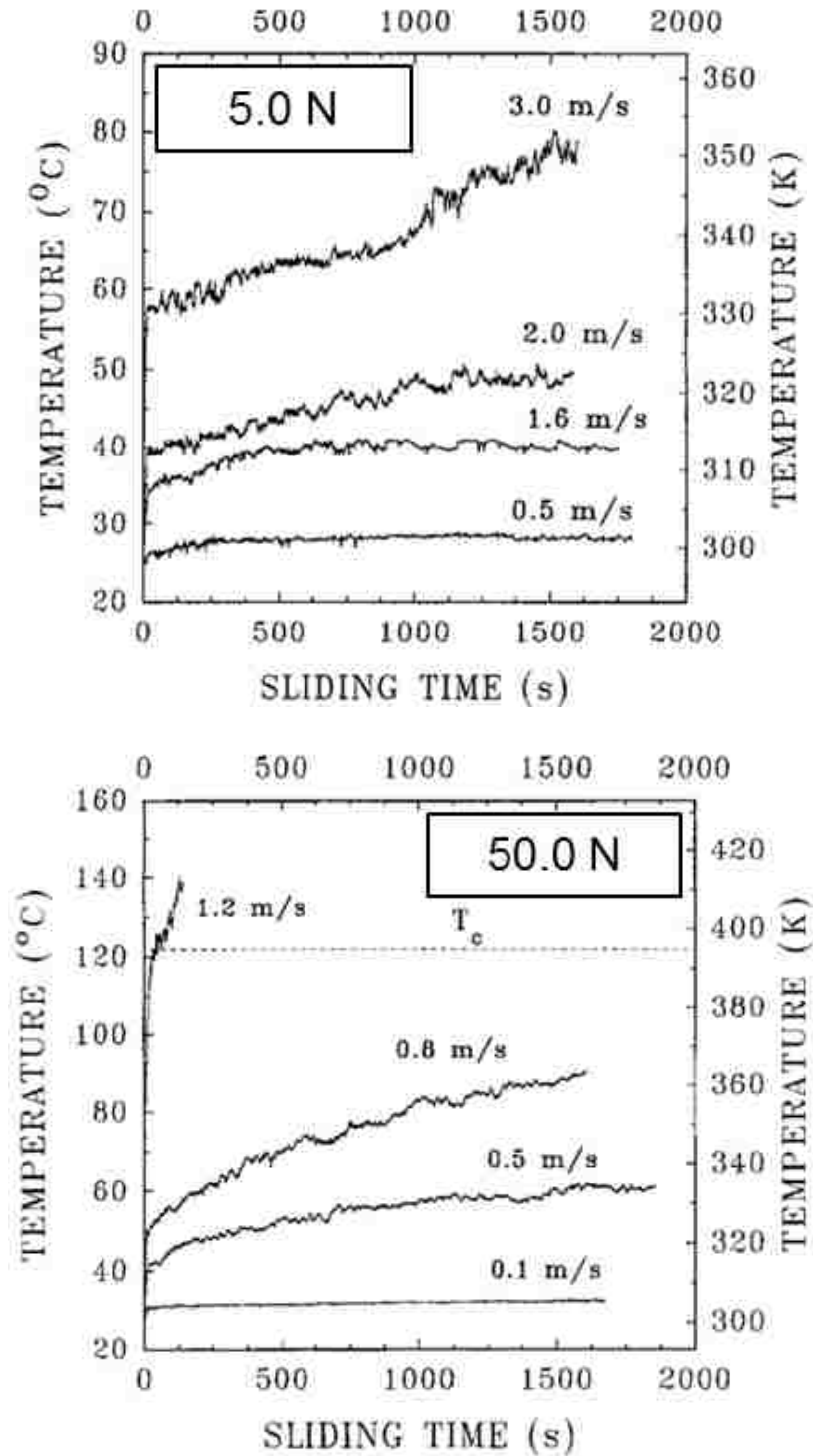
Figure 2.20. (a) Contact surface temperature versus sliding time plots at different sliding velocities at a constant load of 5.0 N; (b) Contact surface temperature versus sliding time plots at 50 N [57].
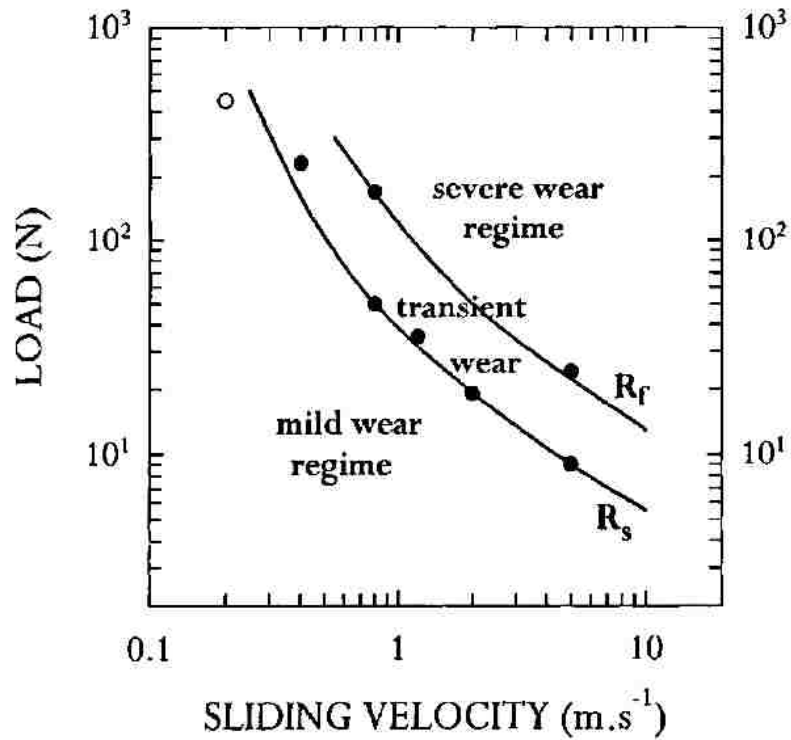
Figure 2.21.Wear transition map for 6061 Al against SAE 52100 steel counterface.R_s indicates load and sliding velocity combinations at which mild to severe wear transition is first observed. Below the solid line, R_s mild wear conditions prevail. Only severe wear occurs above R_f. Wear is transient in the region between R_s and R_f, i.e. mild wear transforms into severe wear after a certain sliding distance (open symbol (0) indicates that no transition is observed under that combination of applied load and velocity) [57]
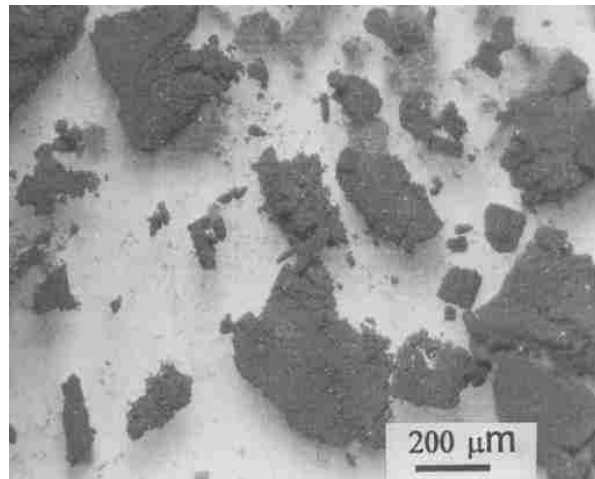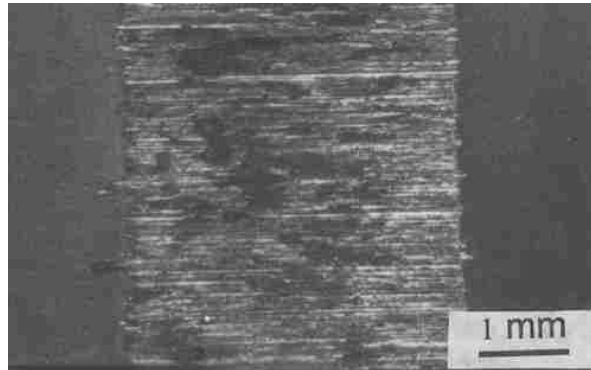
Figure 2.22.(a) Optical micrograph showing typical morphology of the worn surface in the mild wear regime; (b) Optical micrograph of the debris that agglomerate to form the dark colored aggregates, load = 10 N, v = 0.8 m/s [57].
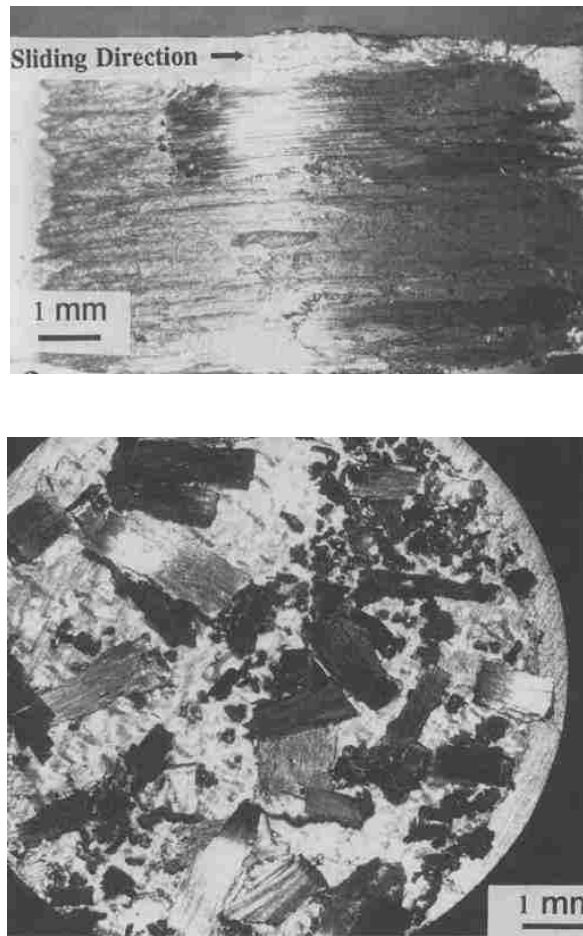
Figure 2.23. Optical micrograph showing (a) Typical morphology of the worn surfaces in the severe wear regime; (b) Wear debris, load = 98 N, v = 0.8m/s. [57].
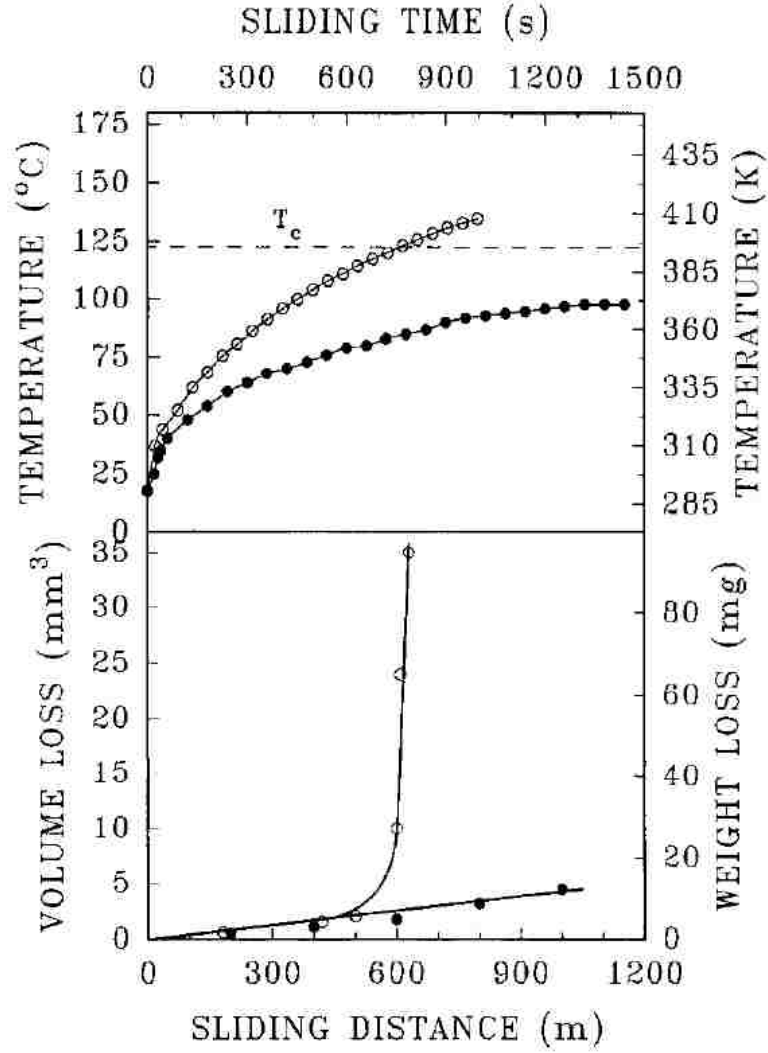
Figure 2.24.Effect of forced cooling by chilled water on the mild to severe wear transition in 6061 Al worn against SAE 52100 steel: (a) Temperature distribution at the contact surface as a function of sliding distance; (b) Corresponding volume loss versus sliding distance diagram. Without cooling the system the contact surface temperature exceeds T_c (395 K) leading to the severe wear ($\circ$). Cooling the system will ensure that the contact surface temperature stays below 395 K, thus only mild wear is observed ($\bullet$). Load = 98 N, v = 0.8 m/s [57].
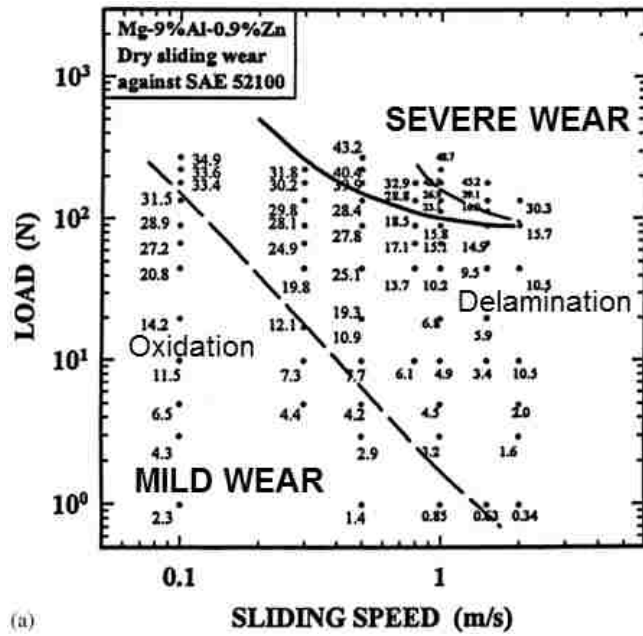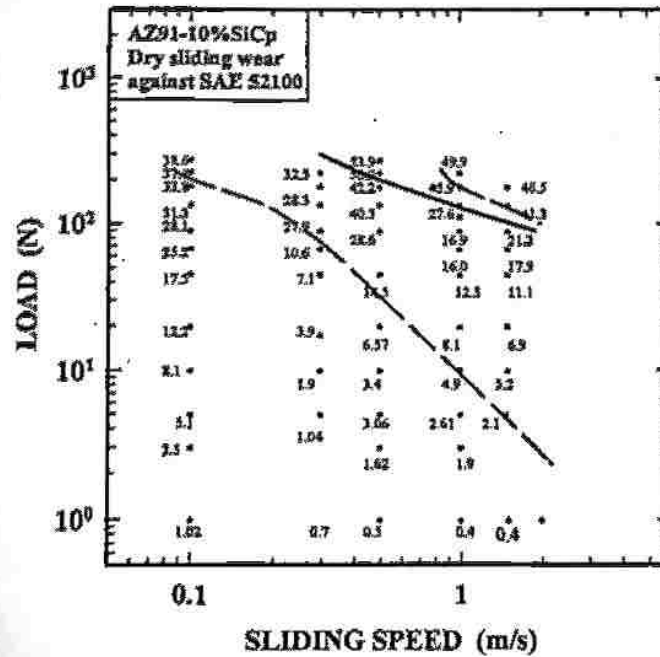
Figure 2.25. Wear rate map for (a) AZ91; (b) AZ91-10%SiC$_p$ in dry sliding wear. Each point on the map represents a wear rate measurement made at a given set of load and sliding speed. To find the actual wear rates in mm3/m multiply each number by 10^{-3}. The continuous line represents the boundary between the mild and severe wear. The transitions between the sub-regimes are marked by dashed lines [60,61].
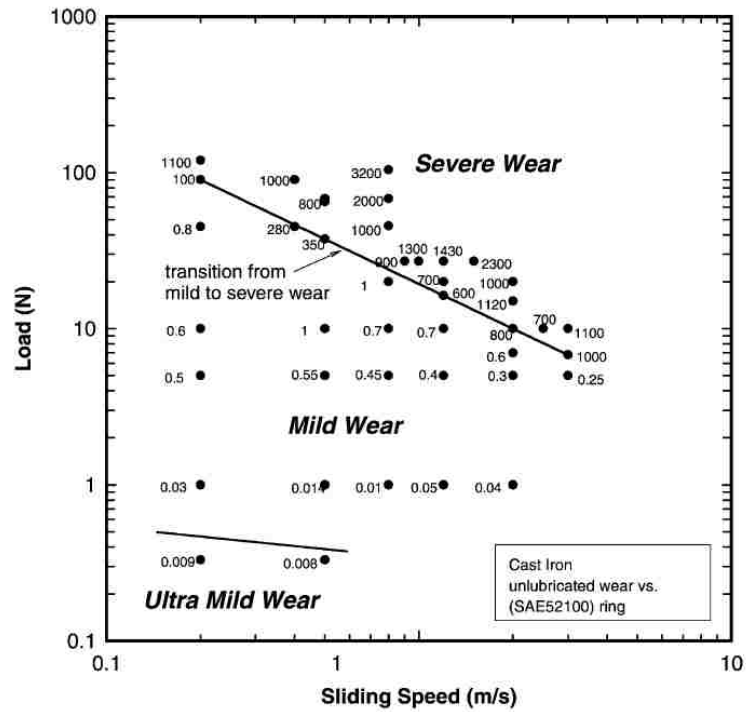
Figure 2.26. The wear map constructed for the grey cast iron. Three major wear regimes of ultra-mild, mild, and severe wear are depicted on the map. The wear rates shown should be multiplied by 10^{-3} to find the actual wear rates in mm^3/m [62].

2.5.2. Wear of Mg based alloys and composites

Desire to improve the strength of light weight magnesium with the required mechanical properties led to the development of Mg alloy metal matrix composites (MMCs) for automotive and other advanced engineering applications [63,64]. Chen and Alpas [60,61] identified oxidation and delamination as the two dominant wear mechanisms in the mild wear regime under dry sliding condition for Mg alloy AZ91 and AZ91-10%SiC_P. A tribolayer was formed on the sliding surface of magnesium alloy AM60 at low speeds which was found to be rich in magnesium oxide. Under severe wear regime, a subsurface deformation was found to occur beneath the sliding surface at higher loads and speeds. Two wear mechanisms, (i) plastic deformation induced wear and (ii) melt wear were found to be dominant in the severe wear regime. No oxygen content was found on the surface, while the deformed layer below the sliding surface was found to be about 100 µm thick. As the load was increased further, the thickness of the deformed layer was increased to 200 µm and the formation of metallic debris explained the beginning of severe wear. As the loads were further increased in the severe wear regime, melt wear was found to be a dominant wear mechanism. Localized melting forms thin liquid film on the sliding surface, thereby, providing melt lubrication. The molten surface builds up chunks at the edge of the specimen block (Figure 2.26) which, later, broke away as metallic wear debris (Figure 2.27). It was concluded that the transition from mild to severe wear occurred when the bulk temperature exceeded a critical temperature of 347 ± 15 K. It was further stated that the temperature change with the sliding distance for a tribo-system was a function of applied load, sliding velocity and sliding distance (Eq. 2.14).

$$T = f(F,V,D) \qquad (2.14)$$

A regression analysis on the surface temperatures measured during the sliding tests was performed which showed that the highest temperature T_{max} obtained at any given condition of the applied load (F) and sliding speed (V) can be expressed as shown in Eqn. 2.15.

$$T_{max} = T_0 + aF^{1/4}V^{1/2} \qquad (2.15)$$

Where, T_0 is the initial environment temperature at the beginning of the test and a is the regression coefficient. It was also concluded that mild to severe wear transition that occurs at a certain combination of load, velocity and sliding distance was controlled by a surface temperature criterion which coincided with the threshold temperature at which thermally activated processes, such as dynamic recrystallisation initiated.

The subsurface damage and recrystallization of deformed grains below the sliding surface at high temperatures was studied by Das et al. [65]. Dry sliding tests were performed using pin-on-disk configuration using magnesium alloy AZ31disks and AISI 52100 tool steel balls as the counterface at temperatures between 298 K and 673 K, constant load and speed of 5.0 N and 0.01 m/s respectively. At the given sliding condition, oxidational wear was observed at temperatures between 298 K and 575 K while plastic deformation controlled wear was observed as a dominant wear mechanism above 600 K. Using a reference marker inserted, i.e. a thin plate of AZ31 inserted in AZ31 sample normal to its contact surface (Figure 2.28), a plastic strain, ε, was observed below the sliding surface of AZ31 which was calculated using the angle, θ, between the tangent line to the marker

and the axis perpendicular to the sliding surface , i.e., the original position of the marker using the following equation:

$$\varepsilon = \frac{1}{\sqrt{3}}(\tan \theta) \tag{2.16}$$

It was also shown that at high temperatures, the sliding surface undergoes dynamic recrystallization producing fine grains on the sliding surface along with the coarse grains that were formed below the dynamically recrystallized grains as shown in figure 2.29. The mechanism of the sliding induced microstructural changes including formation of dynamically recrystallized surface grains, grain growth underneath the recrystallized grains and the grain boundary sliding is explained via figure 2.30. The deformation and damage mechanism events were cyclically repeated in the course of high temperature sliding to attain an equilibrium microstructure and a steady-state wear rate.

Sharma et al. [66] studied the effect of reinforcing AZ91 alloy with feldspar particles, of size 30-50 μm in proportion of 1, 3 and 5%, on the tribological properties of the resulting composite. For this purpose a pin-on-disk tribometer was used and dry sliding wear tests were conducted using the composite pins against an EN24 steel counterface at loads between 20-100 N and sliding speeds of 0.62, 0.94 and 1.25 m/s. Results showed that reinforcing AZ91 with feldspar improved the wear resistance of the composite in comparison with the unreinforced alloy. Fine scratches that were formed due to the action of the wear hardened deposits on the wear track, provided evidence for the domination of abrasion wear mechanism at low loads. At high loads, delamination wear was suggested by the presence of distinct grooves and damaged spots in the form of craters. It was found that increase in the feldspar content increased the dry sliding wear resistance of the

composite. However, it was further elaborated that the increase in the feldspar content only increased the abrasive wear resistance but decreased the delamination wear resistance which was induced by massive surface damage and material transfer to the counterface, thereby delaying the transition from mild to severe wear. A critical load was also determined for each sliding speed and feldspar content, above which, the wear rate was found to increase abruptly. It was established that an optimum value of reinforcement particles existed above which the wear rates higher than those of the reinforced alloys were observed despite an increase in the hardness [66,67]. The delamination wear mechanism was also found to be intensified due to high reinforcement content which gave rise to the subsurface cracks that initiated from the decohesion at the particle-matrix interface and propagation of the so formed cracks [55,68,69].

Lim et al. [70] investigated the effect of reinforcing Mg with nano-sized reinforcement in lesser volume fraction.Dry sliding wear tests were conducted using pin–on-disc tribometer with pins made of 99.99% pure Mg reinforced with 0.22, 0.66 and 1.11 % of alumina particles with a nominal size of 50 nm against AISI-O1 tool steel disc. The 1.11% alumina reinforced composite showed improvement in wear resistance at more severe sliding conditions as shown in figure 2.31. Abrasion, adhesion and thermal softening were the main mechanisms observed at different sliding speeds. The small amount and size of the reinforcement prevented occurrence of delamination wear.

Banerji et al. [71] studied the boundary lubricated sliding behaviour of AM60 alloy reinforced with 9, 11 and 26 % alumina fibres by carrying out boundary lubricated sliding tests using pin-on-disc configuration using composite pins against AISI 52100 disc as the counterface within a load range of 1.0-5.0 N. The test parameters simulated

the sliding conditions observed in automotive engines blocks showing ultra-mild wear regime. AM60-9% $(Al_2O_3)_f$ and AM60-11% $(Al_2O_3)_f$ showed similar wear damage in the form of fractured particles and grooves on the Mg matrix at high sliding cycles. Wear resistance of the composites increased with an increase in the volume percentage of the alumina fibres. Wear processes and mechanism were identified by studying worn samples of AM60- 9% $(Al_2O_3)_f$. After the wear tests, the fibres were fractured and sank into the Mg matrix at all loads, the extent of sinking of the particles, however, increased with an increase in the load as shown in figure 2.32. The composites showed negligible wear in comparison with the unreinforced alloy as shown in figure 2.33.Due to lack of hardness in comparison with the hardness of the reinforcement phase, the counterface was also observed to be worn off. Increasing the test temperature to 100 °C showed a further improvement in the wear resistance of the composite by a reduction in the sinking of the alumina fibres as shown in figure 2.34. The improvement in wear resistance at high temperature was attributed to the formation of an oil-residue layer (ORL) which was favored at high temperature, while no ORL was observed to form at 25 °C. The formation of ORL was also observed on the counterface, thereby reducing the wear of the counterface as well. The ORL formed mainly on the top of the fibres and on the worn Mg matrix as well, was found to comprise of Zn, P, S and C which originated from the breakdown of zincdialkyldithiophosphate(ZDDP) additive, the most effective class of antiwear, antioxidant and anticorrosive additive used in the engine oil, at high temperature and formed stabilized tribolayer due to the underlying nanosized Mg grains formed due to severe plastic deformation of the subsurface during sliding wear.
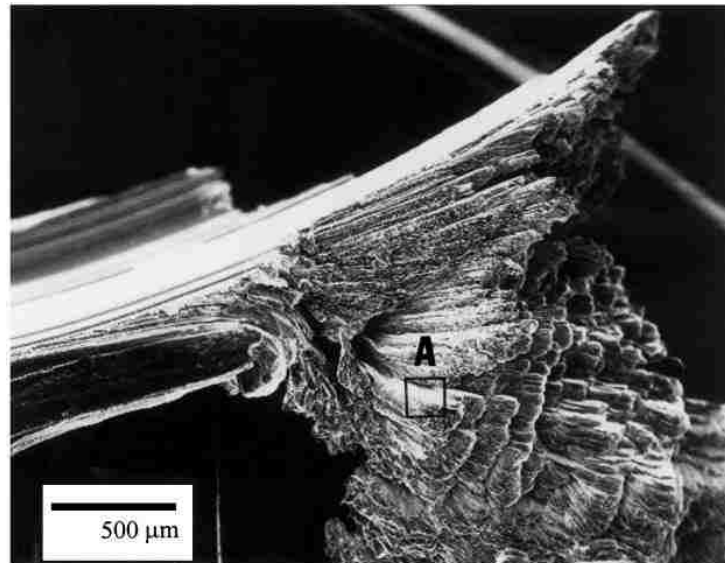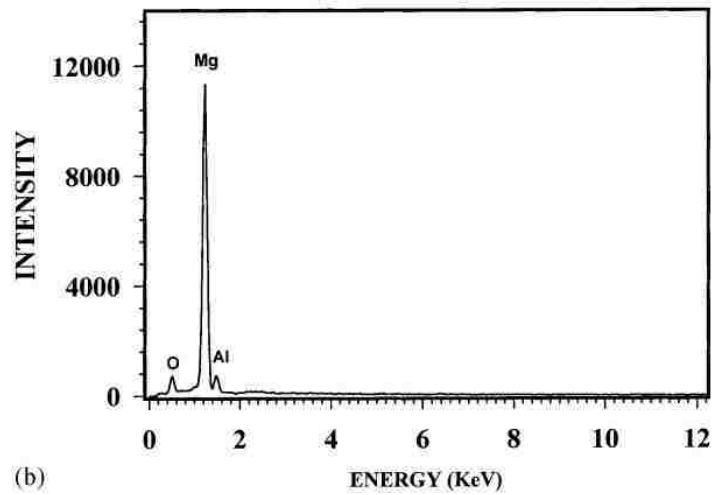
Figure 2.27. (a) SEM micrograph of wear debris produced as a result of friction induced surface melting (v = 1.0 m/s and load = 224 N); (b) EDS spectrum of wear debris corresponding to area A in Figure 2.26 (a) [60]
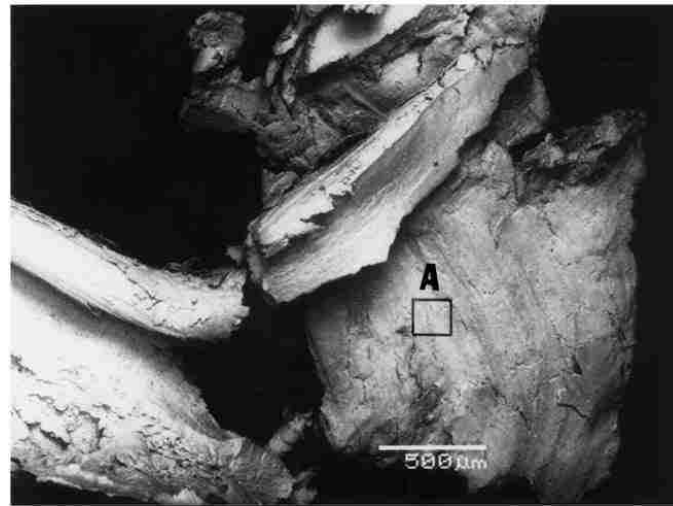
(a)
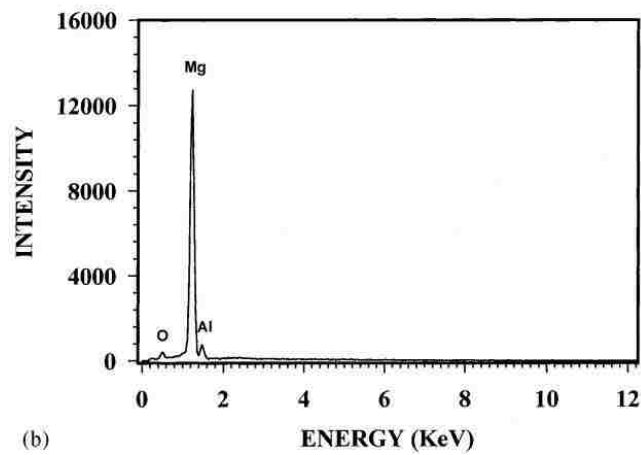
(b)

Figure 2.28. (a) SEM micrograph of wear debris produced as a result of extrusion of severely deformed surface layers (v = 1.0 m/s and load = 133 N); (b) EDS spectrum of wear debris corresponding to area A in Figure 2.27 (a). [60]
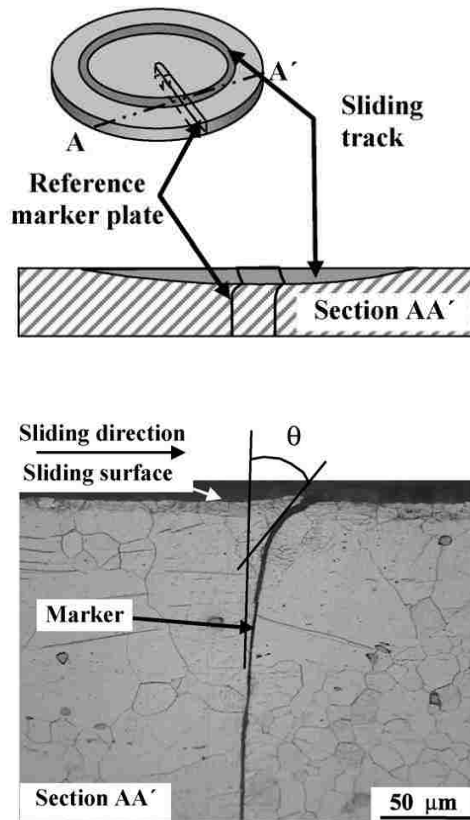
Figure 2.29. (a) Geometry of the marker inserted in the sample (disc) and the cross-section AA`representing the displacement of the marker underneath the contact surface after the sliding wear test and (b) Cross-sectional optical micrograph showing the displacement of the marker towards the sliding direction after sliding for 50 cycles at 673K. [65]
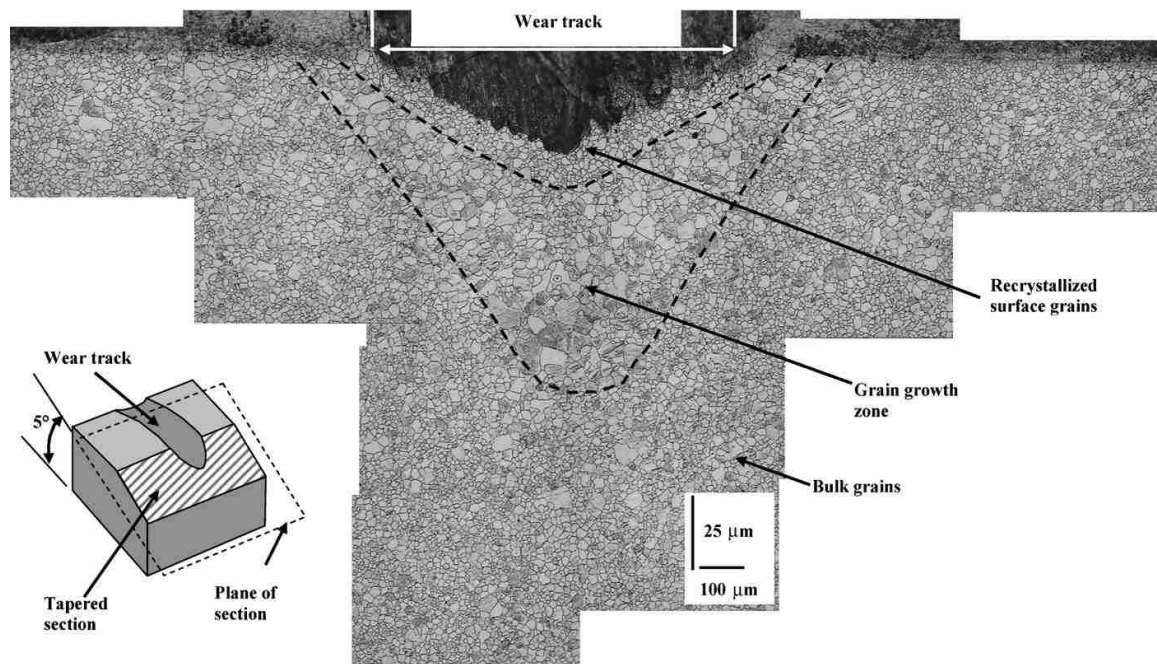
Figure 2.30.Subsurface microstructure of the worn samples developed after sliding for 50 cycles at 673K. Micrograph indicates presence of a thin recrystallized zone and an extensive grain growth zone. This micrograph was taken from a tapered section of the wear track where the section plane was at an angle of 5°to the horizontal axis (inset) [65].
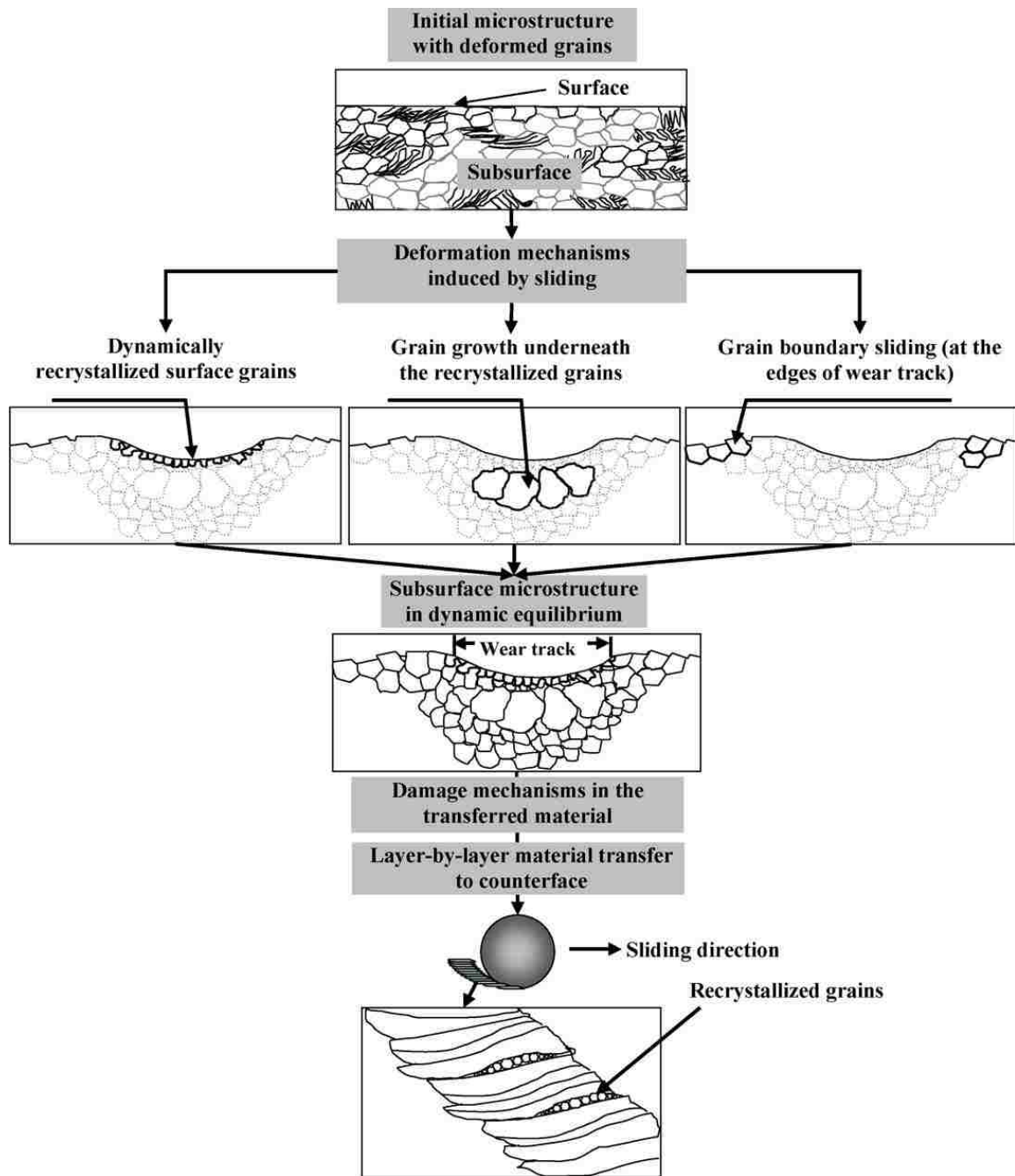
Figure 2.31.Schematic diagram summarizing sliding-induced microstructural events observed under the contact surfaces as well as in the debris fragments generated at 673K [65].
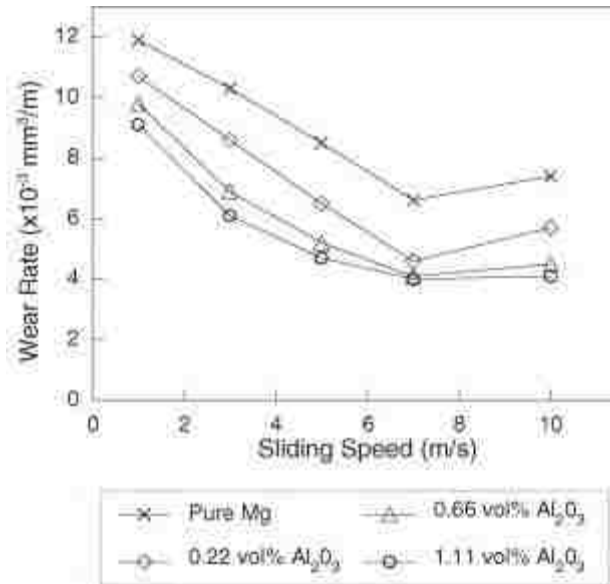
Figure 2.32. Variation of wear rate with sliding speed for pins of pure magnesium and magnesium composites containing 0.22, 0.66 and 1.11 vol.% nano-sized Al_2O_3 particulates during dry sliding against tool steel discs [70].
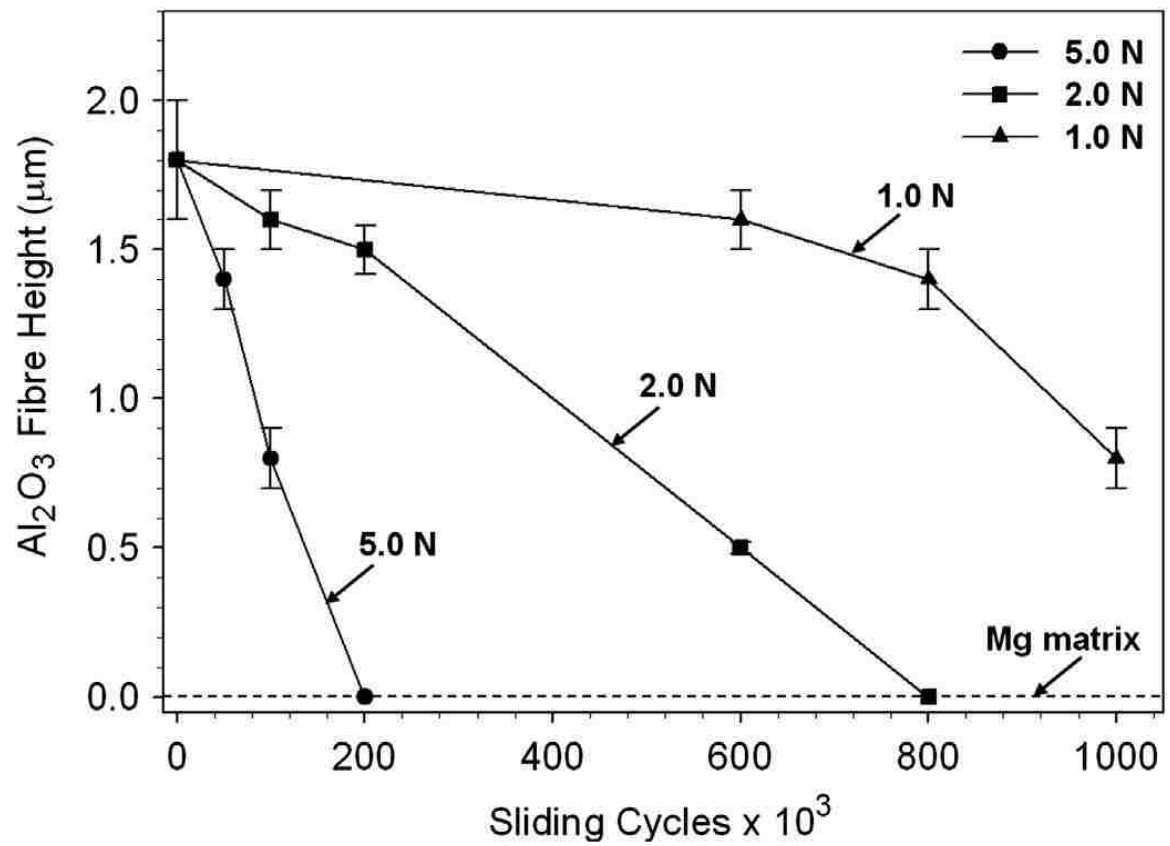
Figure 2.33. Plot of variation of Al_2O_3fibre height with sliding cycles at 1.0 N, 2.0 N and 5.0 N for AM60−9% $(Al_2O_3)_f$ composite at 25 °C [71].
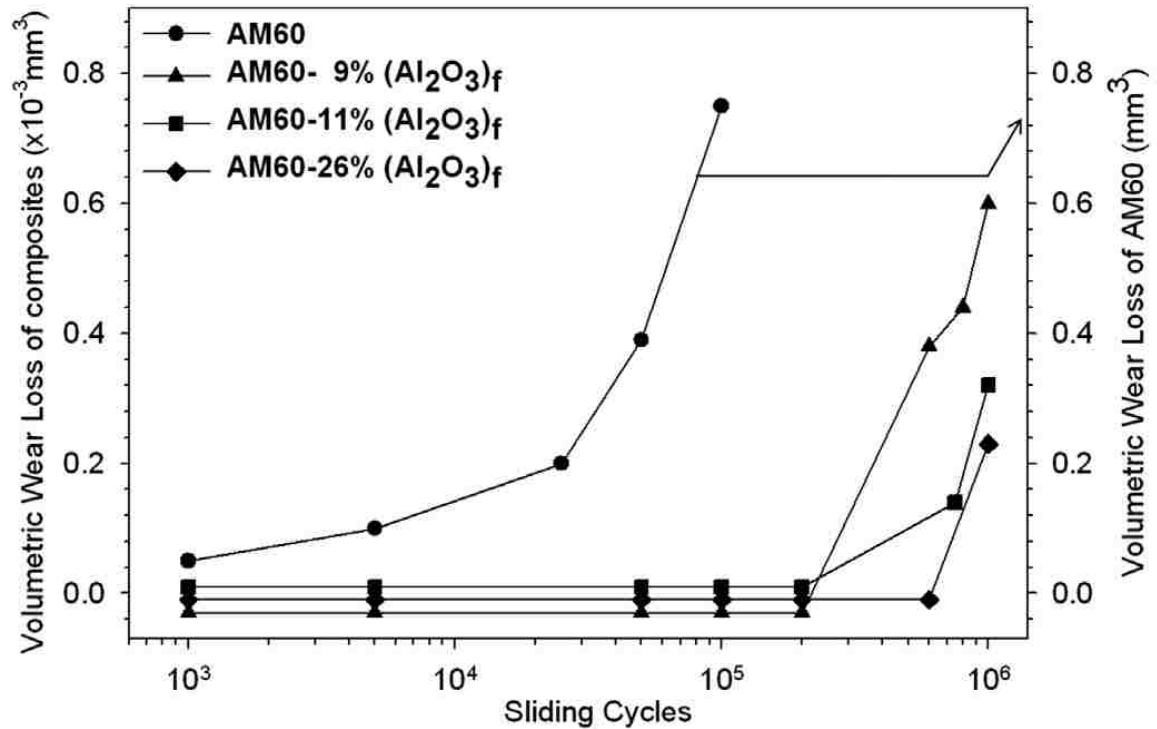
Figure 2.34. Volumetric wear loss (in mm^{3}x 10^{-3}) vs. sliding cycles at 2.0 N load indicating the effect of Al$_2$O$_3$fibre volume percentage on the rate of material removal. Higher volumetric wear loss occurred after 6 x 10^{-5} cycles for AM60–26% (Al$_2$O$_3$)$_f$ as opposed to after 2 x 10^5 cycles for AM60–9% (Al$_2$O$_3$)$_f$ and AM60–11% (Al$_2$O$_3$)$_f$. Note the different scale used to indicate the volumetric wear loss of AM60 (mm^3) [71].
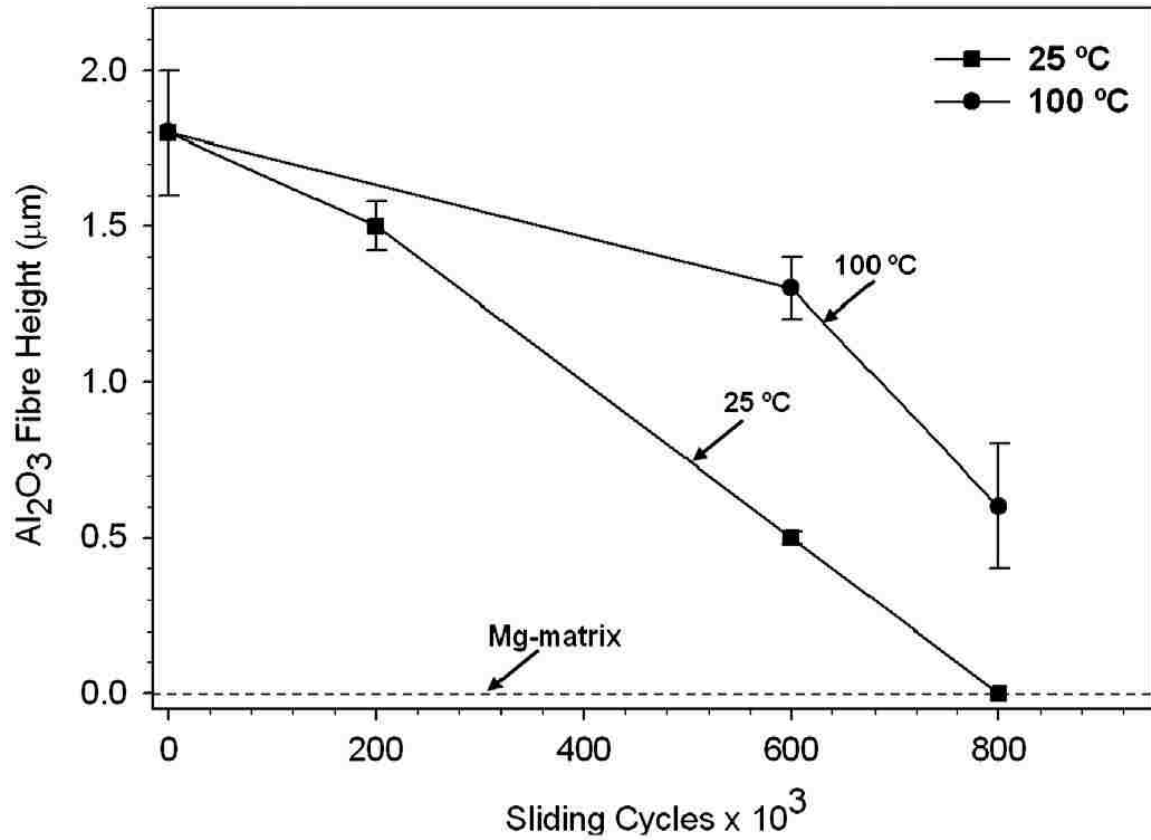
Figure 2.35. Plot of variation of Al_2O_3 fibre height with sliding cycles at 25 °C and 100 °C under a load of 2.0 N for AM60−9% $(Al_2O_3)_f$ composite [71].

2.6 Summary

A large amount of research work has been carried out on the dry sliding wear of the Mg alloys. However, the research work lacks in presenting databases describing the tribological behaviour of Mg alloys and composites over a range of loads and velocities. Hence, there is a need to study the wear mechanisms of Mg alloys and composites by means of wear mechanism maps. Therefore the next few chapters outlining the current research will discuss:

(i) A squeeze casting technique for production of high quality Mg composites.

(ii) Dry sliding wear tests carried out on Mg alloy AM60 and its composite AM60- 9% $(Al_2O_3)_f$.

(iii) Wear mechanism maps for unreinforced AM60 alloy and its composite AM60- 9% $(Al_2O_3)_f$.

(iv) A detailed description of the various wear mechanisms of AM60 alloy and its composite AM60- 9% $(Al_2O_3)_f$.

Chapter 3: Experimental methodology

3.1 Introduction

Experimental details are described in the chapter. These include the fabrication of AM60-9% $(Al_2O_3)_f$ using the squeeze casting technique ; the casting process and parameters. This is followed by the description of the block-on-ring tribometer, used to conduct the sliding wear tests, the parameters used and the surface characterization techniques employed to investigate the wear mechanisms. An outline of the experimental methods used in this work is shown in figure 3.1.

3.2 Fabrication of Mg composites through squeeze casting technique

The materials fabricated for this work include:

1. Mg alloy AM60 (matrix) with a composition (wt. %) Al: 5-6%, Zn: 0.2%, Mn: 0.4%, Si: 0.1%, Cu: 0.01% and the balance Mg.

2. Mg alloy AM60 reinforced with alumina fibres- AM60- 9% $(Al_2O_3)_f$.

The composite was prepared by squeeze casting technique using saffilfibres (97% Al_2O_3, 3% SiO_2 obtained from Saffil Inc. and Thermal Ceramics Inc. The preforms were made by grinding the fibres into a powder form, flocculating the powder with water, polyacrylic amide and binder. The resulting solution was stirred thoroughly overnight followed by compressing and drying the mixture into a 2.5 cm thick and 10 cm diameter disc and as shown in figure 3.2 (a) and (b). The preform volume was calculated using the following formula (eq.3 .1) in table 3.1.

$$(Al_2O_3)_f\% = \frac{\rho_{preform}}{\rho_{Al_2O_3}} \tag{3.1}$$

where, $\rho_{preform}$ and ρ_{fibre} are the densities of preform and the Al_2O_3 fibres/particles constituting the preform respectively. The preform was heat treated to evaporate water, polyacrylic and binder (Table 3-2).

Figure 3.3 shows the casting machine used for the squeeze casting of the composite along with furnace used for preheating the preform and melting the matrix alloy. During the casting process, both the upper and the lower dies of the squeeze casting machine were preheated to 350 ℃. The preform and the Mg alloy were heated to 450 ℃ and 750 ℃ respectively before pouring them into the lower die. The casting parameters are shown in table 3-3. These castings were made in the Casting lab (120A) in Centre for automotive research and education, University of Windsor by Xuezhi Zhang headed by Dr. Henry Hu, Department of Mechanical, Automotive and Materials Engineering (MAME), University of Windsor.

The microstructures of the alloy and the composite used to conduct the dry sliding wear tests are shown in figure 3.4(a) and (b) respectively. The alumina fibres reinforced in the composites were found to be protruded up to a height of 1.5 ± 0.3 μmμm using an optical surface profilometer WYKO NT-1100 (Fig. 3.6).
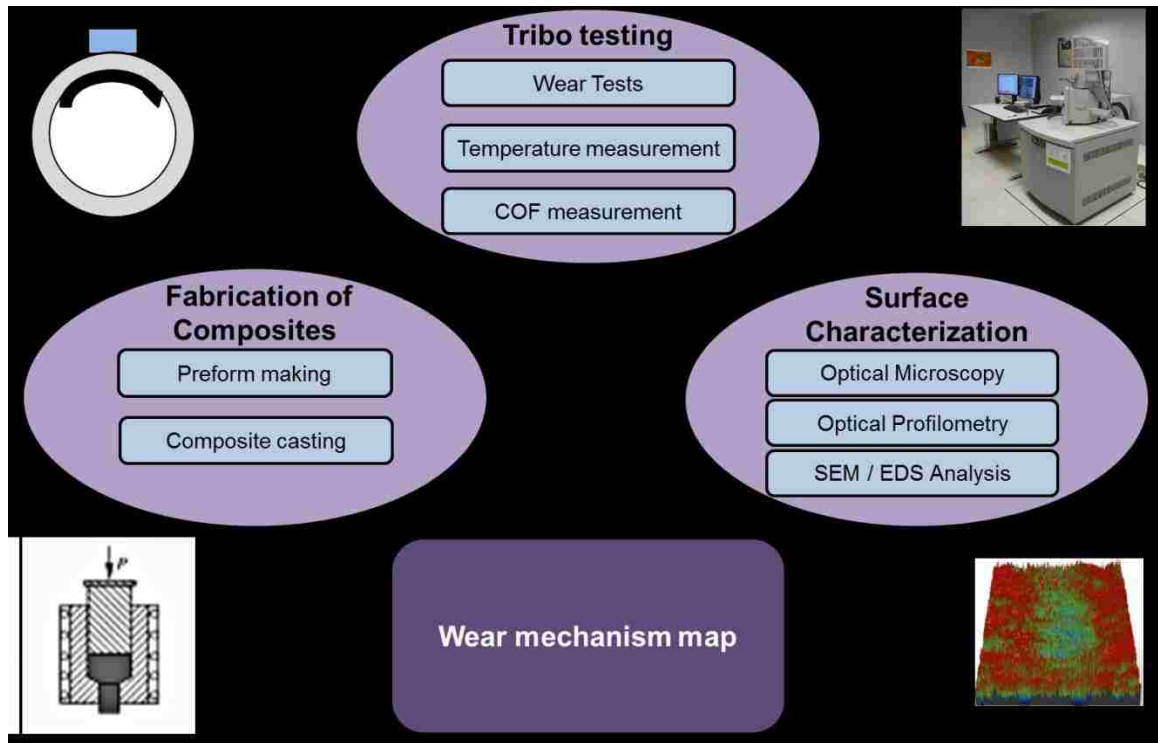
Figure 3.1 Experimental methodology of the current research work.

(a)
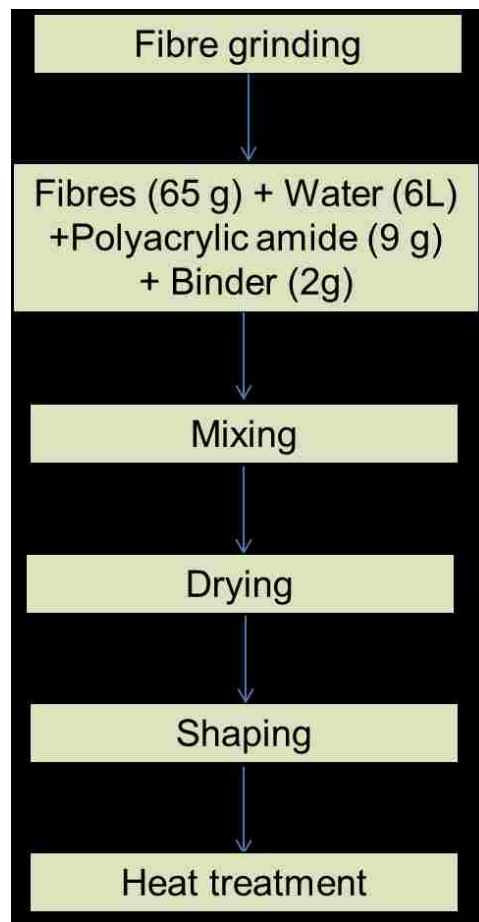
(b)

Figure 3.2. (a) Schematic presentation of preform making (b) Flowchart showing the process of preform making

Table 3-1. Determination of preform volume percentage.

Weight of perform (g)	Volume of preform (cm^3)	$\rho_{preform}$ (g/cm^3)	ρ_{Al2O3} [82] (g/cm^3)	Al$_2$O$_3$ fibre %
70.72	196.25	0.36	3.96	9.13

Table 3-2. Preform heat treatment cycles.

Temperature (°C)	Duration
200	3 hours
400	15 minutes
750	30 minutes
1000	15 minutes
1100	15 minutes
1200	1.5 ~ 2 hours

Figure 3.3.Furnace and hydraulic press used for squeezed casting

Table 3-3. Casting parameters adopted during squeeze casting.

Hydraulic Press Capacity (Tons)	Pressure applied (MPa)	Duration of applied pressure (s)
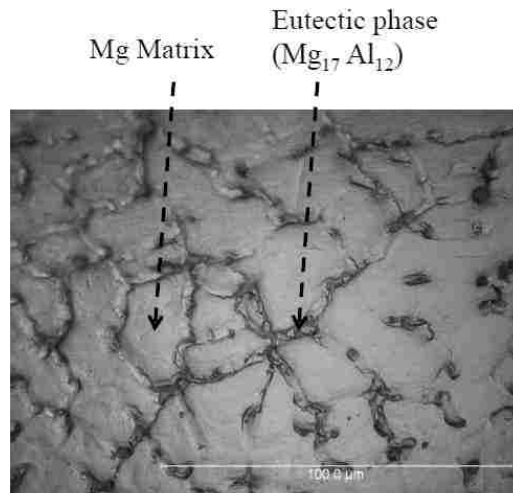
(a)
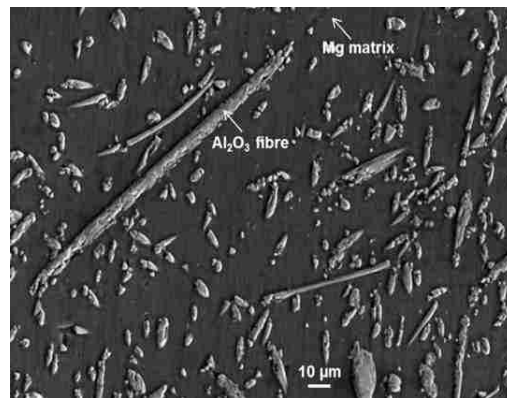
(b)

Figure 3.4. Microstructure of (a) AM60 alloy polished and etched with Glycol (1 ml HNO_3(conc.), 24 ml water, 75 ml ethylene glycol) (b) AM60-9% $(Al_2O_3)_f$ composite.
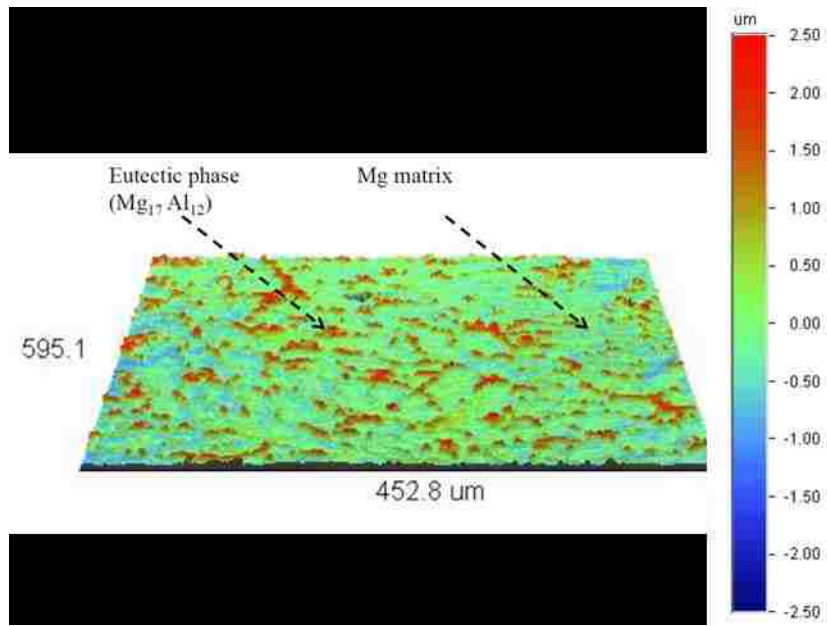
Figure 3.5. Optical profilometry image of AM60 alloy
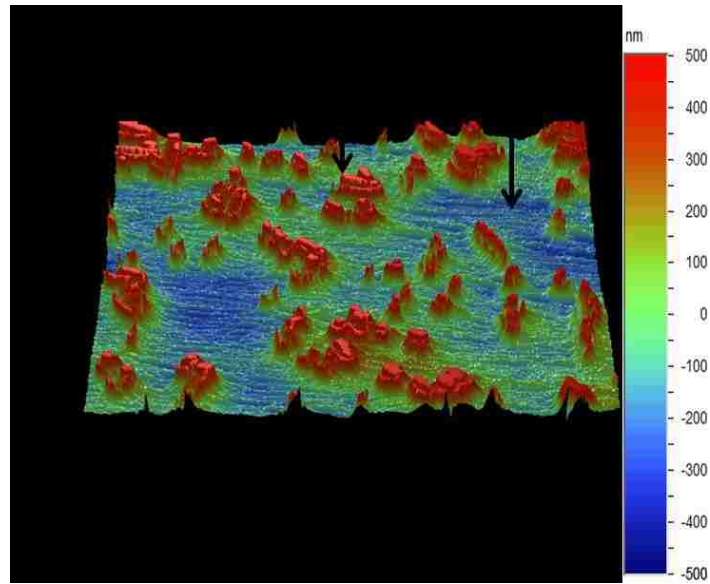
(a)
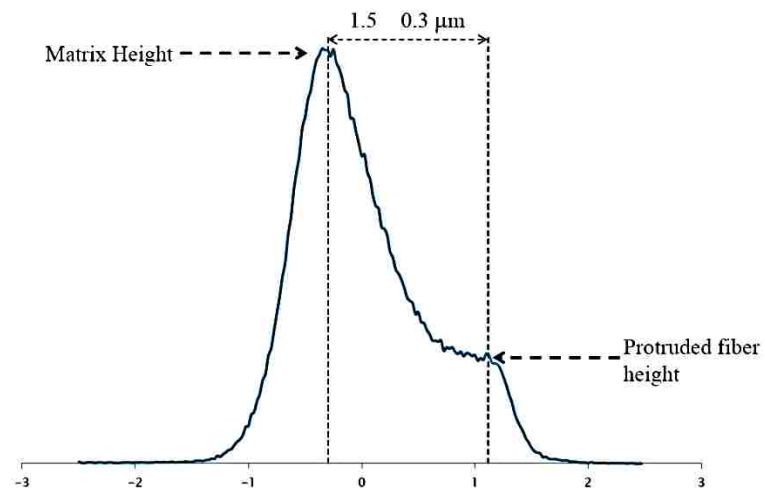
(b)

Figure 3.6. (a) Optical profilometry image for AM60- 9% $(Al_2O_3)_f$ (b) Histogram showing Al_2O_3fibre height protruded from the surface of AM60-9% $(Al_2O_3)_f$ composite.

3.3. Sliding wear tests

A block-on-ring type tribometer was used to perform dry sliding wear tests using 10 x 10 x 5 mm^3 blocks made of AM60 alloy and AM60- 9% $(Al_2O_3)_f$ composite against counterface slider rings made of AISI 52100 grade steel. The specimens were made from the as cast AM60 alloy ingot and squeeze cast AM60- 9% $(Al_2O_3)_f$ composite. Conventional magnesium alloy polishing techniques were used to prepare the sliding surfaces of the specimens. The procedure consisted of grinding the surfaces manually to 1200 grit SiC papers followed by polishing with 1 and 0.1 μm alumina powder slurry. The polished surfaces were ultrasonically cleaned using ethanol. The counterface rings used for the experiments were also polished and cleaned before each wear tests using the same procedure. The width of the rings was 12 mm. The outer diameter was 38 mm. The wear tests were performed at linear velocities ranging from 0.1 to 1.5 m/s and a load range of 0.1 to 250 N (Table 3-4). The load was applied through dead weights.

The block on ring tribometer (Fig. 3.7) was equipped with a data acquisition system that consisted of a multifunction analog-to-digital conversion board connected to a computer. The data acquisition system was used to measure the coefficient of friction (COF) between the sliding surfaces and the resulting interface temperature of the specimens. The temperatures were measured using a grounded chromel-alumel type thermocouple probe with a stainless sheath of diameter 0.25 mm. The probe was inserted into the specimen through a hole drilled slightly larger than the diameter of the thermocouple at about 1.0 mm away from the sliding surface.

3.4. Observation of the worn surfaces
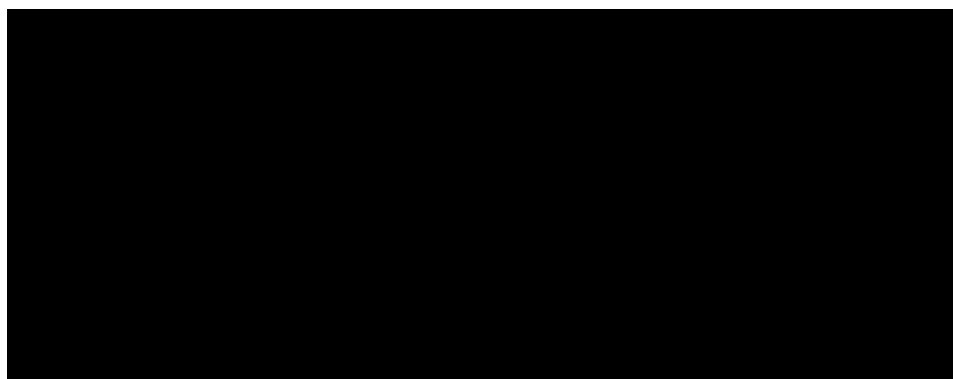
The wear features were quantified using two different techniques. For significant amount of wear loss, mass loss method was employed to calculate the wear rates. The mass losses were calculated from the difference in weights of specimens measured before and after the sliding tests to the nearest 10^{-5} g using an analytical balance. The mass of the worn specimens was measured after removing the loose debris from the worn surfaces using ethanol in an ultrasonic cleaner. For mass losses less than 10^{-5} g, i.e. ultra-mild wear, volumetric wear losses were measured using a white light optical profilometer (WYKO NT-1100). Optical profilometry calculations were employed to determine the material removal rates in the composites according to the reference [36]. The amount of material removal associated with the groove formations along the wear track were detected in this way. The amount of material removed was obtained from an area, A, by calculating the cross-sectional area that fell below a reference position with respect to unworn Mg matrix. The worn area was calculated using optial profilometry observations, with four readings from each image (Fig. 3.8), where the area beneath the reference line was calculated to be the worn area. An average of 24 readings (from six different regions of the wear track) was taken as the worn area A_{ij} and was multiplied by the perimeter of the wear track, which gives the volumetric wear loss W according to the equation 3.1 [36]:

$$W = \frac{2}{n} \pi R w \left[\sum_{i=1}^{n} \quad \sum_{j=1}^{k} \quad A_{ij} \right] \tag{3.3}$$

where, k is the number of grooves per section and n=24: the number of different sections along the wear track from which measurements were made.

The worn surfaces were observed using a digital optical microscope Keyence and a scanning electron microscope (SEM), JEOL 6400, equipped with an energy dispersive spectrometer (EDS) using both the secondary electron and the backscattered modes.

Table 3-4 Test parameters for dry sliding wear tests.
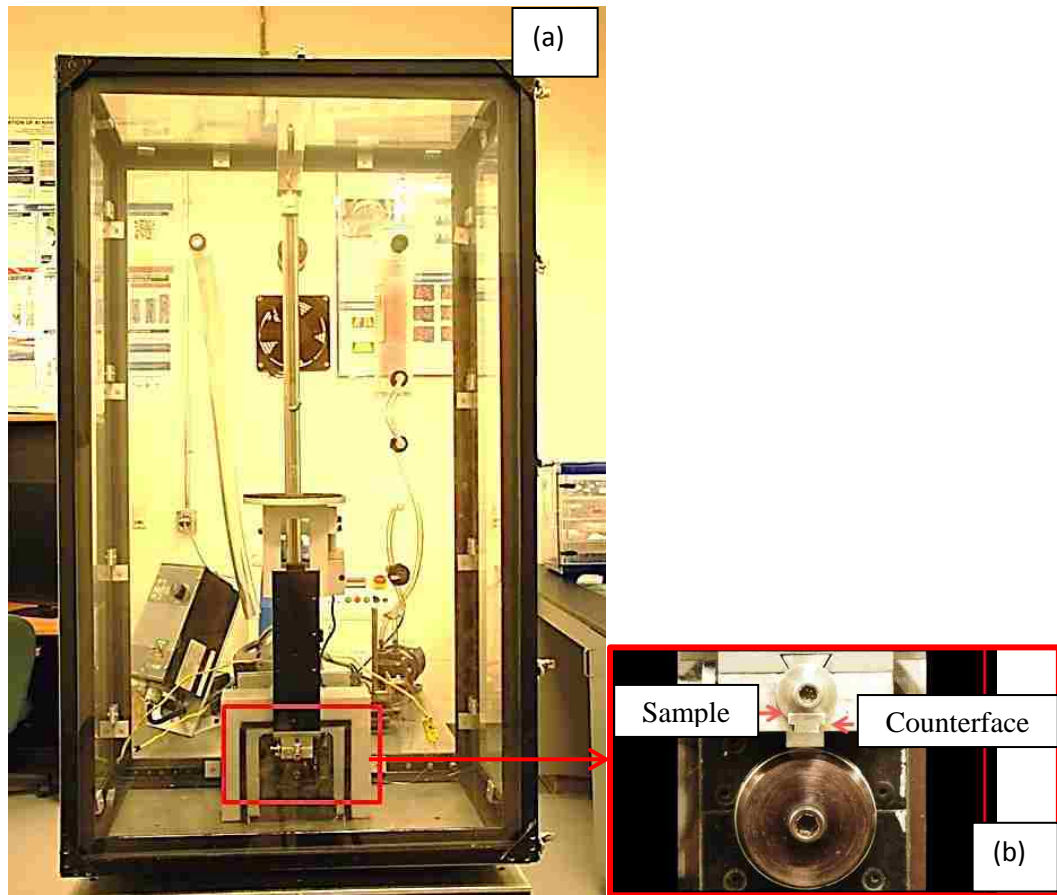
Figure 3.7.(a) A block on ring tribometer. (b) Enlarged figure showing the block-on-ring configuration.

600 µm
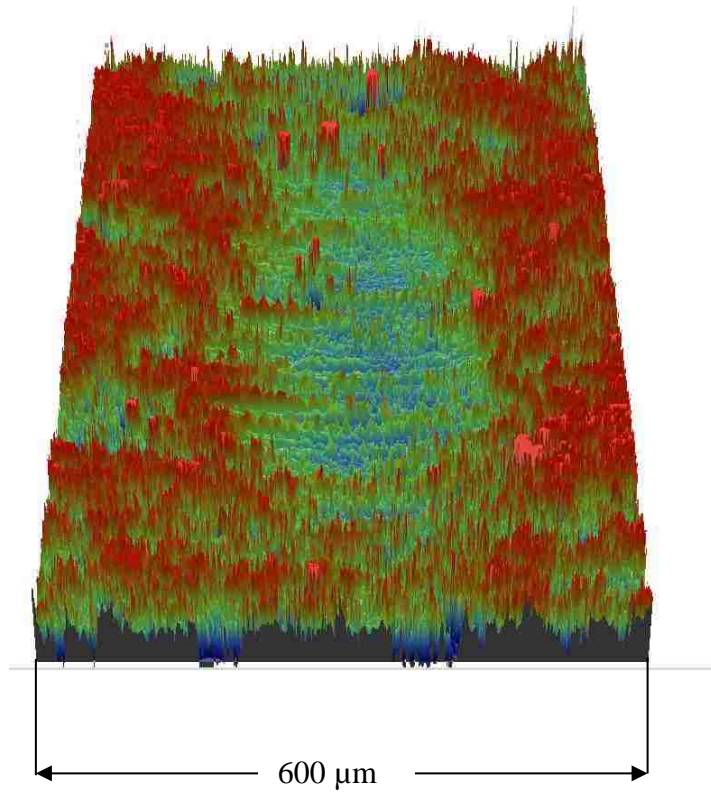
Figure 3.8.Optical profilometry image for worn surface of AM60 alloy.

Chapter 4: Results

4.1. Introduction

In this chapter, results of the wear tests conducted on Mg alloy AM60 and its composite AM60- 9% $(Al_2O_3)_f$ are presented. The chapter starts by reporting the results of the tests that were carried out at a load range of 0.1 to 250.0 N and velocities varying from 0.1 to 1.5 m/s on AM60 alloy and AM60- 9% $(Al_2O_3)_f$ composite. This is followed by the construction of wear map for both materials. The wear mechanisms controlling the wear rates in each regime are then discussed. COF and temperature maps have also been constructed showing the correlation of wear with both temperature and COF. Forced cooling experiments have also been presented to show the dependence of wear transition on temperature.

4.2. Dry sliding wear of unreinforced AM60 alloy and AM60- 9% $(Al_2O_3)_f$ composite

4.2.1. Mass loss – Sliding distance curves

Wear of AM60 alloy was investigated by studying the relationship between the volumetric wear loss and sliding distance at loads ranging from 0.1 to 250.0 N at sliding velocities of 0.1 to 1.5 m/s. For loads lower than 1.0 N and velocities less than 0.5 m/s, volumetric wear losses were measured using optical profilometer WYKO NT-1100. For loads greater than 1.0 at all velocities, wear was high enough to be measured using the mass loss method. The measured mass losses were then used to calculate volumetric losses using the densities of the alloy. Figures 4.1 to 4.6 show volumetric losses vs. sliding distance curves at different applied loads for sliding velocities of 0.1, 0.2, 0.3, 0.5, 1.0 and 1.5 m/s. Each point on these plots represents an individual test carried out at that particular load and speed for a certain sliding distance.

Figure 4.1 shows linear increase in volumetric loss for all loads with increasing the sliding distance at 0.1 m/s. The same trend is followed at 0.2 m/s. Thus, the relationship between applied load and sliding distance remained linear at the highest applied load, i.e. 237.8 N for velocities up to 0.2 m/s. However, tests conducted at the velocity of 0.3 m/s (Fig. 4.3), a change in slope occurred at the highest applied load, i.e. 237.8 N while at lower loads, a linear relationship between the volumetric loss and the sliding distance was maintained. As the velocity is increased (Figure 4.4-4.6) the load, at which volumetric loss-sliding distance curve shows a change in slope, decreases. At 0.5 m/s, the change in slope was first observed at 150.0 N. At 1.0 m/s change in the slope occurred at 100.0 N, and at 1.5 m/s change occurred at 80.0 N. The change of the slope indicates change in the wear behaviour of AM60 alloy.

A similar behaviour is shown by AM60- 9% $(Al_2O_3)_f$ composites. From velocities ranging from 0.1 to 0.3 m/s, the volumetric loss-sliding distance plots were linear. A change from constant slope first occurred at 150.0 N at 0.5 m/s, 70.0 N at 1.0 m/s and 60.0 N at 1.5 m/s. The delay in the change in the slopes can be attributed to the addition of the reinforcement.

4.2.2. Wear rates

The wear rate at any sliding distance is defined as the volumetric loss of the tested materials per unit sliding distance, thus, the slope of the volumetric loss- sliding distance curve can be taken as the wear rate at that particular load and speed combination. The wear rates calculated from these linear plots are linear. This exhibits "equilibrium wear". These are called steady state wear rates as shown in figure 4.13 (a), hence, called mild wear. The wear rates are dependent on the sliding distance and show two types of wear

behaviour steady state wear for all sliding distances at low load and speed (Fig 4.13 (b)).

The condition, when the sliding distance, at which the steady state wear rate prevails, becomes negligible, is termed as severe wear (Fig. 4.13 (c)).
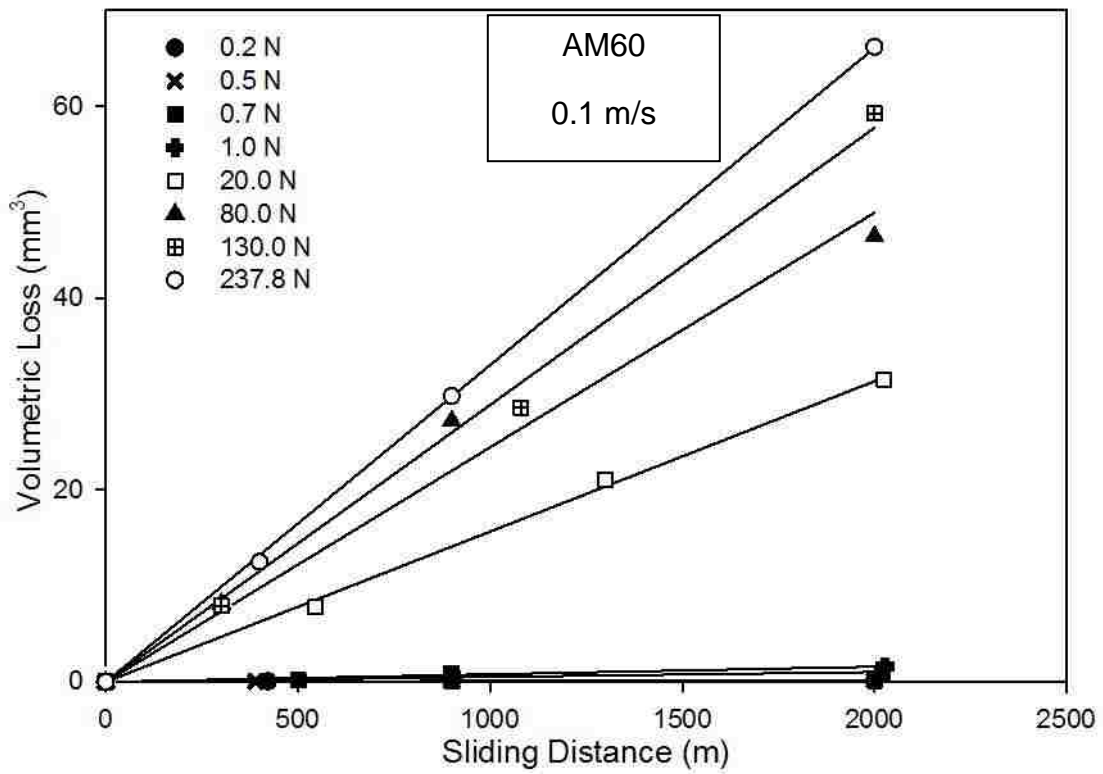
Figure 4.1. Volumetric loss vs. sliding distance plots for various tested loads at 0.1 m/s for AM60 alloy.
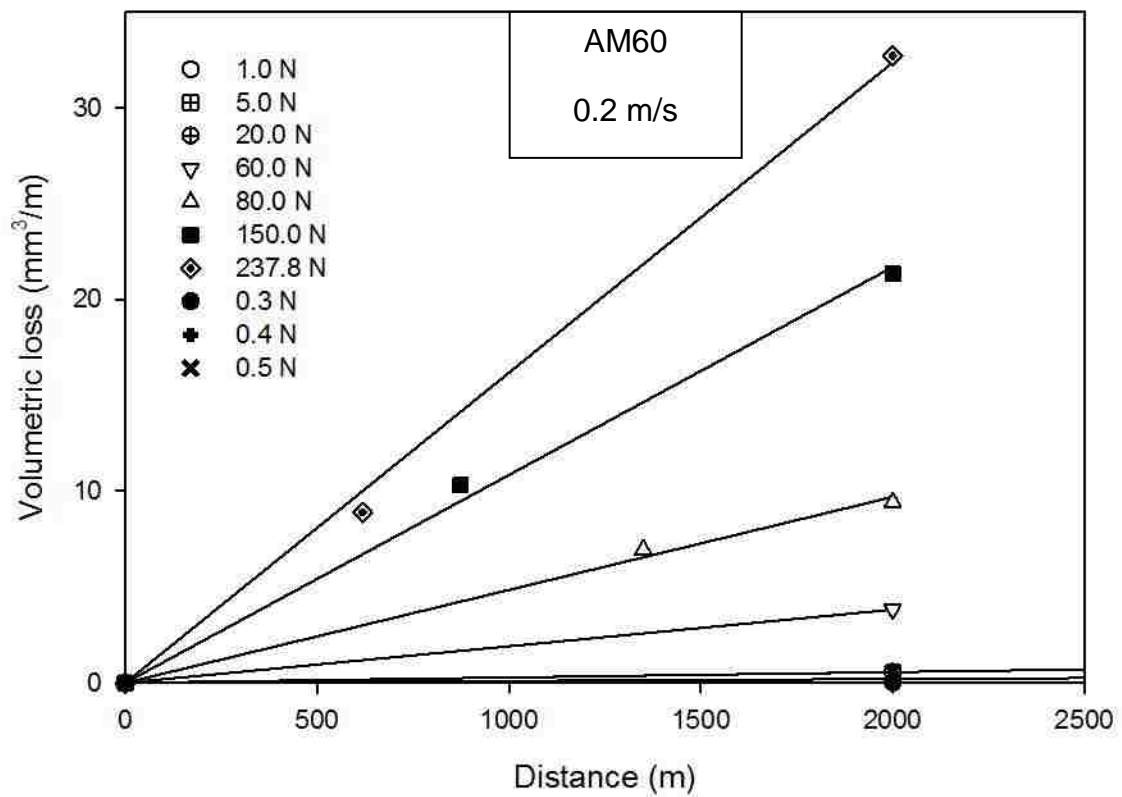
Figure 4.2. Volumetric loss vs. sliding distance plots for various tested loads at 0.2 m/s for AM60 alloy.
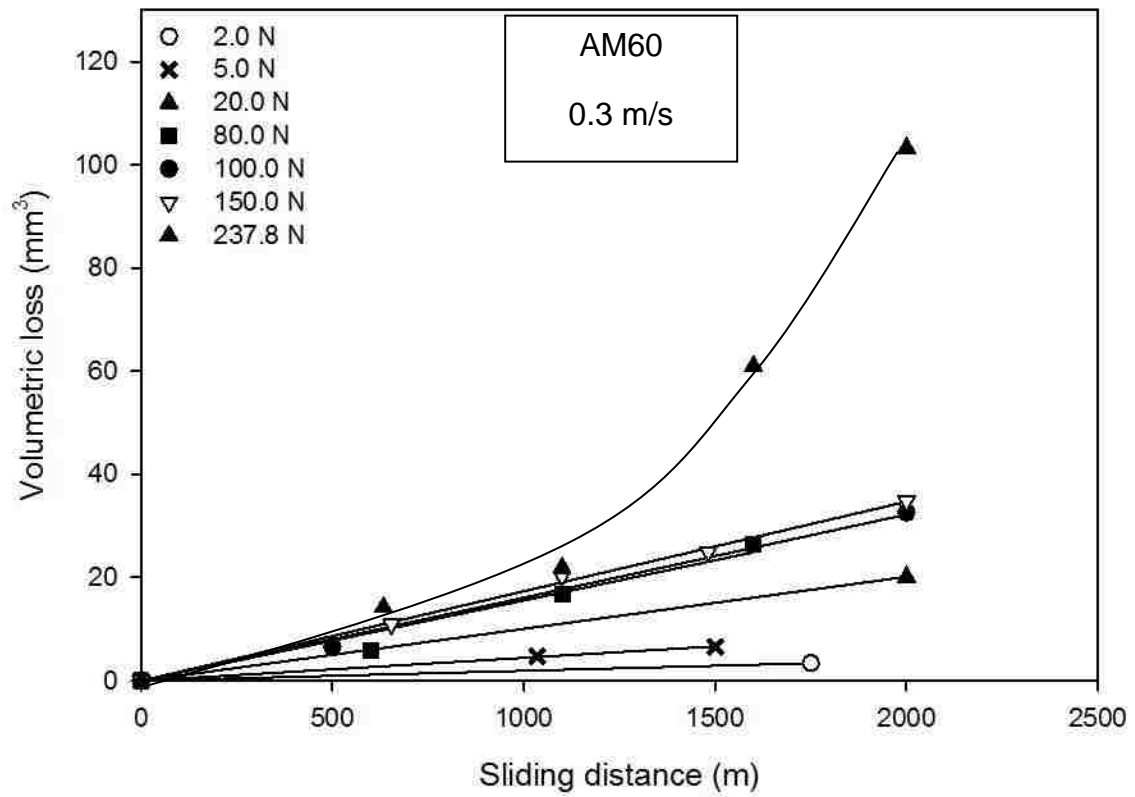
Figure 4.3. Volumetric loss vs. sliding distance plots for various tested loads at 0.3 m/s for AM60 alloy.
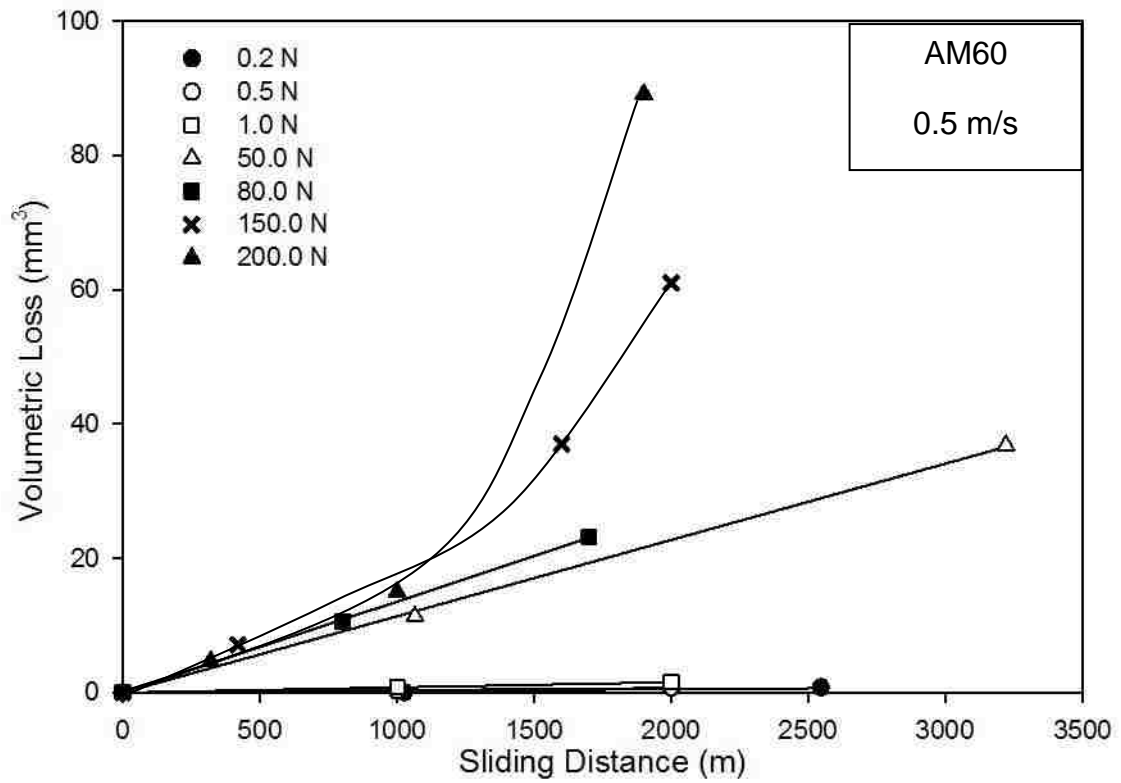
Figure 4.4. Volumetric loss vs. sliding distance plots for various tested loads at 0.5 m/s for AM60 alloy.
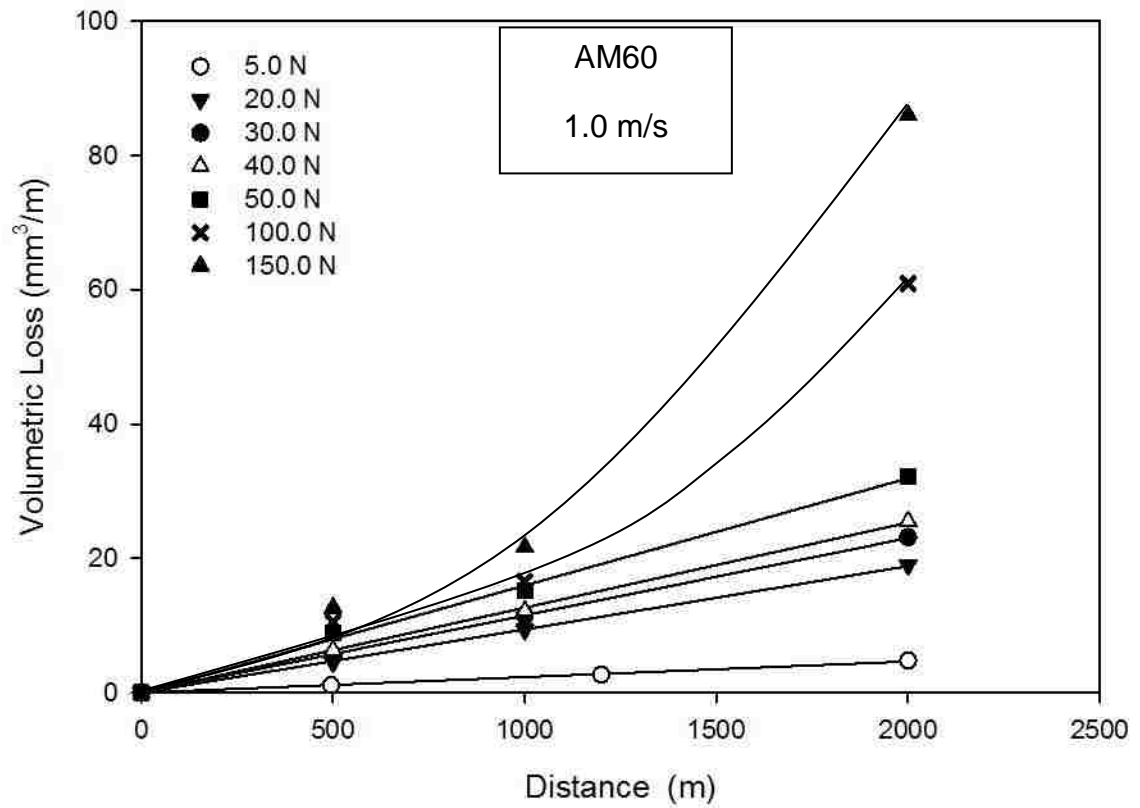
Figure 4.5. Volumetric loss vs. sliding distance plots for various tested loads at 1.0 m/s for AM60 alloy.
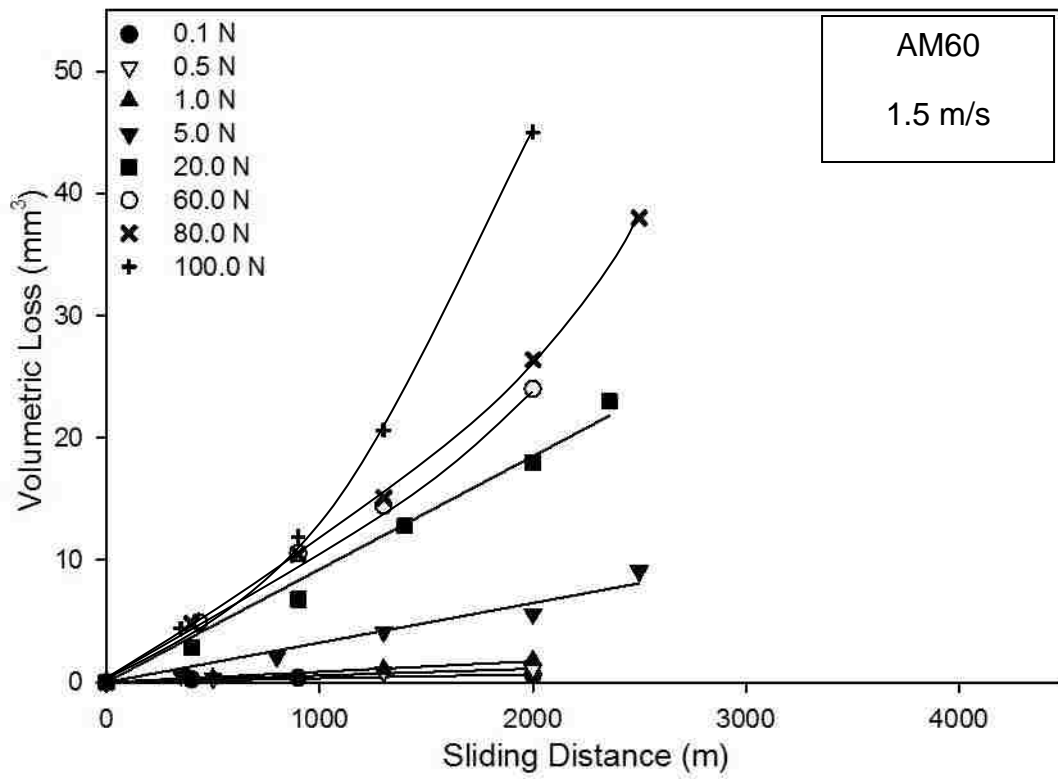
Figure 4.6.Volumetric loss vs. sliding distance plots for various tested loads at 1.5 m/s for AM60 alloy.

Figure 4.7. Volumetric loss vs. sliding distance plots for various tested loads at 0.1 m/s for AM60- 9% $(Al_2O_3)_f$ composite.
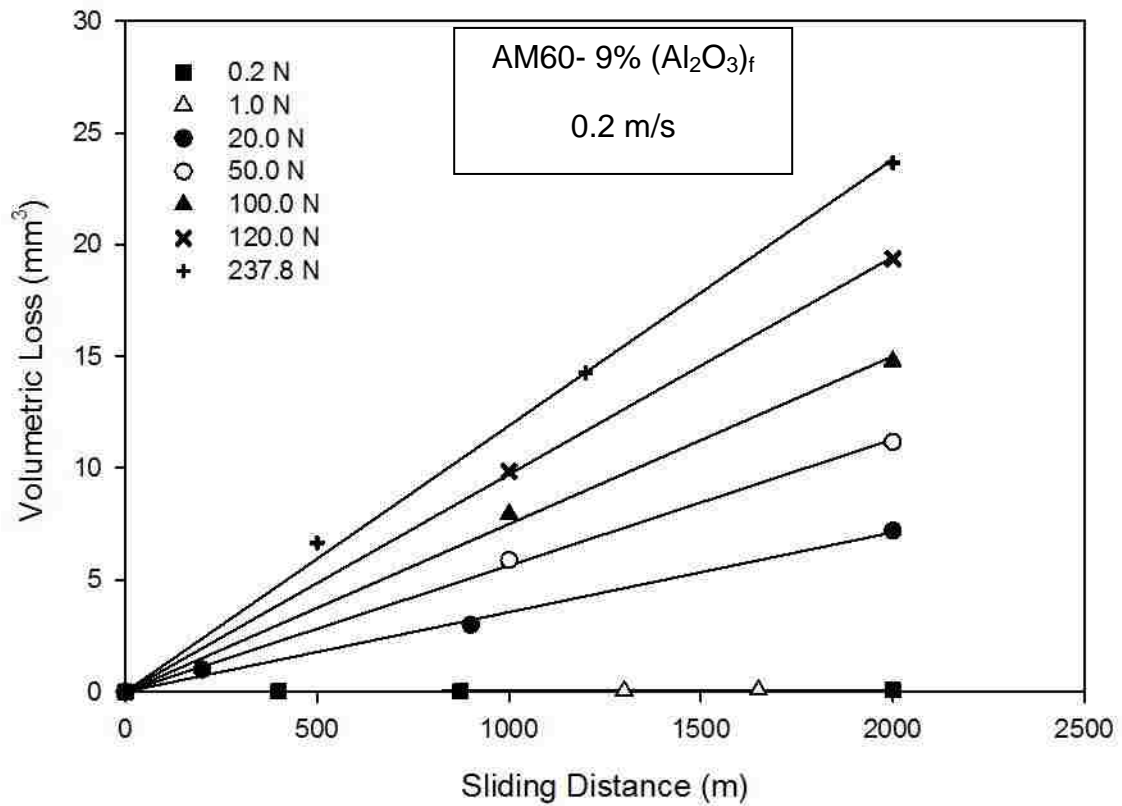
Figure 4.8. Volumetric loss vs. sliding distance plots for various tested loads at 0.2 m/s for AM60- 9% $(Al_2O_3)_f$ composite.
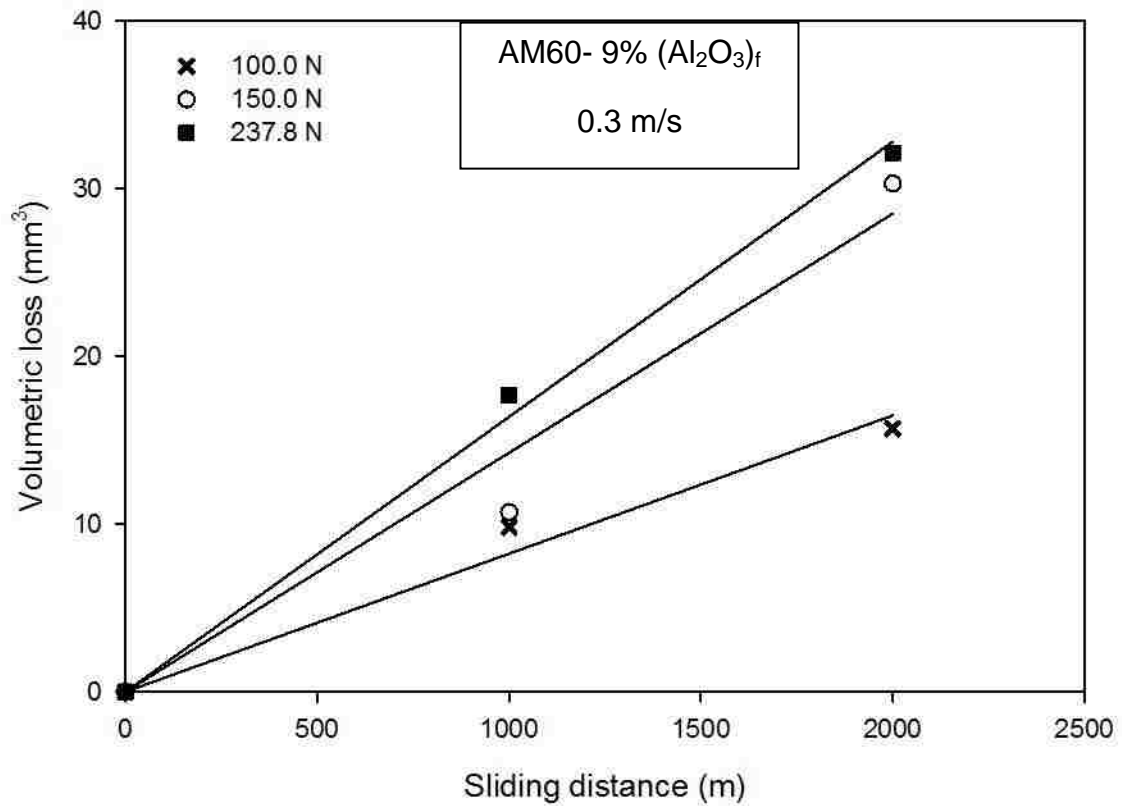
Figure 4.9. Volumetric loss vs. sliding distance plots for various tested loads at 0.3 m/s for AM60- 9% $(Al_2O_3)_f$ composite.
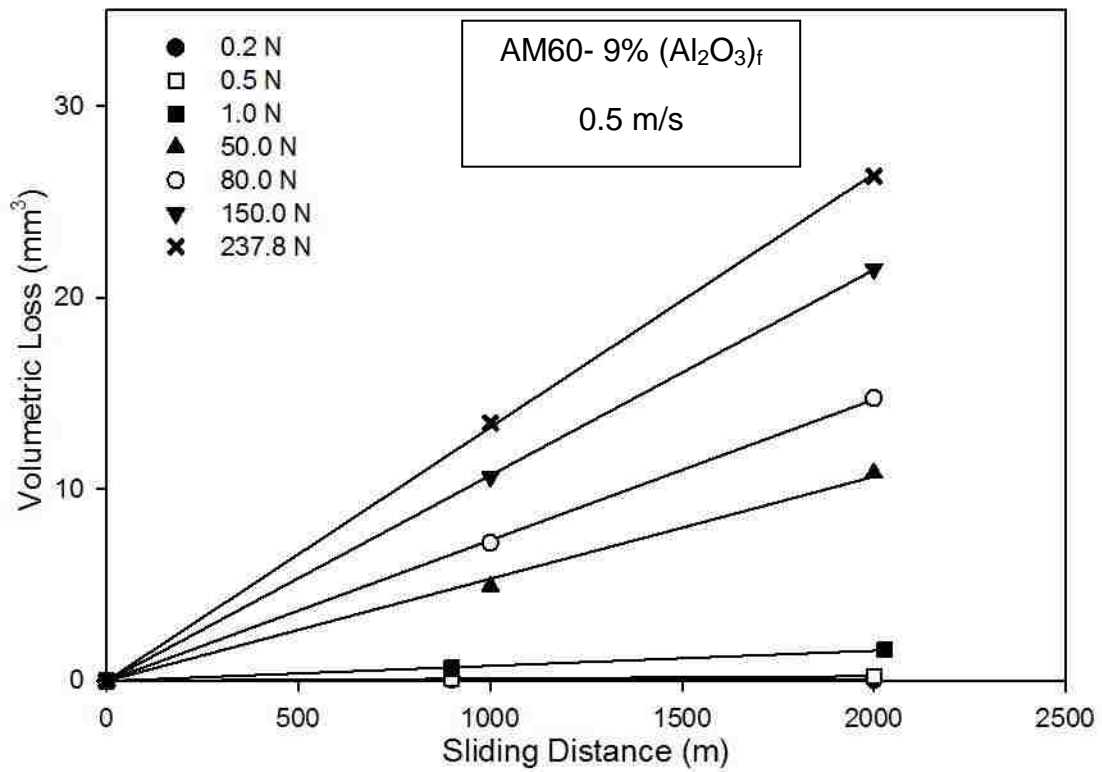
Figure 4.10. Volumetric loss vs. sliding distance plots for various tested loads at 0.5 m/s for AM60- 9% $(Al_2O_3)_f$ composite.
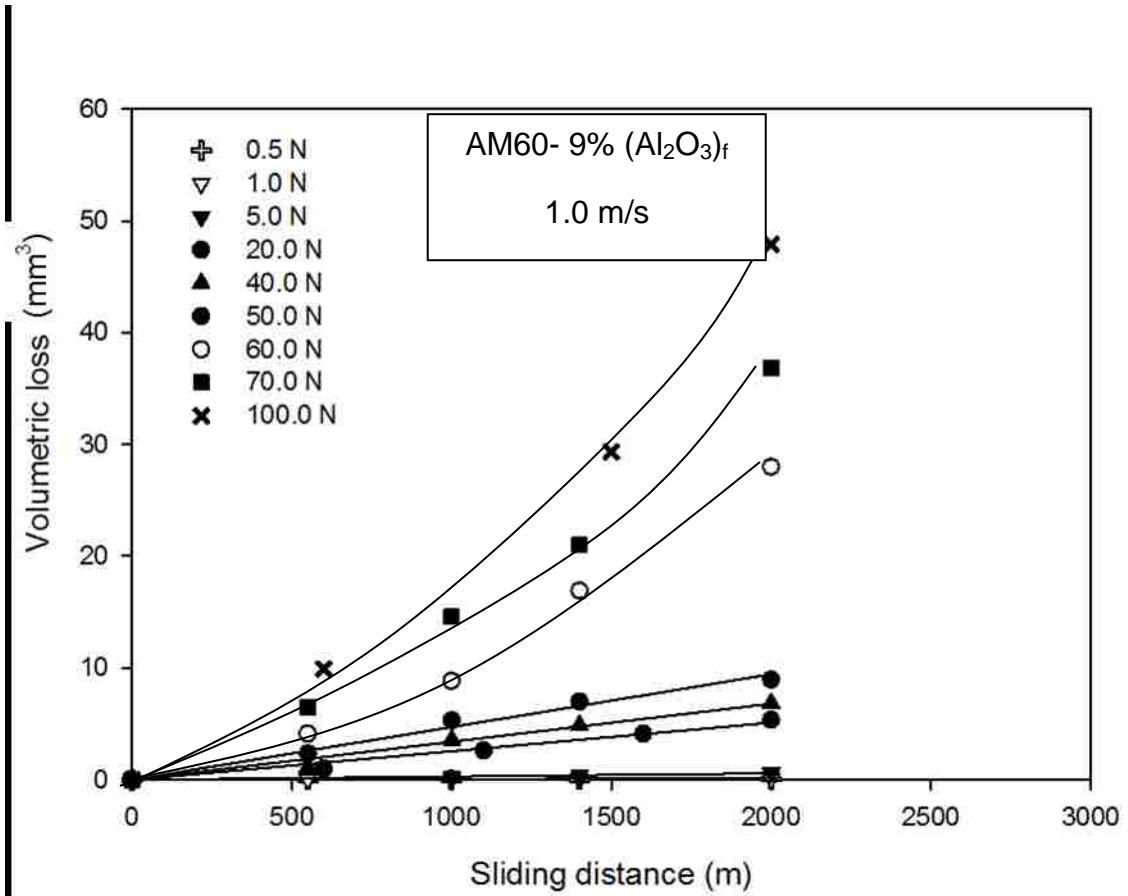
Figure 4.11. Volumetric loss vs. sliding distance plots for various tested loads at 1.0 m/s for AM60- 9% $(Al_2O_3)_f$ composite.

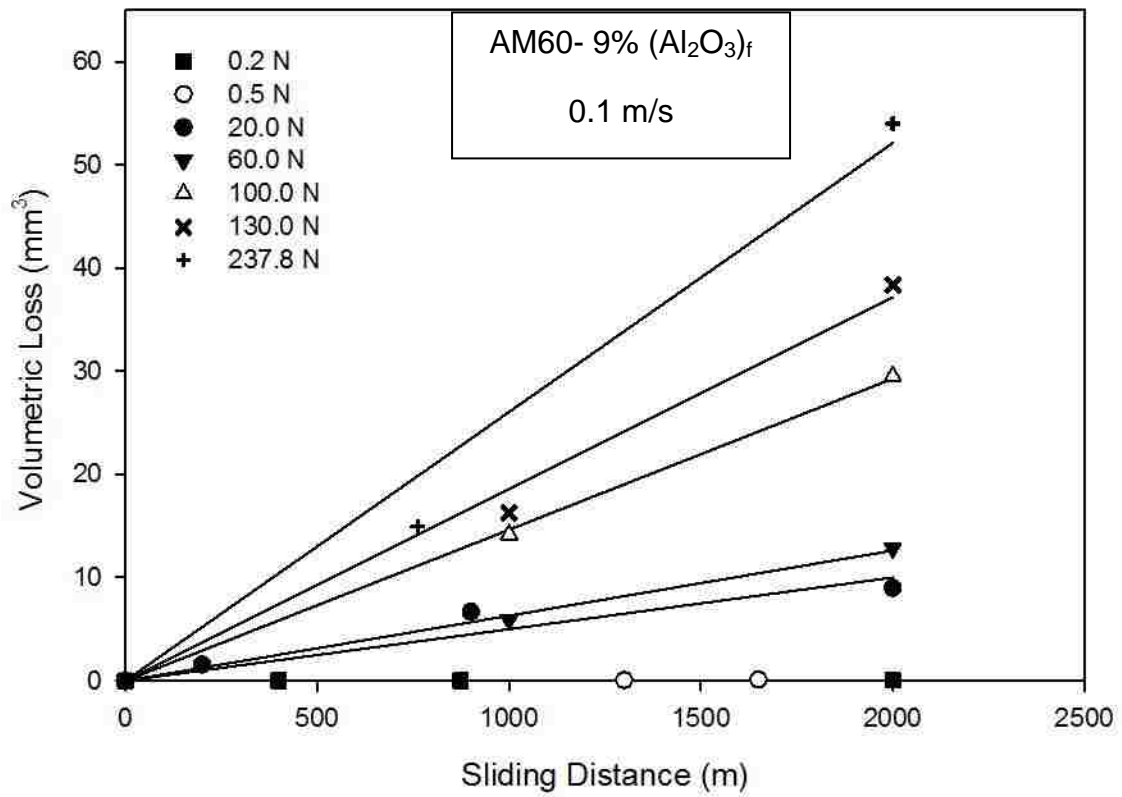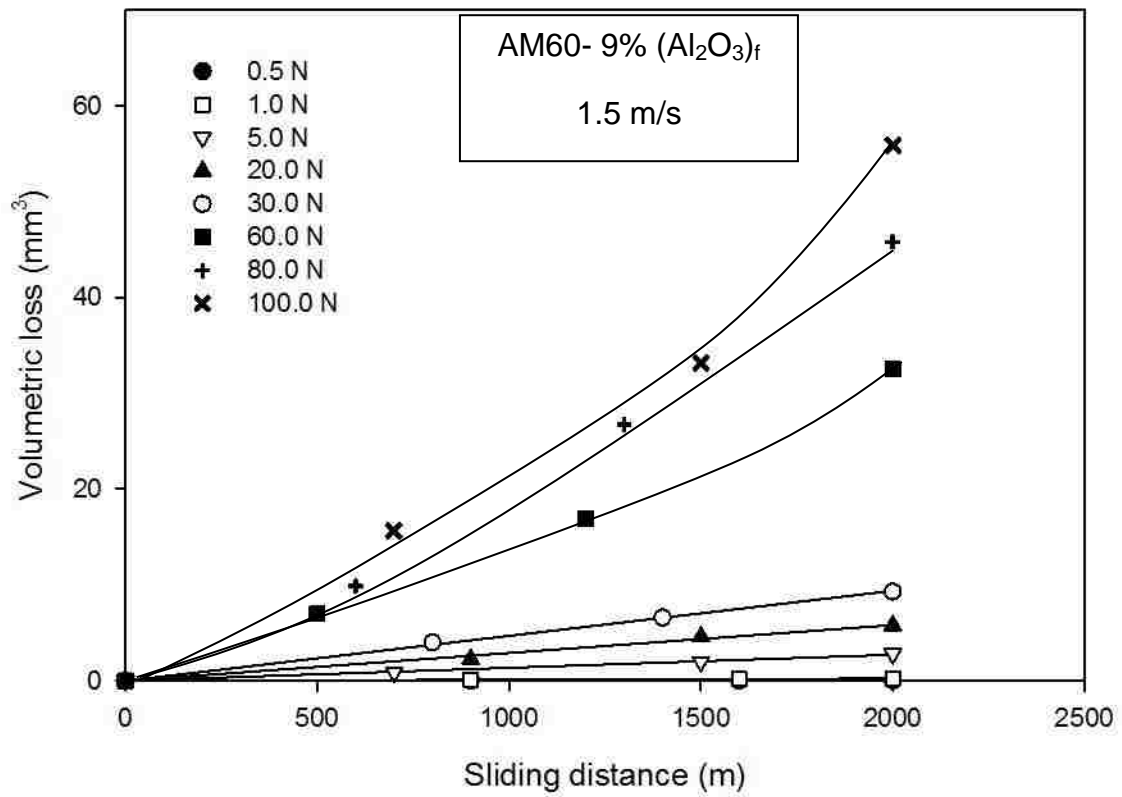Figure 4.12. Volumetric loss vs. sliding distance plots for various tested loads at 1.5 m/s for AM60- 9% $(Al_2O_3)_f$ composite.
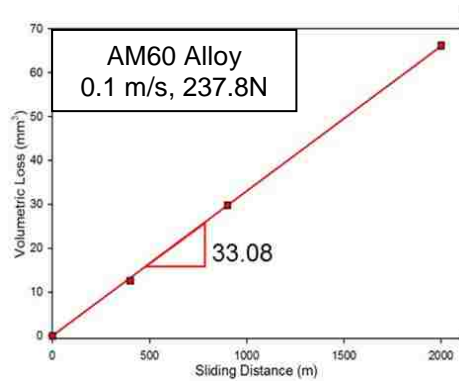
(a)
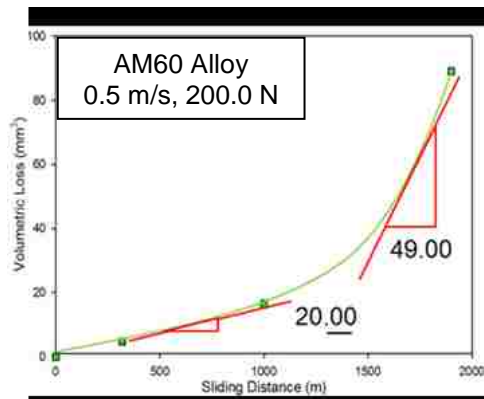
(b)
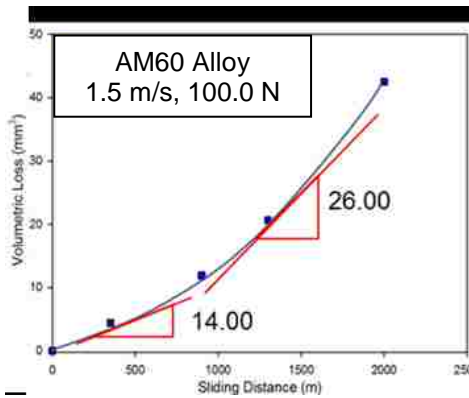
(c)

Figure 4.13. (a) Mild wear or steady-state wear rate (b) Transient or mixed wear (c) Severe wear

4.2.3. Effect of applied load

The wear rates determined as explained in section 4.2.1 are plotted against the applied load at sliding speeds 0.1,0.2,0.3,0.5,1.0 and 1.5 m/s for AM60 alloy (Figure 4.14 – 4.19). Wear rate increases with the applied load for all sliding speeds. However, at 0.3 m/s (Fig. 4.16), the slope of the wear rate vs. load curve changes drastically as compared to 0.1 and 0.2 m/s (Fig. 4.14-4.15). This rise in slope corresponds to the change in slope in volumetric loss vs. sliding distance curve at 238.7 N and 0.3 m/s (Fig. 4.3). The drastic rise in the wear rate is noticeable in all speeds starting from 0.3 m/s to 1.5 m/s (Fig 4.16-4.18) showing a transition from mild to severe wear. Figure 4.19 shows the microstructure of the worn surfaces at different loads at 0.1 m/s. Although the width of the wear tracks show a drastic increase with increasing applied loads, the morphology of the wear tracks remains the same. Oxidized wear debris adhered to the wear track are evident from loads ranging from 0.1 N to the highest applied load of 237.8 N. However, in case of 1.5 m/s (Fig. 4.20), oxide debris are found at loads up 20.0 N only. At 60.0 and 100.0 N, the worn surfaces appear to be free of oxide debris.

Similar behaviour is shown by AM60-9% $(Al_2O_3)_f$ composite on wear rate vs load plots for speeds of 0.1, 0.2, 0.5, 1.0 and 1.5 m/s (Fig. 4.21- 4.25). The drastic increase in wear is noticed at 0.5 m/s and onwards showing a transition from mild to severe wear. This transition is also evident in the microstructures of the worn surface (Fig. 4.26). The worn surfaces corresponding to the loads from 0.2 to 80.0 N show a lackluster morphology while at 150.0 N, shiny metallic worn surface is observed. Similar transition is shown to start from 60.0 N at 1.5 m/s (Fig. 4.27).

When the wear rate vs. load plots for AM60 alloy (Fig. 4.14-4.19) and AM60- 9% $(Al_2O_3)_f$ composite (Fig. 4.22-4.26) are compared, it is evident that the reinforcement plays an important role in increasing the wear resistance of the composite compared with the unreinforced alloy. Under mild wear conditions, the unreinforced alloy shows a maximum wear rate of 33.08 x10^{-3} mm^3/m while AM60- 9% $(Al_2O_3)_f$ composite gets to a maximum wear rate of 25.98 x10^{-3} mm^3/m. The transition from mild to severe wear is first evident at 237.8 N at 0.3 m/s, followed by 150.0 N at 0.5 m/s, 100.0 N at 1.0 m/s and 80.0 N at 1.5 m/s. This can be compared to the AM60- 9% $(Al_2O_3)_f$ composite showing the transition at 237.8 at 0.5 m/s, 60.0 N at 1.0 m/s and 50.0 N at 1.5 m/s. Even in the severe wear regime, the maximum wear rate of 24.52 x10^{-3} mm^3/m for AM60- 9% $(Al_2O_3)_f$ composite is less than half of 54.00 x10^{-3} mm^3/m for AM60 alloy. The delay in transition and the overall reduction in the wear rates of the composites in comparison with the alloy can be attributed to the presence of the reinforcement.
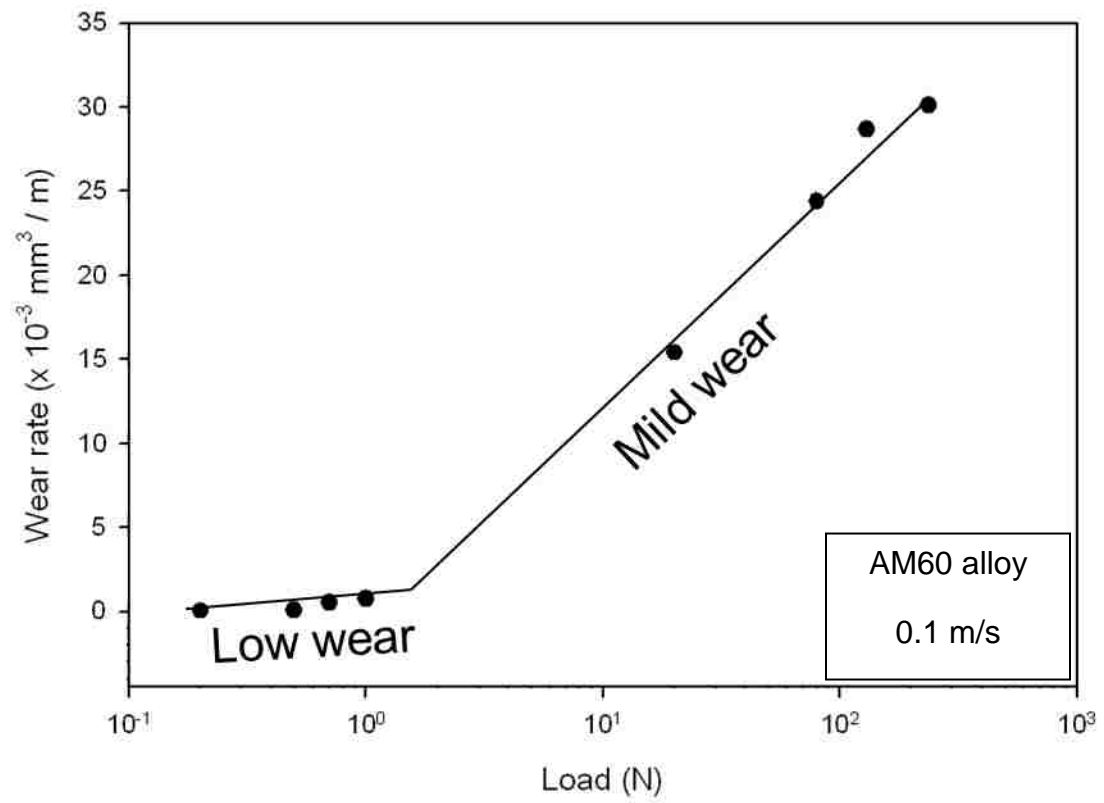
Figure 4.14. Wear rate vs load curve for AM60 alloy at 0.1 m/s.
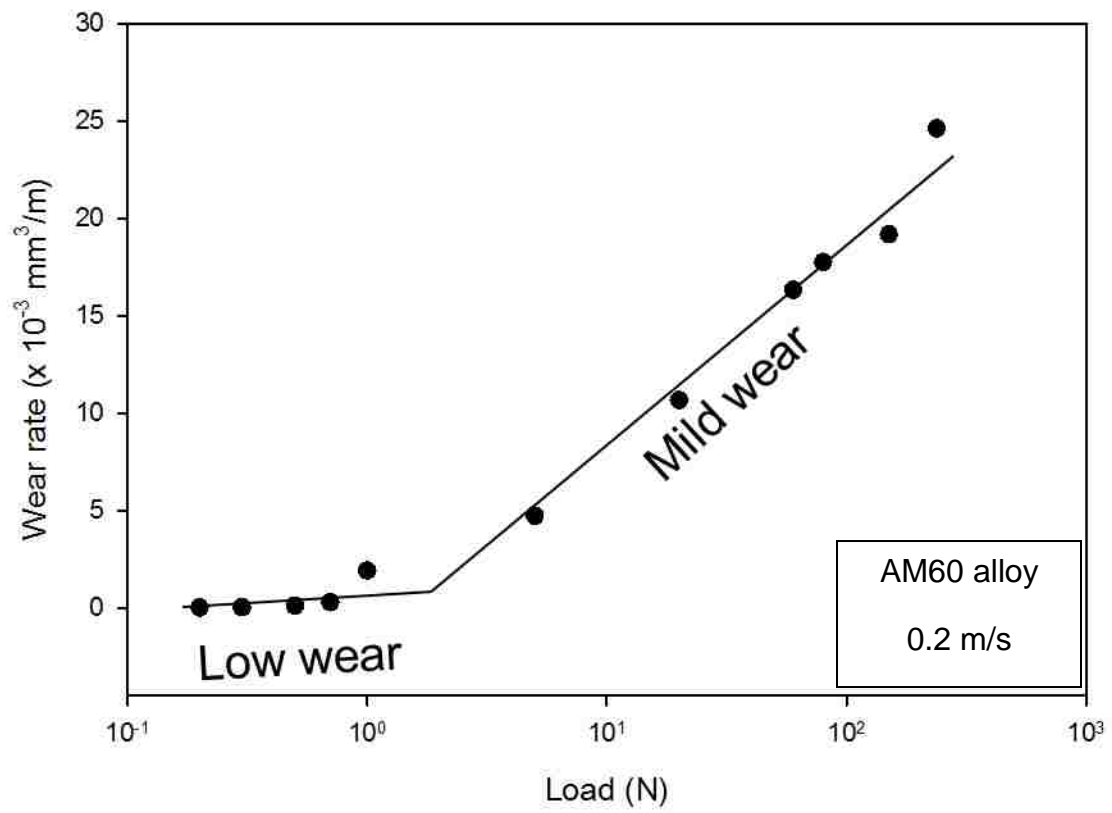
Figure 4.15. Wear rate vs load curve for AM60 alloy at 0.2 m/s.
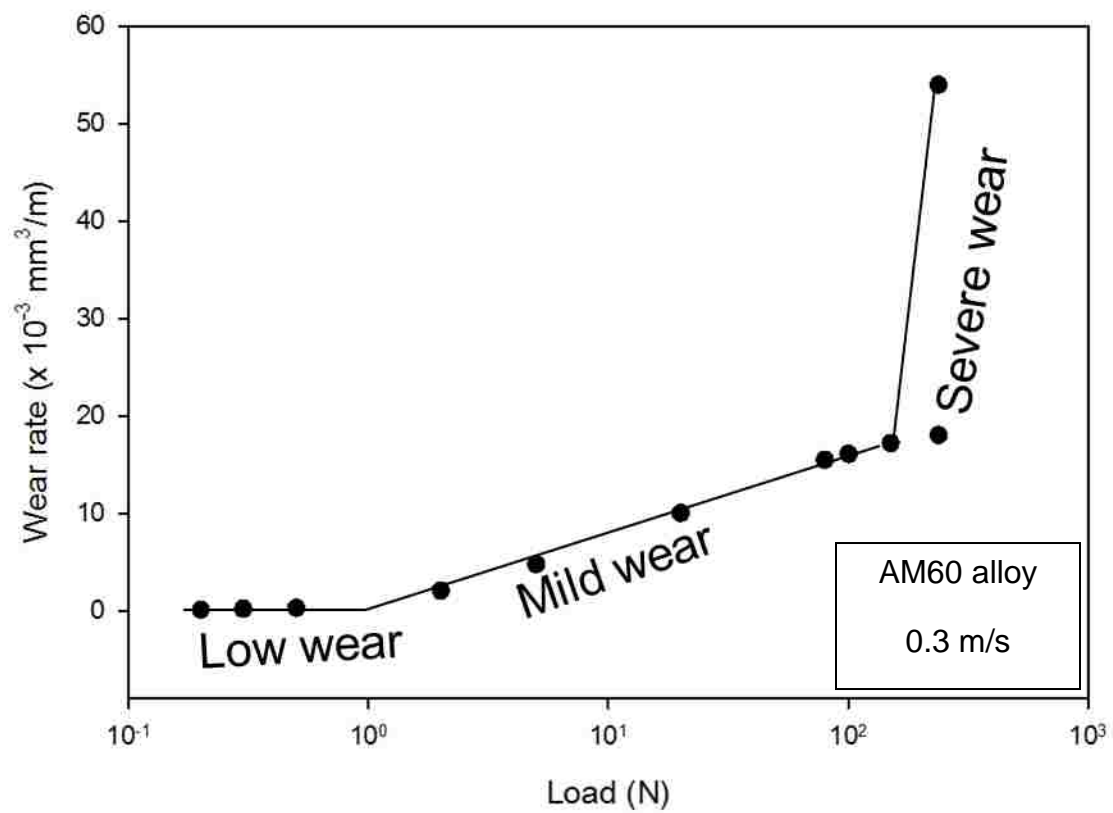
Figure 4.16. Wear rate vs load curve for AM60 alloy at 0.3 m/s.
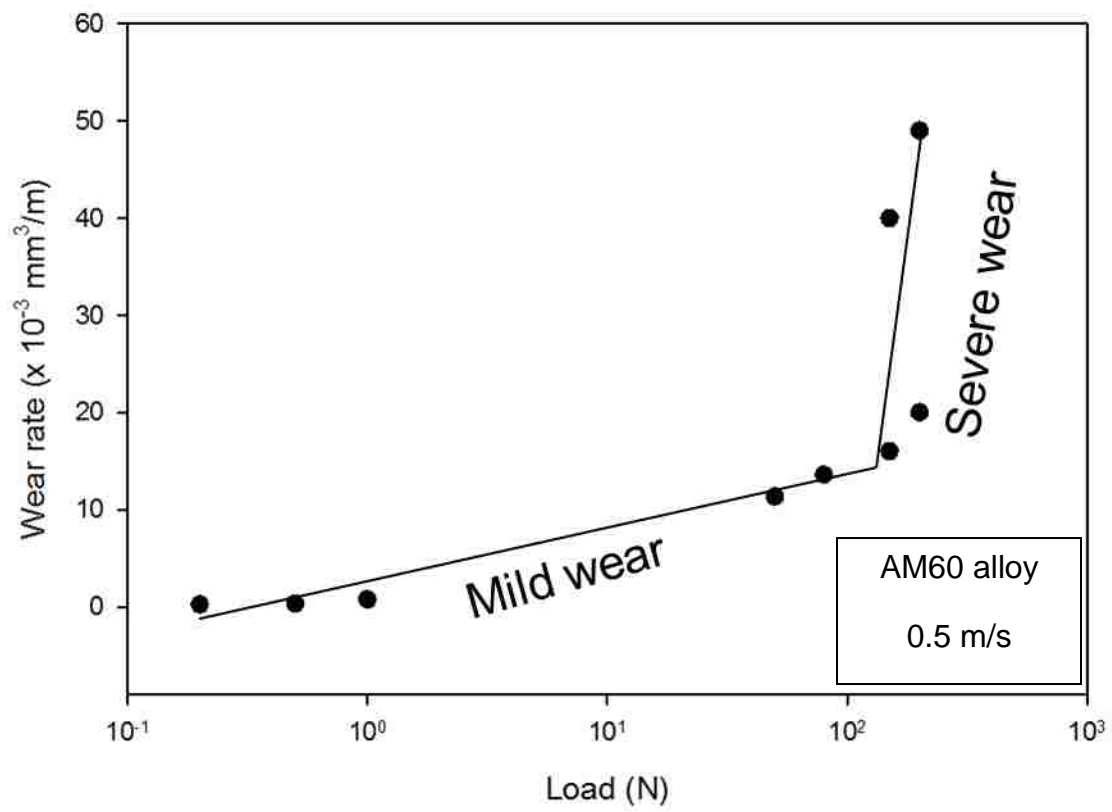
Figure 4.17. Wear rate vs load curve for AM60 alloy at 0.5 m/s.
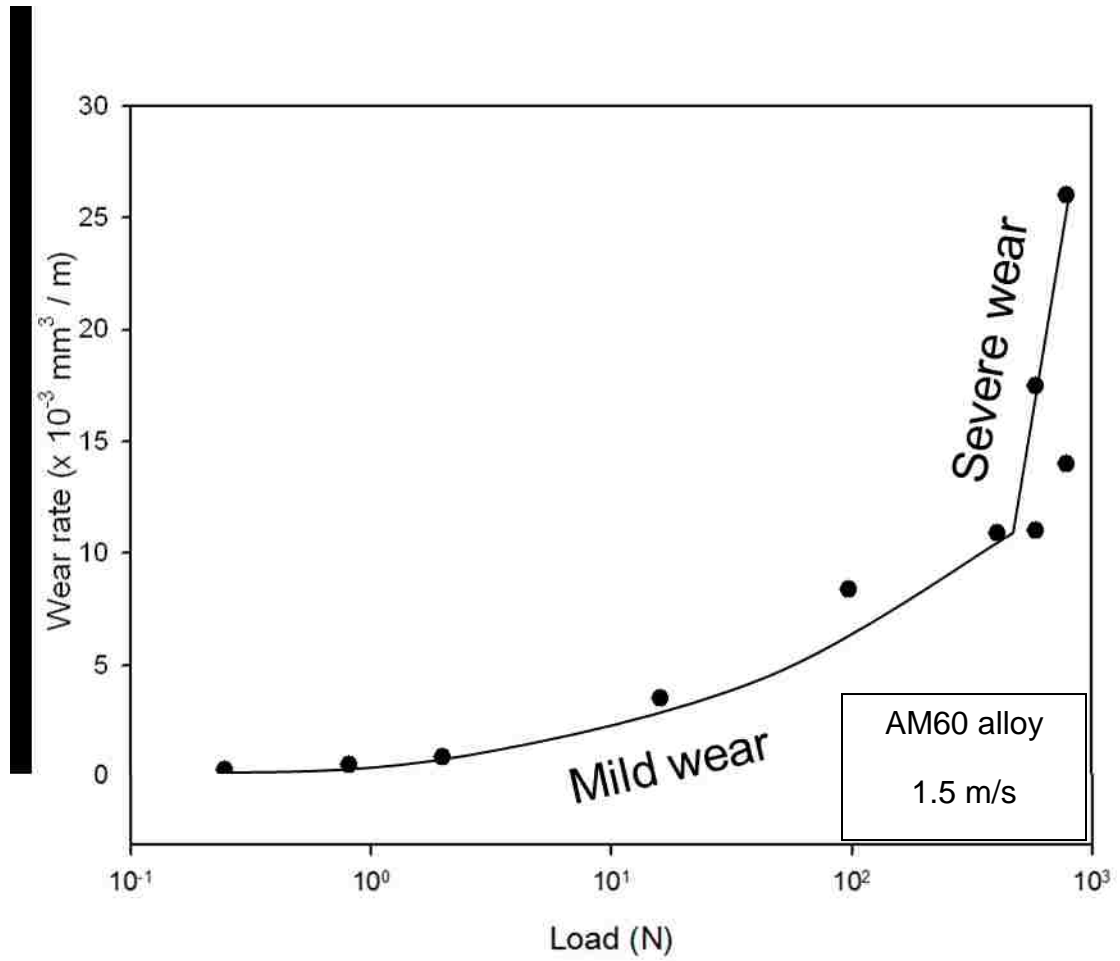
Figure 4.18.Wear rate vs load curve for AM60 alloy at 1.5 m/s.
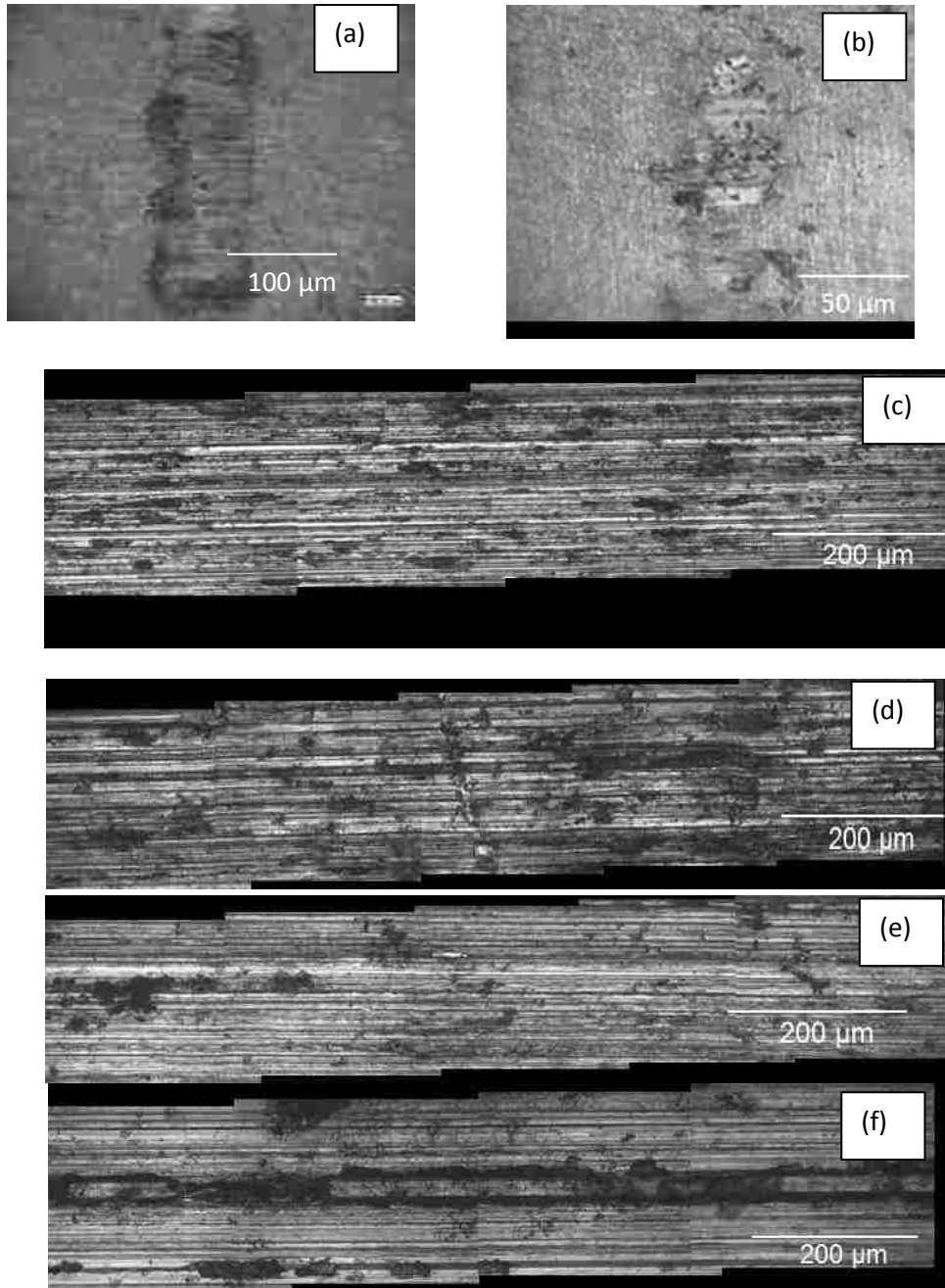
Figure 4.19. Optical micrograph of the worn surface of AM60 alloy at 0.1 m/s at (a) 0.2 N, (b) 0.5 N, (c) 1.0 N, (d) 20.0 N, (e) 80.0 N and (f) 237.8 N.
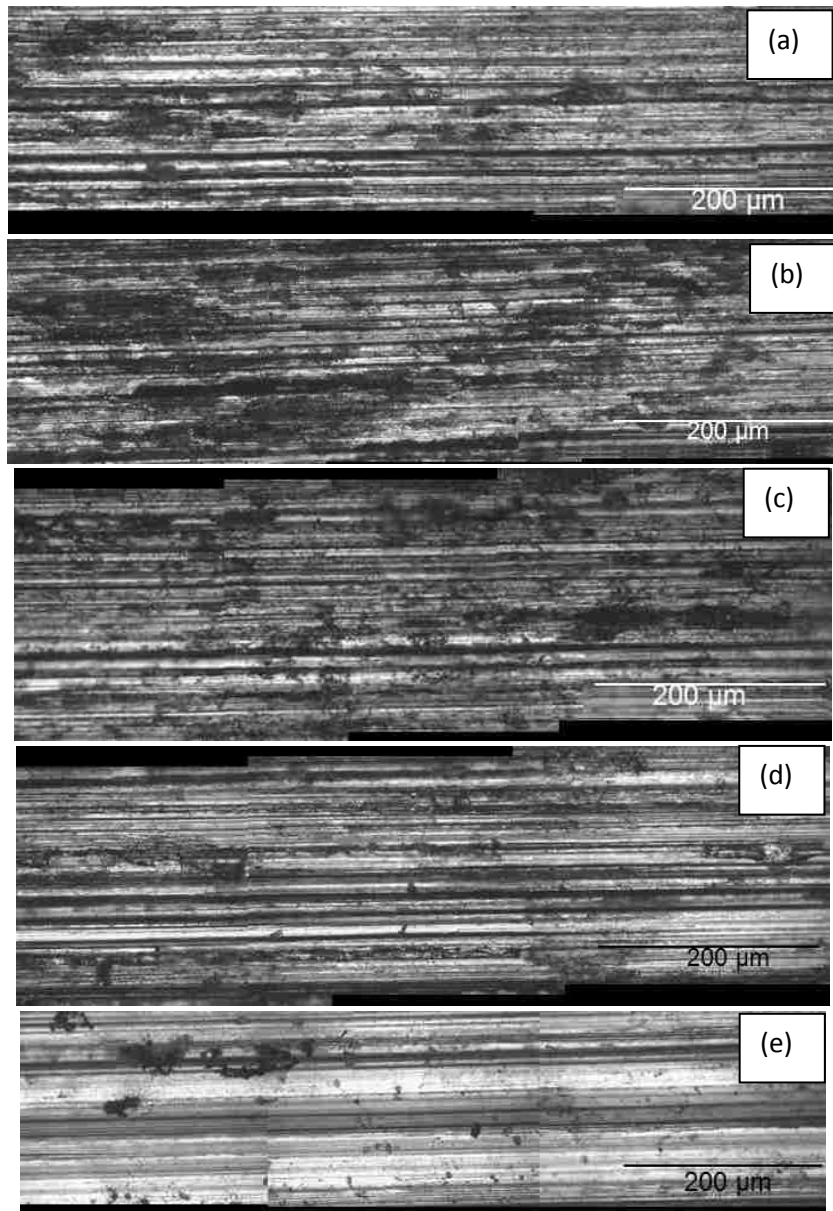
Figure 4.20.Optical micrograph of the worn surface of AM60 alloy at 1.5 m/s at (a) 0.2 N, (b) 0.5 N, (c) 1.0 N, (d) 20.0 N, and (e) 100.0 N.
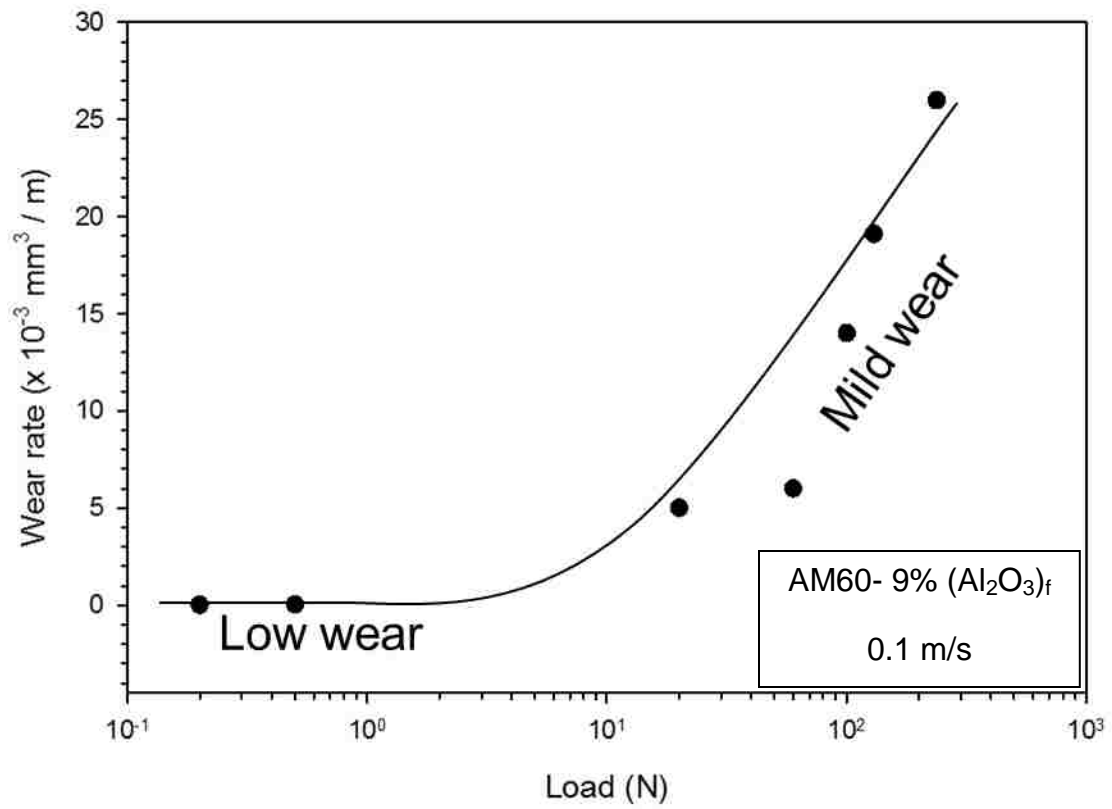
Figure 4.21.Wear rate vs load curve for AM60-9% $(Al_2O_3)_f$ composite at 0.1 m/s.
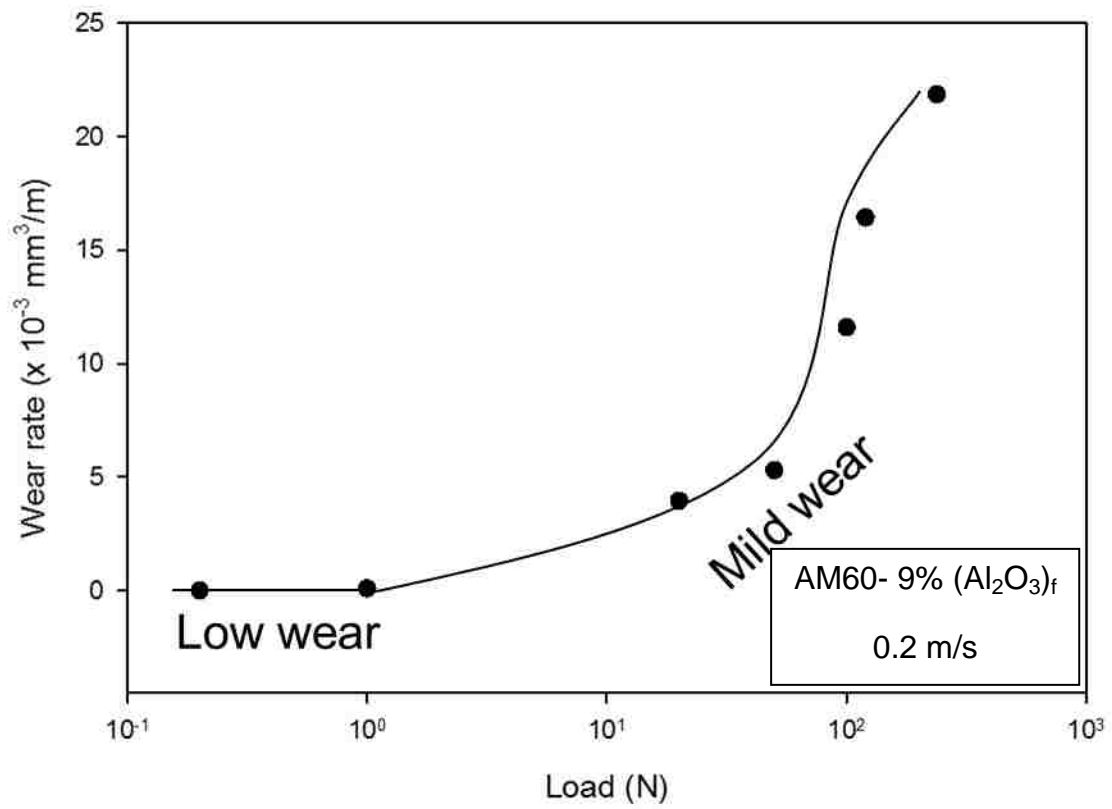
Figure 4.22.Wear rate vs load curve for AM60-9% $(Al_2O_3)_f$ composite at 0.2 m/s.
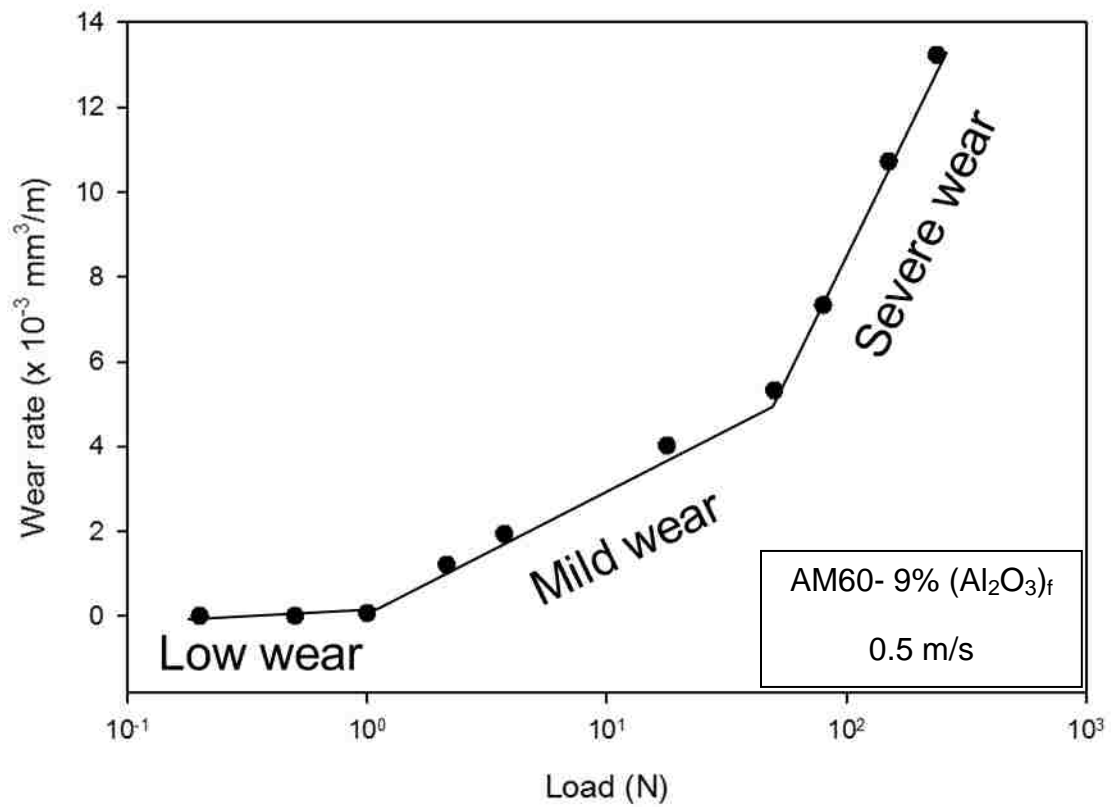
Figure 4.23.Wear rate vs load curve for AM60-9% $(Al_2O_3)_f$ composite at 0.5 m/s.
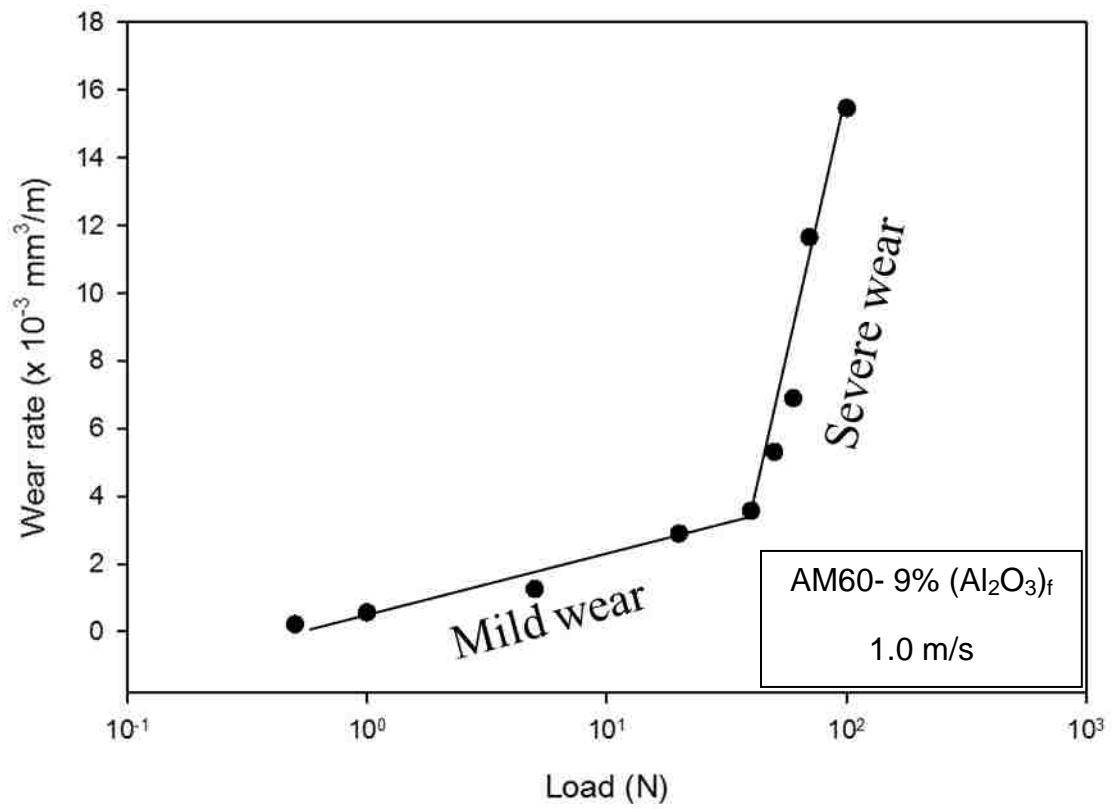
Figure 4.24.Wear rate vs load curve for AM60-9% $(Al_2O_3)_f$ composite at 1.0 m/s.
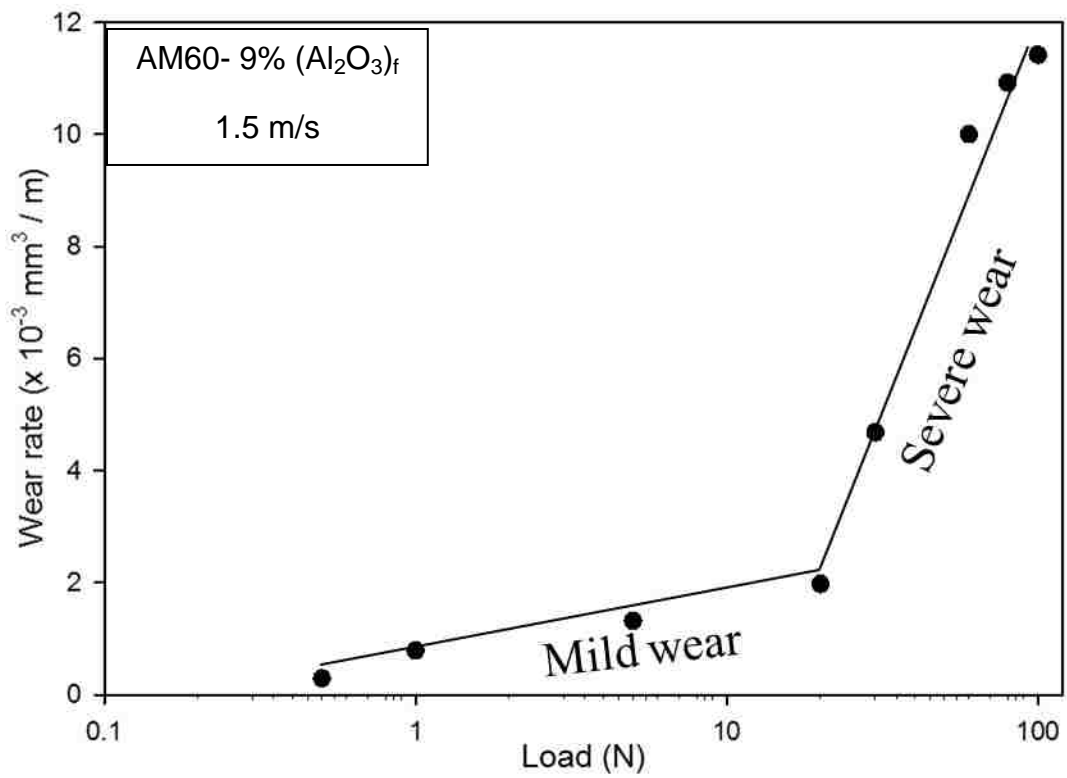
Figure 4.25.Wear rate vs load curve for AM60-9% (Al$_2$O$_3$)$_f$ composite at 1.5 m/s.
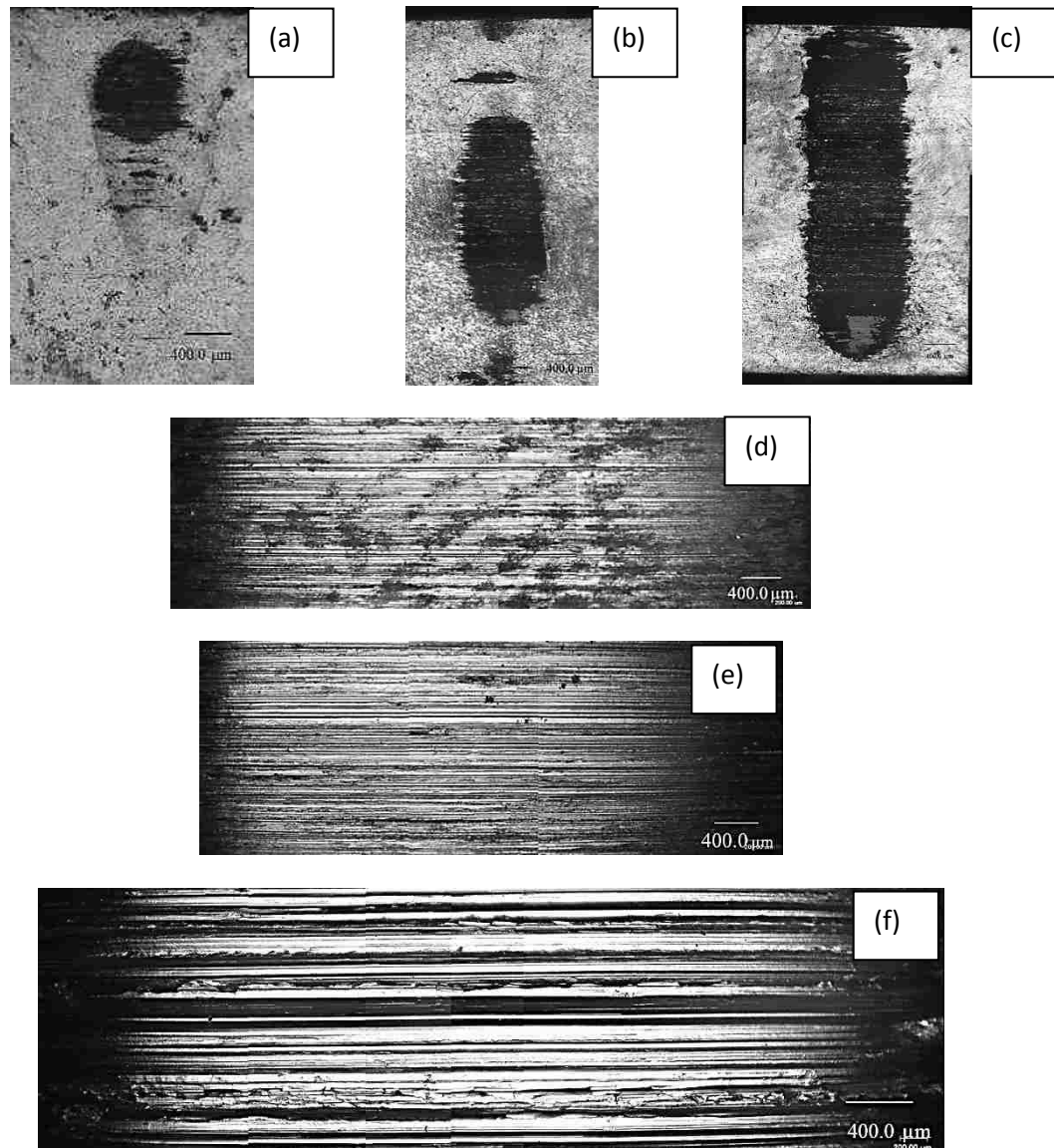
Figure 4.26.Optical micrograph of the worn surface of AM60-9% $(Al_2O_3)_f$ composite at 0.5 m/s at (a) 0.2 N, (b) 0.5 N, (c) 1.0 N, (d) 50.0 N, (e) 80.0 N and (f) 150.0 N.
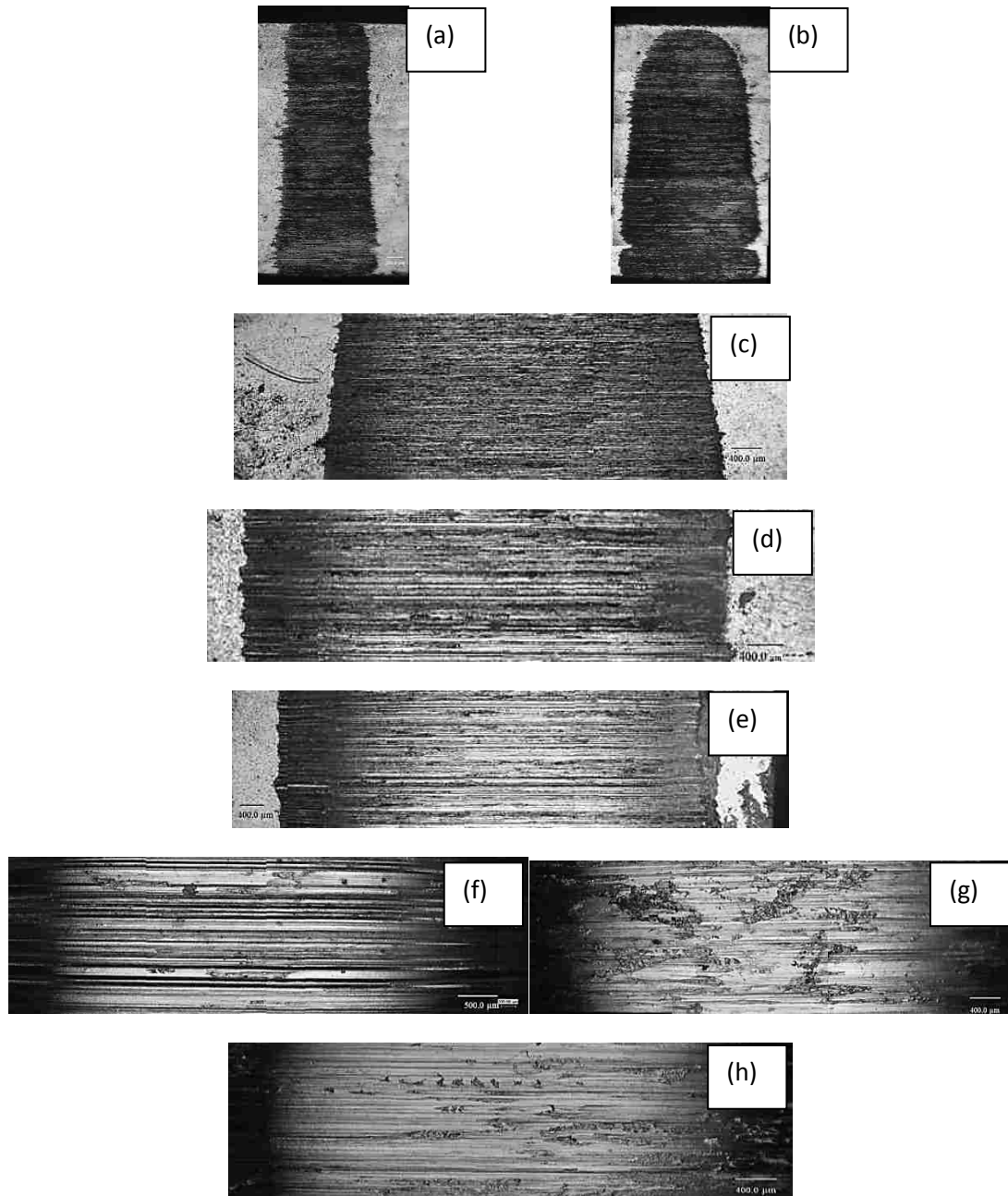
Figure 4.27. Optical micrograph of the worn surface of AM60-9% $(Al_2O_3)_f$ composite at 1.5 m/s at (a) 0.5 N, (b) 5.0 N, (c) 20.0 N, (d) 30.0 N, (e) 60.0 N, (f) 80.0 N (g) 100.0 N and (h) 120.0 N.

4.3. Wear regimes and corresponding wear mechanisms

From the results included in the previous sections, it can be concluded that four prominent wear regimes exist in the tested load and speed range for Mg alloy AM60 and AM60-9% $(Al_2O_3)_f$ composite. These are (i) low wear, (ii) mild wear (iii) transient wear and (iv) severe wear. This section covers a description of the wear mechanisms that control the wear rates within these wear regimes.

4.3.1. Low wear regime

The previous sections lack discretion between low and mild wear regime. Like mild wear regime, low wear regime also shows steady state wear rates wear rates that are two orders less than that in the mild wear regime. AM60 alloy exhibit low wear regime for loads up to 0.5 N, at lowest velocity (0.1 m/s) and 0.3 m/s for the lowest load. The maximum wear rate observed corresponding to a mild wear regime is 1 x 10^{-5} mm^3/m.

SEM micrograph for the wear track on AM60 alloy obtained after sliding at 0.2 N and 0.1 m/s (Fig. 4.28) shows evidence of oxidation of Al and Fe transferred from the counterface on the wear track. The oxidized Al and Fe form a tribolayer that prevents further damage to the Mg matrix.On the other hand , SEM micrograph for the wear track on AM60-9% $(Al_2O_3)_f$ composite 0.2 N and 0.1 m/s (Fig. 4.28) shows the removal of Al_2O_3fibres. The tribolayer comprised of oxidized Fe that was transferred from the counterface to the wear track. The amount of Fe detected on the wear track, however is greater in AM60-9% $(Al_2O_3)_f$ composite as compared to that in AM60 alloy. This can be attributed to an increased abrasion of the counterface due to the presence of hard Al_2O_3fibres in the composite. Since the wear tracks of both AM60 alloy andAM60-9%

(Al_2O_3)$_f$ composite were covered with oxides, oxidation wear can be referred to as the operating mechanism in the low wear regime.

4.3.2. Mild wear regime

It has been established in 4.2 that the wear rates in the mild wear regime are in the steady state condition. This is proved by the gradual increase in the wear rates with the increase in the applied load for a given sliding speed. The EDS map of the worn surface of the AM60 alloy at 237.8 N at 0.1 m/s (Fig. 4.30) shows that the worn surface is covered with oxides. The EDS map of oxygen overlap Fe and Mg which shows that oxides of these elements are formed on the surface. The wear process produced agglomerates of black fine debris, SEM micrograph of which (Fig. 4.31) shows presence of agglomerated oxides of Fe and Mg in the wear debris similar to that found on the worn surface. The average size of these agglomerates was measured to be around 100 μm.

Under similar sliding condition i.e. 237.8 N and 0.1 m/s, the SEM micrograph and the corresponding EDS maps of the worn surface of the AM60-9% (Al_2O_3)$_f$ also show evidence of oxidation of Mg and Fe on the worn surfaces. Al map shows the distribution of Al_2O_3on the worn surface. The debris produced by wear process under same sliding conditions showed agglomerated Mg and flakes of Fe covered with O which suggested that Al_2O_3fibre caused abrasion of Fe flakes which later oxidized along with the oxidation of Mg (Fig. 4.32). The average size of Fe flakes was found to be approx. 80 μm.

Considering the formation of oxidized debris and the worn surface covered with oxides of Mg and Fe, "oxidational wear" can be referred as the main wear mechanism operating under mild wear regime. The flakes of Fe found in wear debris the case of AM60-9%

$(Al_2O_3)_f$ composite can we attributed to the presence of Al_2O_3fibres in the composite which caused abrasion of the counterface due their hardness being higher than that of AISI 52100 steel. Had it not been Al_2O_3fibres, the wear debris would still be consisiting of agglomerate of oxidized Mg and Fe.

4.3.3. Severe wear regime

It would be much convenient to discuss severe wear before transient wear to explain the concept of transient wear clearly. In the severe wear regime, wear rates are not in the steady state condition. Severe surface damage caused accelerated wear which caused an increase in the wear rate. At applied loads above 100.0 N at the highest test speed i.e. 1.5 m/s , a thin layer material exited from the contact area in the sliding direction. The bulk material was extruded out not only in sliding direction but also on the two sides perpendicular to the sliding direction (Fig. 4.33 (a)). The formation of thin layer which caused this extrusion can be attributed to the severe frictional heating due to wear. This will be discussed in detail in the later sections. This was a continuous process in which more layers of molten and quasi-molten material kept flowing out, pushing and slipping over the previous layers, resulting in the formation of a multilayered structure (4.33 (a,b)). The multilayered structure curved up and then broke away to produce chunks of metallic debris.

The worn surfaces of the AM60 alloy (Fig. 4.34) and AM60-9% $(Al_2O_3)_f$(Fig. 4.35)composite also showed the flow of the top molten layer. Elemental mapping of the worn surfaces show the minimal presence of Fe and no prominent oxidation on the worn surface. This could mean that no damage was caused to the counterface because of the thermal softening but the elemental mapping of the debris produced by tests at 100.0 N

and 1.0 m/s for AM60-9% $(Al_2O_3)_f$ composite showed the presence of oxidized Fe in the wear debris suggesting initial wear of the counterface due to Al_2O_3 which was washed away with the molten layer (Fig. 4.36).

4.3.4. Transient wear regime

It is obvious that transition from mild wear to severe wear regime is not abrupt. An intermediate regime was suggested to exist between the two regimes. The wear process in this regime consisted of the characteristics of both regimes. To understand this phenomenon, worn surfaces of AM60-9% $(Al_2O_3)_f$ composite tested at 60.0 N 1.5 m/s at different distances can be considered. Figure 4.37 shows the worn surface at 50 m. The surface shows characteristics of oxidational wear under mild wear condition. The surface is covered with oxides of Mg and Fe. This can be compared with the observations made in Figure 4.30 for mild wear regime. The presence of Fe shows the abrasion of the counterface which has been proved previously to occur in mild wear regime only. At 400 m (Fig. 4.38), the presence of oxygen is only limited to that as a part of Al_2O_3fibres. So no oxidation of the surface during the wear process is evident. Fe content is negligible which is earlier explained as a prominent trait of severe wear. Similar surface features are observed at 2000 m (Fig. 4.39), with no iron content on the worn surface and O present only in the form of Al_2O_3. The wear process showing mild behaviour initially and severe behaviour later indicates that there exists an intermediate regime which can be referred as transient wear regime. The mircrostructural observation show evidence of oxidational and delamination wear as two operating mechanisms in the transient wear. The effect of temperature on the transition from oxidational (mild) wear to delamination (severe) wear will be discussed in detail in Chapter 5.
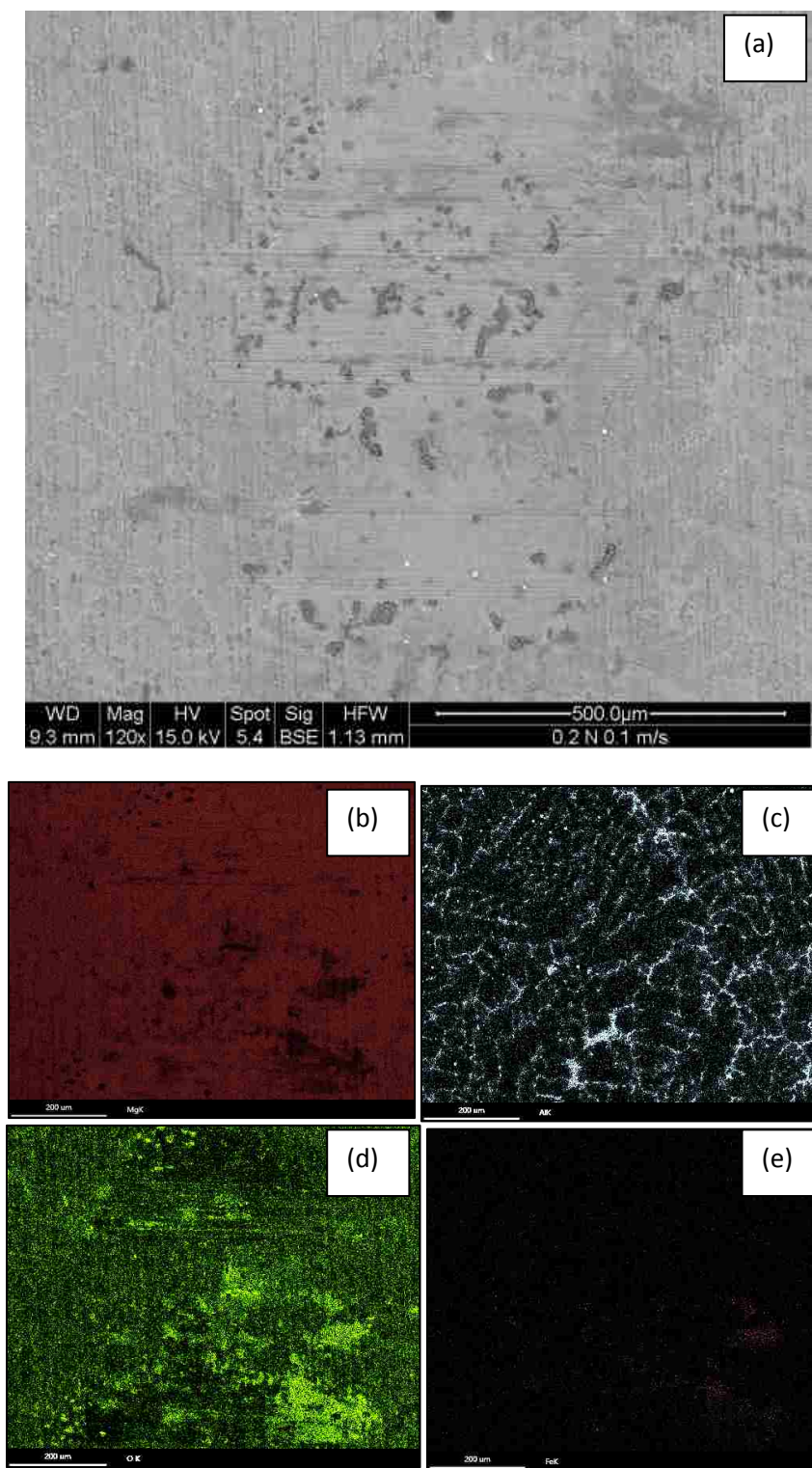
Figure 4.28.(a) SEM micrograph of AM60 alloy worn at 0.2 N 0.1 m/s. EDS maps showing (b) Mg, (c) Al, (d) O and (e) Fe
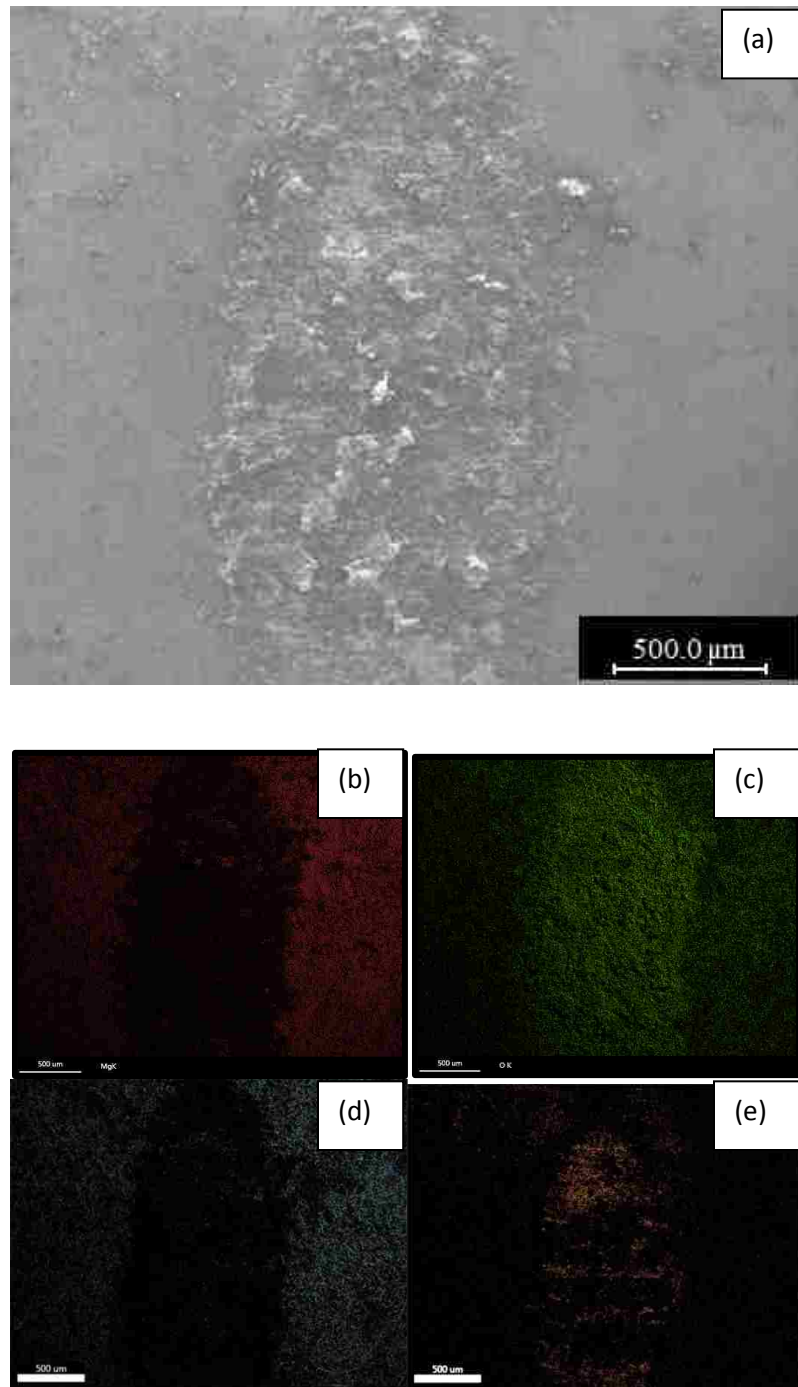
Figure 4.29.(a) SEM micrograph of AM60-9% $(Al_2O_3)_f$ composites worn at 0.2 N 0.1 m/s. EDS maps showing (a) Mg, (b) Al, (c) O and (d) Fe.
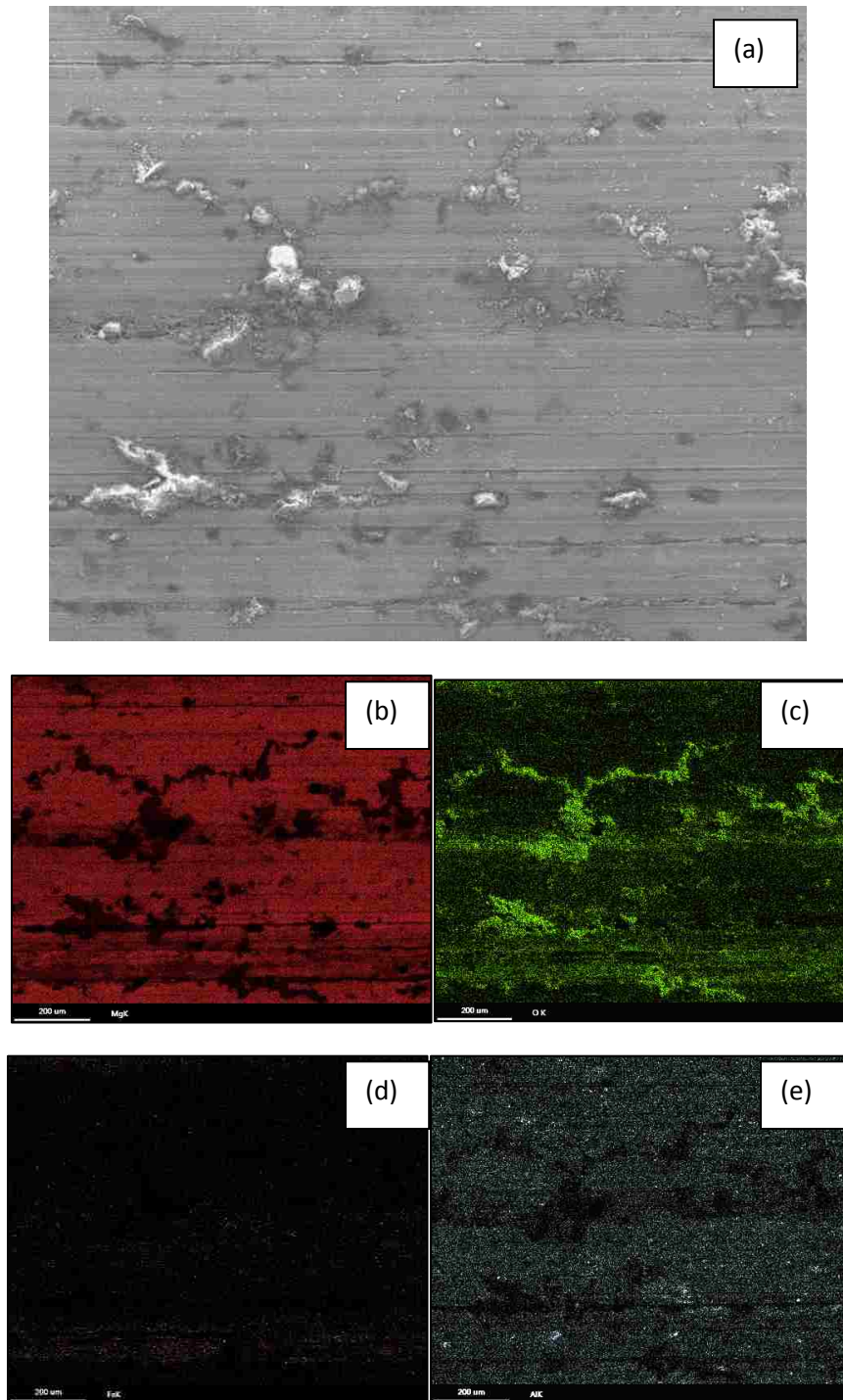
Figure 4.30.(a) SEM micrograph of AM60 alloy worn at 237.8 N 0.1 m/s. EDS maps showing (a) Mg, (b) Al, (c) O and (d) Fe.
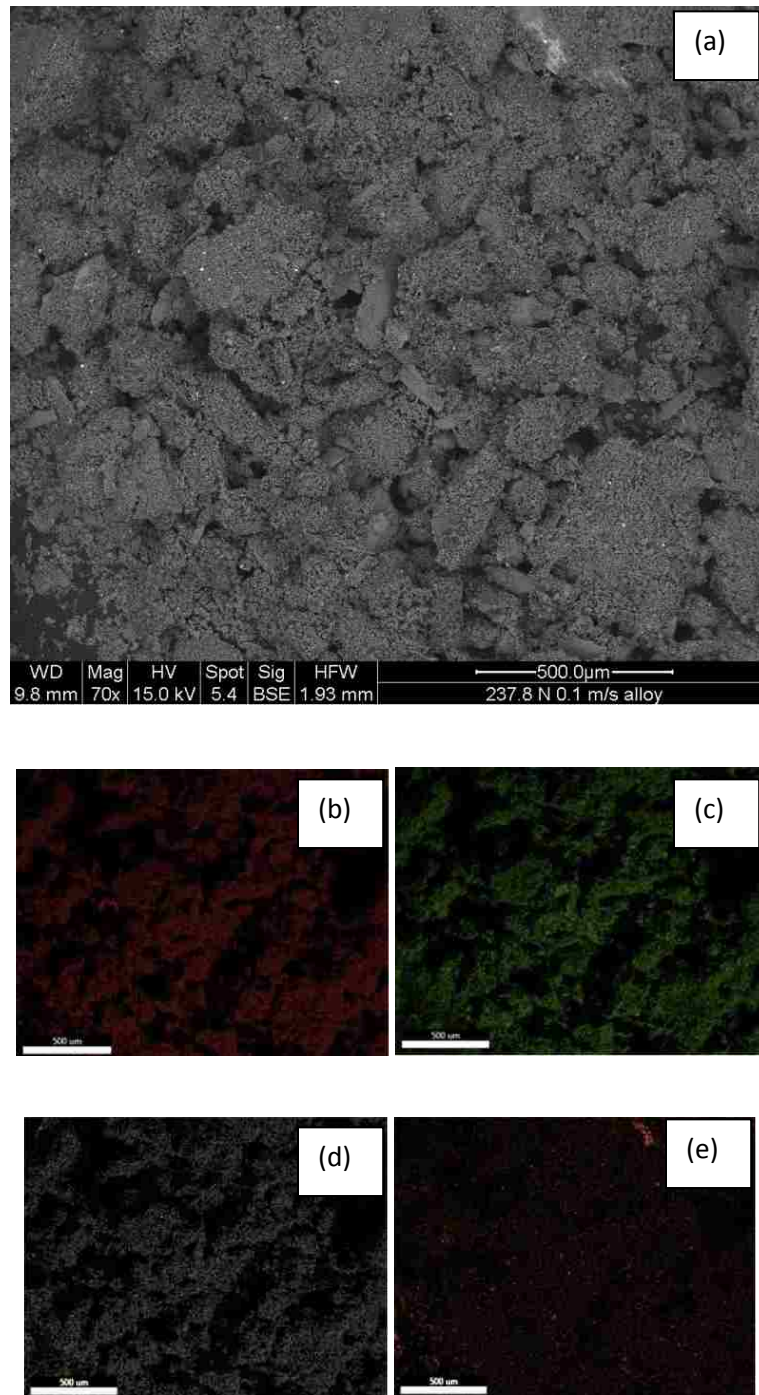
Figure 4.31.(a) SEM micrograph of AM60 alloy debris worn at 237.8 N 0.1 m/s. EDS maps showing (a) Mg, (b) Al, (c) O and (d) Fe.
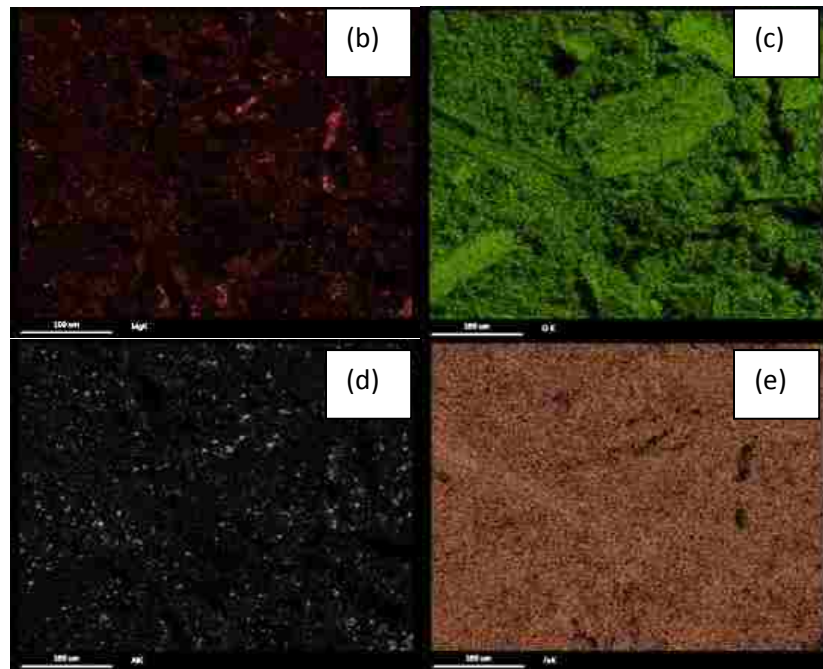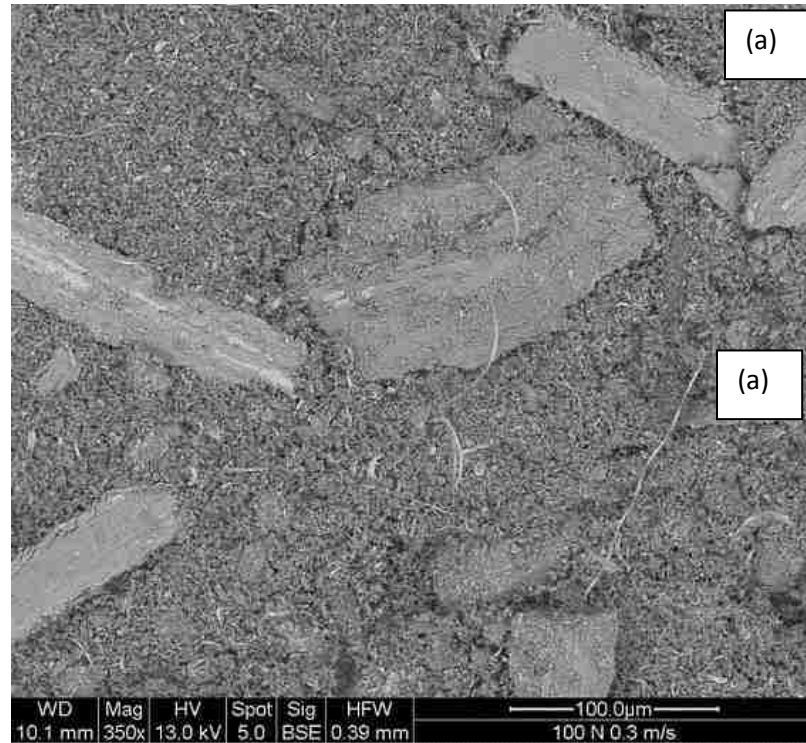
Figure 4.32. (a) SEM micrograph of AM60-9% $(Al_2O_3)_f$ composites debris worn at 237.8 N 0.1 m/s. EDS maps showing (a) Mg, (b) Al, (c) O and (d) Fe.
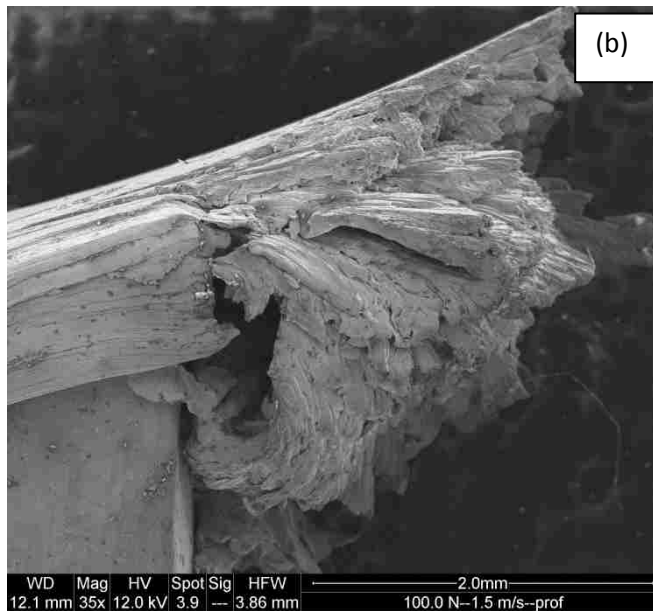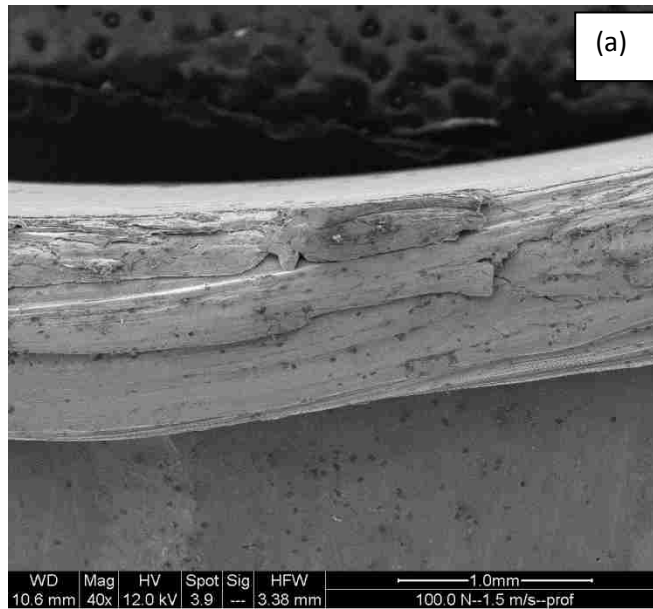
Figure 4.33 (a) Extruded layer from the surface of AM60 alloy perpendicular to the sliding direction. (b) Extruded layer from the surface of AM60 alloy in the sliding direction.
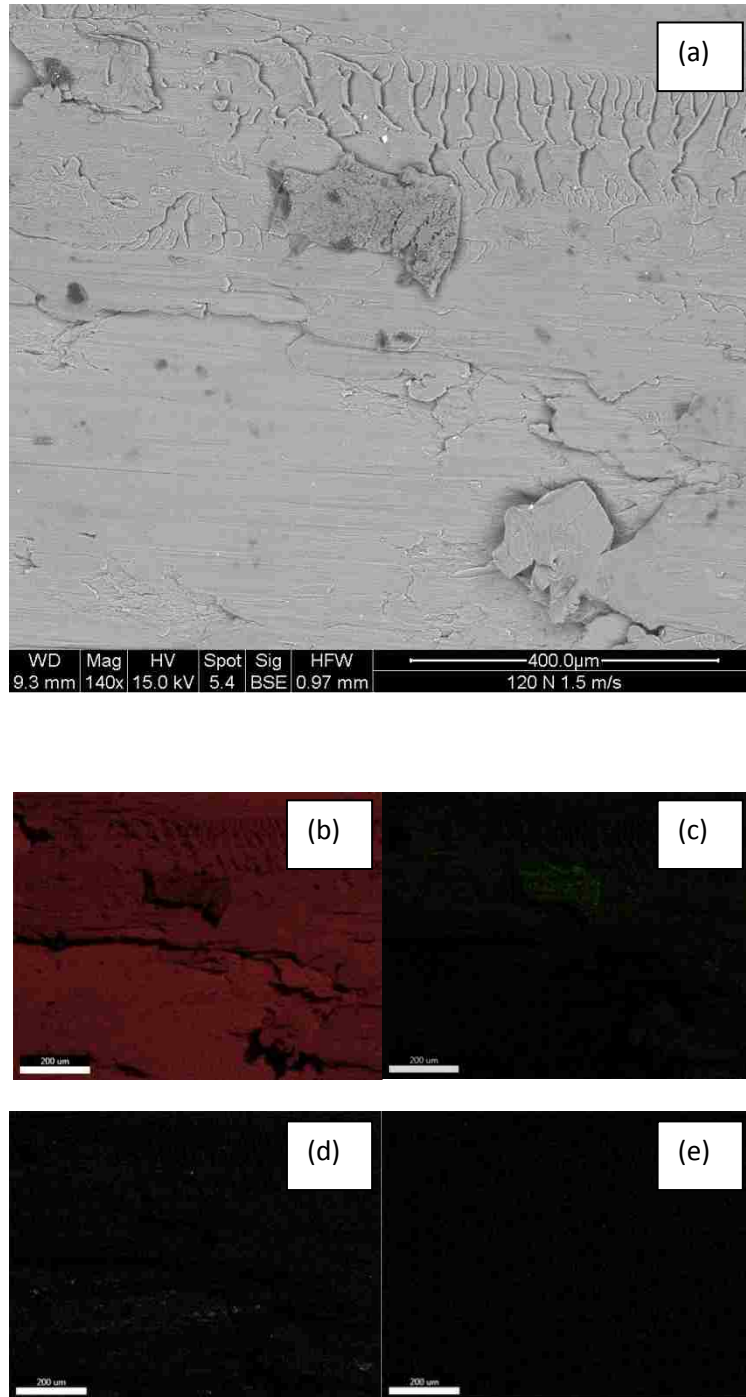
Figure 4.34.(a) SEM micrograph of AM60 alloy worn at 120 N 1.5 m/s. EDS maps showing (a) Mg, (b) Al, (c) O and (d) Fe.
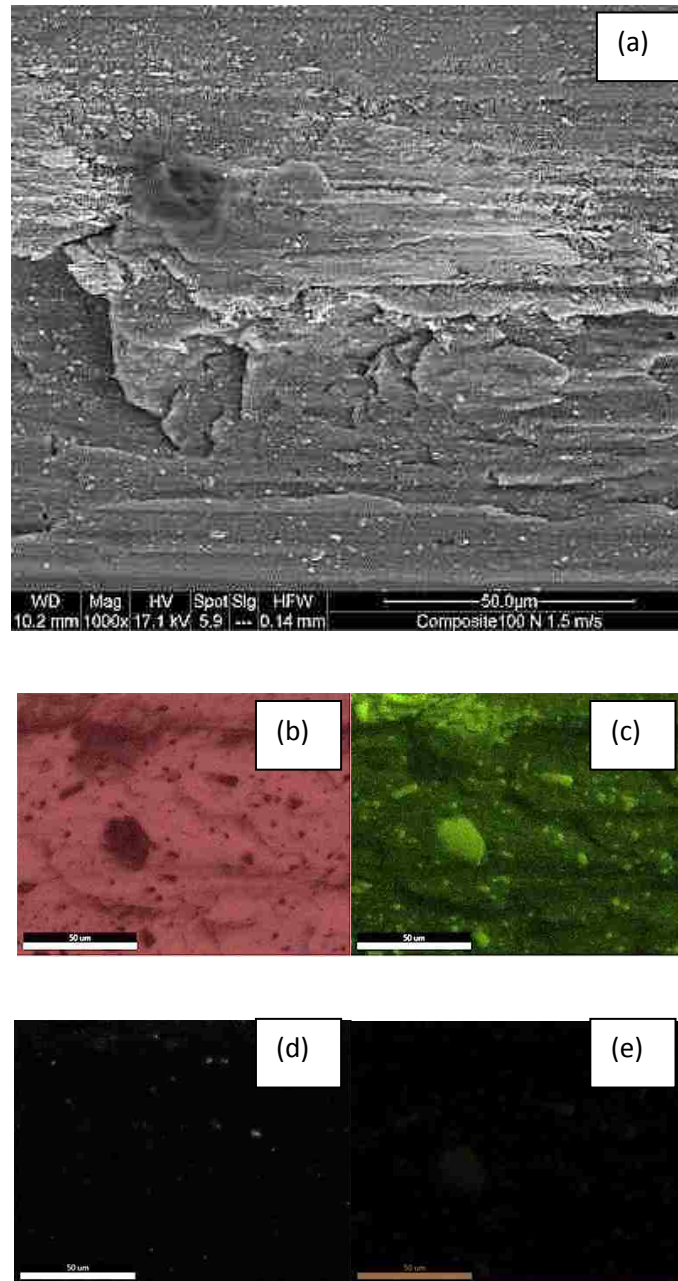
Figure 4.35.(a) SEM micrograph of AM60-9% (Al$_2$O$_3$)$_f$ composite worn at 120 N 1.5 m/s. EDS maps showing (a) Mg, (b) Al, (c) O and (d) Fe.
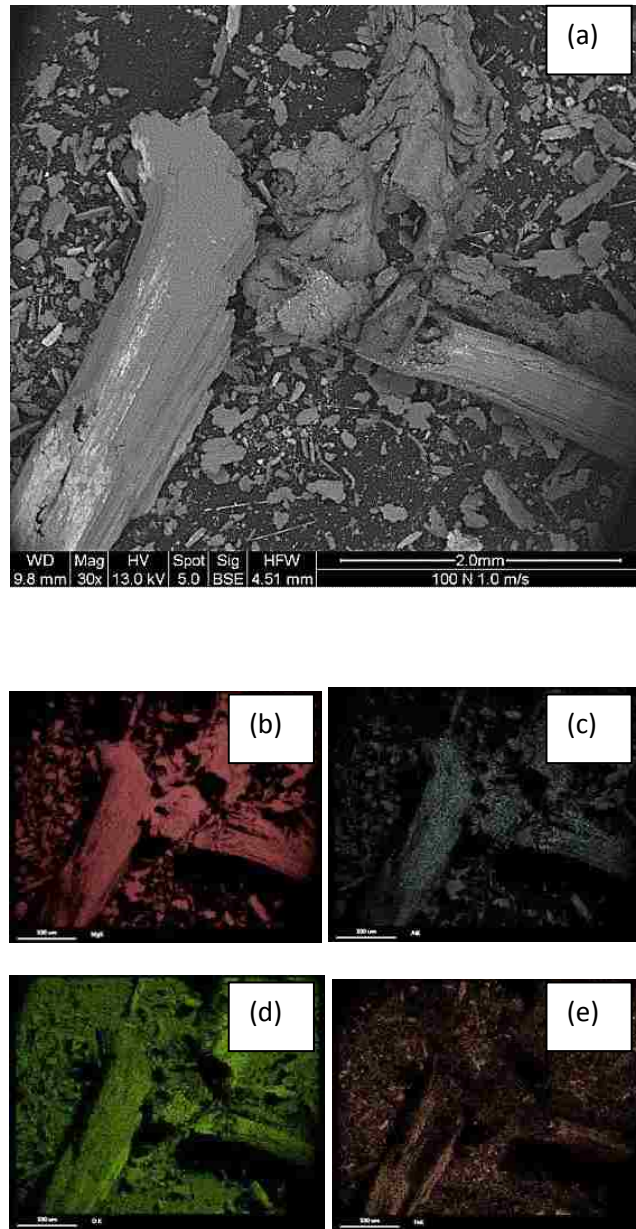
Figure 4.36.(a) SEM micrograph of AM60-9% $(Al_2O_3)_f$ composite debris worn at 100 N 1.0 m/s. EDS maps showing (a) Mg, (b) Al, (c) O and (d) Fe.
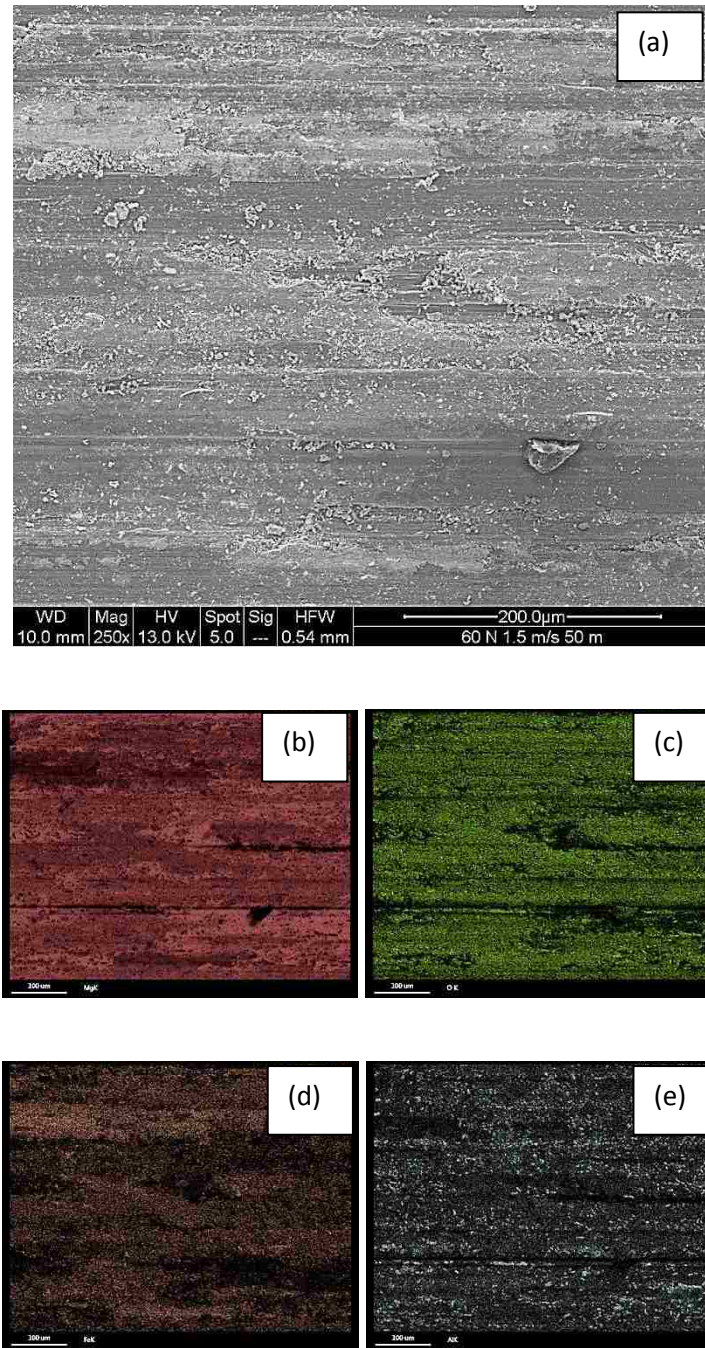
Figure 4.37. (a) SEM micrograph of AM60-9% $(Al_2O_3)_f$ composite worn at 60.0 N 1.5 m/s for a distance of 50 m. EDS maps showing (a) Mg, (b) Al, (c) O and (d) Fe.
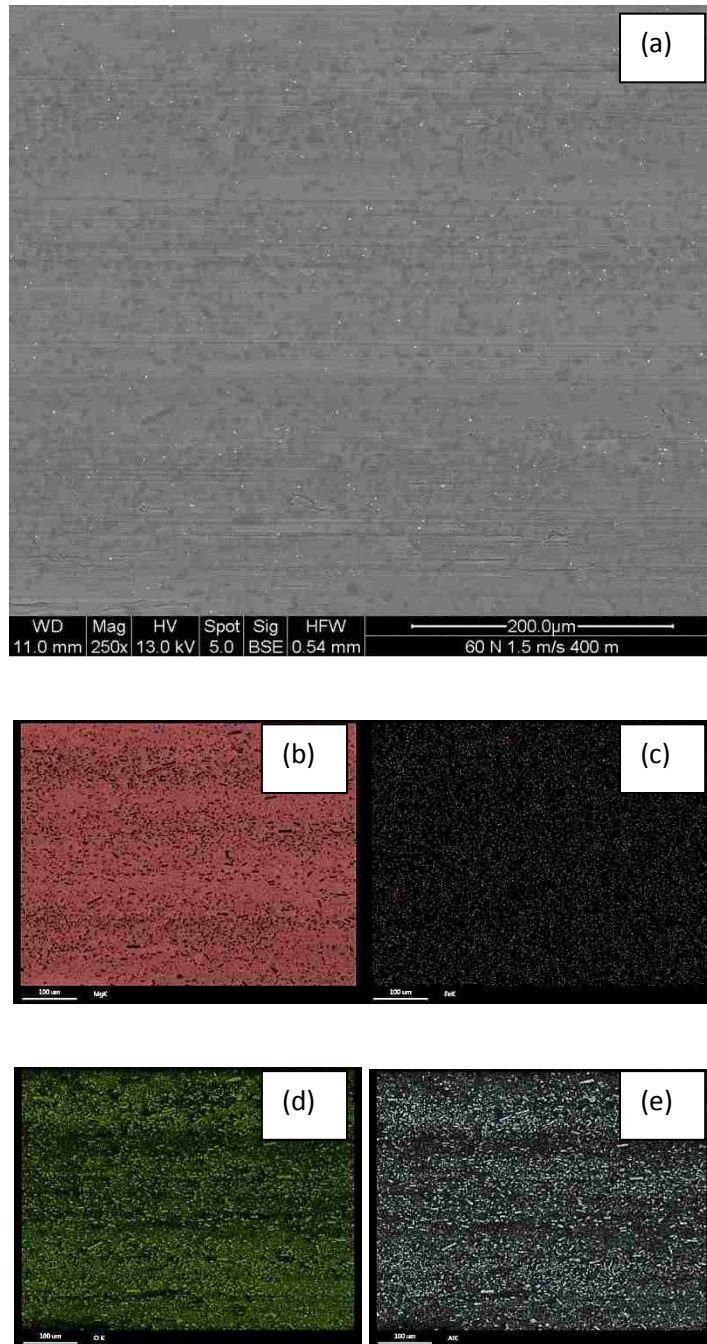
Figure 4.38.(a) SEM micrograph of AM60-9% $(Al_2O_3)_f$ composite worn at 60.0 N 1.5 m/s for a distance of 400 m. EDS maps showing (a) Mg, (b) Al, (c) O and (d) Fe.
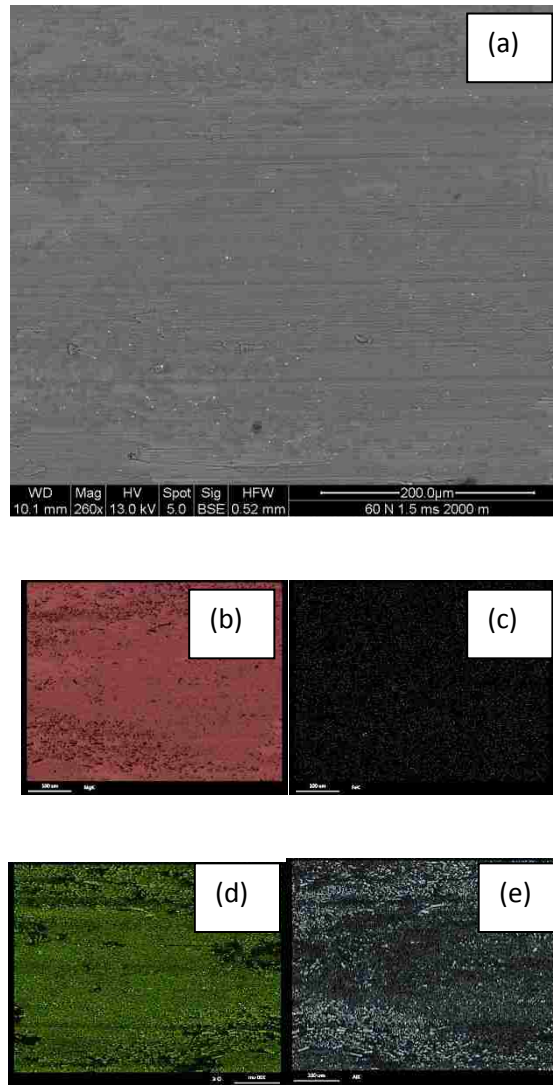
Figure 4.39.(a) SEM micrograph of AM60-9% $(Al_2O_3)_f$ composite worn at 60.0 N 1.5 m/s for a distance of 2000 m. EDS maps showing (a) Mg, (b) Al, (c) O and (d) Fe.

4.4. The wear map for AM60 alloy and AM60-9% $(Al_2O_3)_f$ composite

The results presented in sections 4.2 and 4.3 explain the four wear regimes, low, mild, transient and severe wear regimes, that exist in the tested load and speed range for Mg alloy AM60 and AM60-9% $(Al_2O_3)_f$ composite. The wear process in the low and mild wear regimes is prominently controlled by oxidation wear. In the transient wear regime, two sub-regimes exist, namely oxidational and plastic deformation induced wear. The severe wear is prominently controlled by melt wear and large scale plastic deformation and extrusion. Figure 4.40 and 4.41 show a wear maps for AM60 and AM60-9% $(Al_2O_3)_f$ which show different wear regimes as a function of applied load and speed on logarithmic axes. The construction of these maps is based entirely on the experimental observations. Each point in the map represents a combination of applied load and speed. Dry sliding wear tests were conducted using Mg alloy AM60 and AM60-9% $(Al_2O_3)_f$ composite at all the combination indicated in these maps. Steady state wear rates are indicated by (●), while the load-speed combination showing change in slopes are indicated by (○) which indicate the transition from mild to severe wear in the transient wear regime. The boundary lines are drawn accordingly to separate the wear regimes. Wear rate maps constructed for AM60 and AM60-9% $(Al_2O_3)_f$ by plotting the measured wear rates with the load-speed axes are shown in Fig. 4.42 and 4.43.

Comparison of the wear maps for AM60 and AM60-9% $(Al_2O_3)_f$ shows that the mild wear regime for AM60-9% $(Al_2O_3)_f$ is larger than that of AM60 at the expense of transient wear regime. In AM60 alloy, the transient wear is first at a velocity of 0.3 m/s at 80.0 N while mild wear prevails at all applied load for AM60-9% $(Al_2O_3)_f$ composite. Similarly, at a maximum test speed of 1.5 m/s, transient wear is first observed at 5.0 N in

AM60 alloy while 50.0 N marks the initiation of transient wear in AM60-9% $(Al_2O_3)_f$ composite. This suggests that the transition from mild to severe is delayed due to the introduction of reinforcement fibres. Comparison of wear rate maps show that reinforcing AM60 alloy with Al_2O_3 fibres reduced the wear rates as compared to that for unreinforced alloy. The maximum wear rate for mild wear observed at 237.8 N and 0.1 m/s is 25.98 x 10^{-3} mm^3/m for AM60-9% $(Al_2O_3)_f$ which is lower than 33.08 x 10^{-3} mm^3/m for AM60. Also, the accelerated war rate for 100.0 N and 1.5 m/s of 24.52 x 10^{-3} mm^3/m for AM60-9% $(Al_2O_3)_f$ is lower than 26.00x 10^{-3} mm^3/m for AM60 alloy.
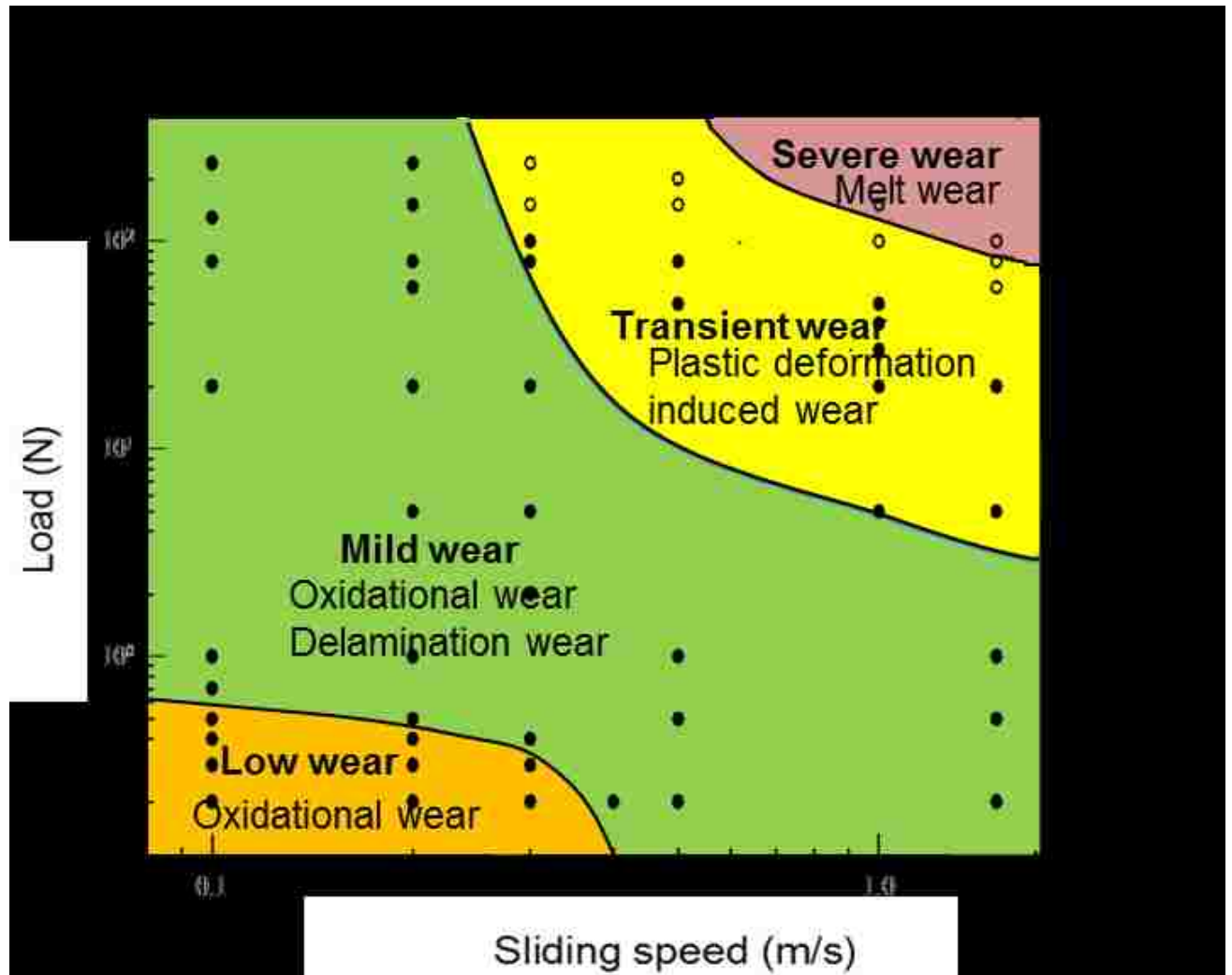
Figure 4.40. Wear map for AM60 alloy
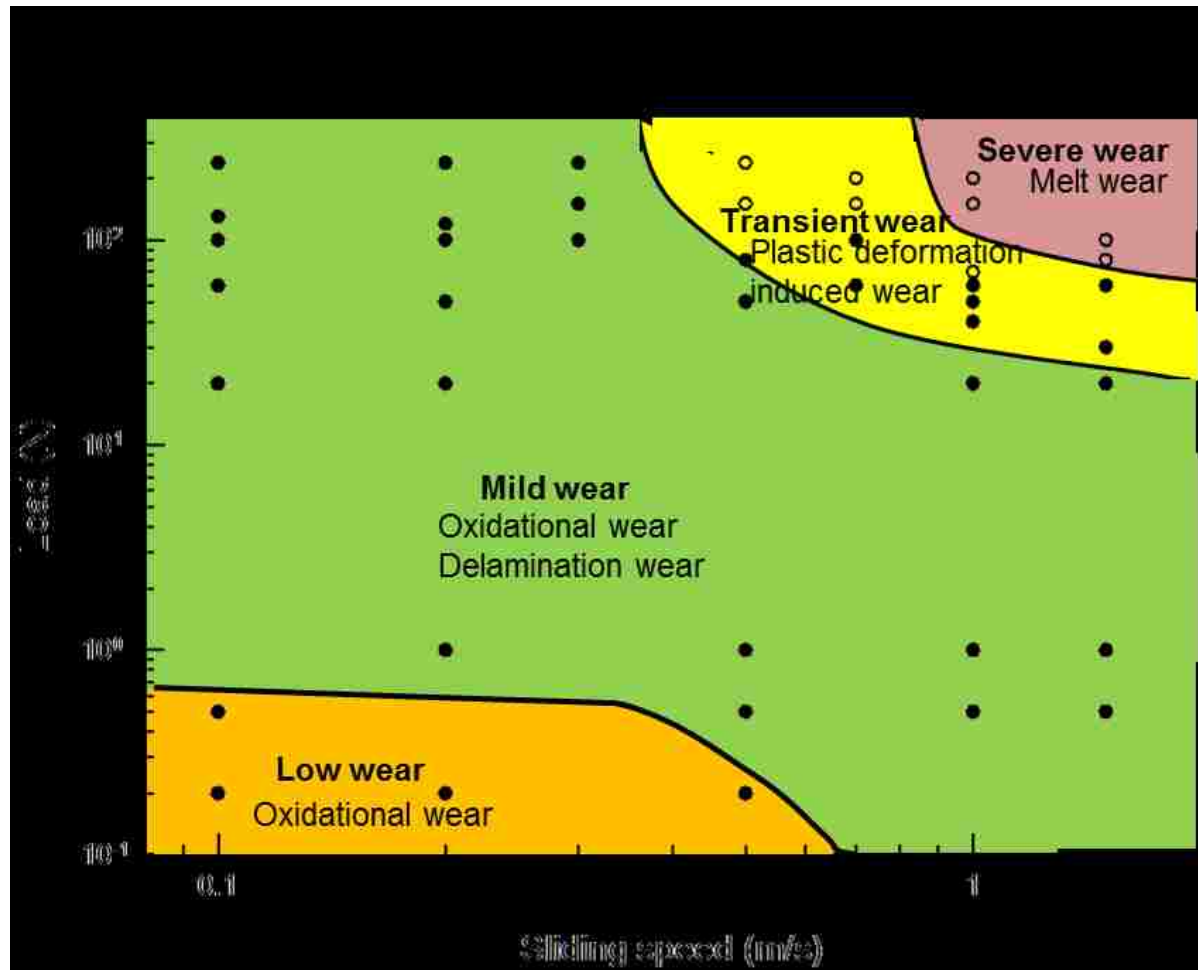
Figure 4.41.Wear map forAM60-9% $(Al_2O_3)_f$ composite.
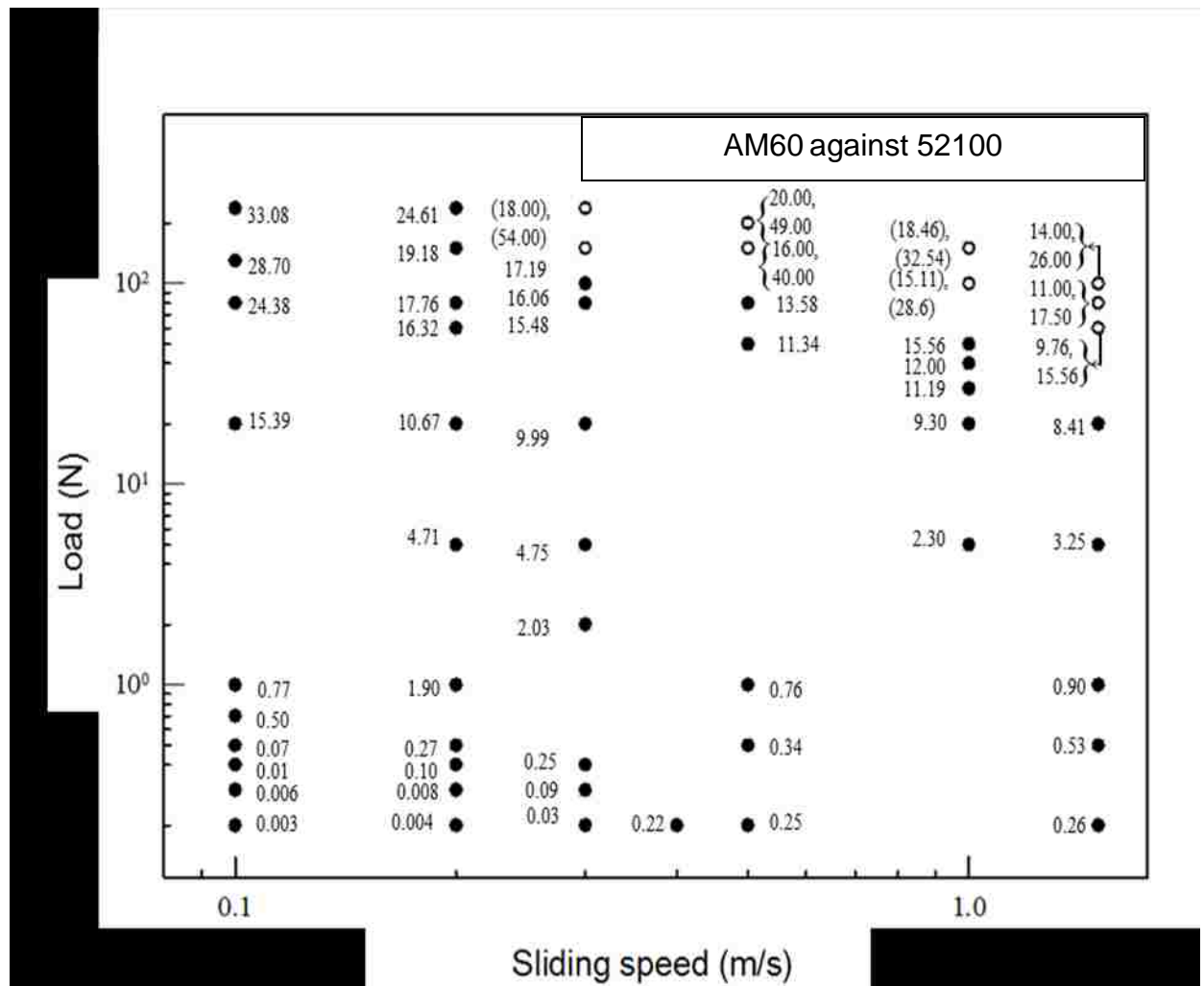
Figure 4.42. Wear rate map for AM60 alloy.
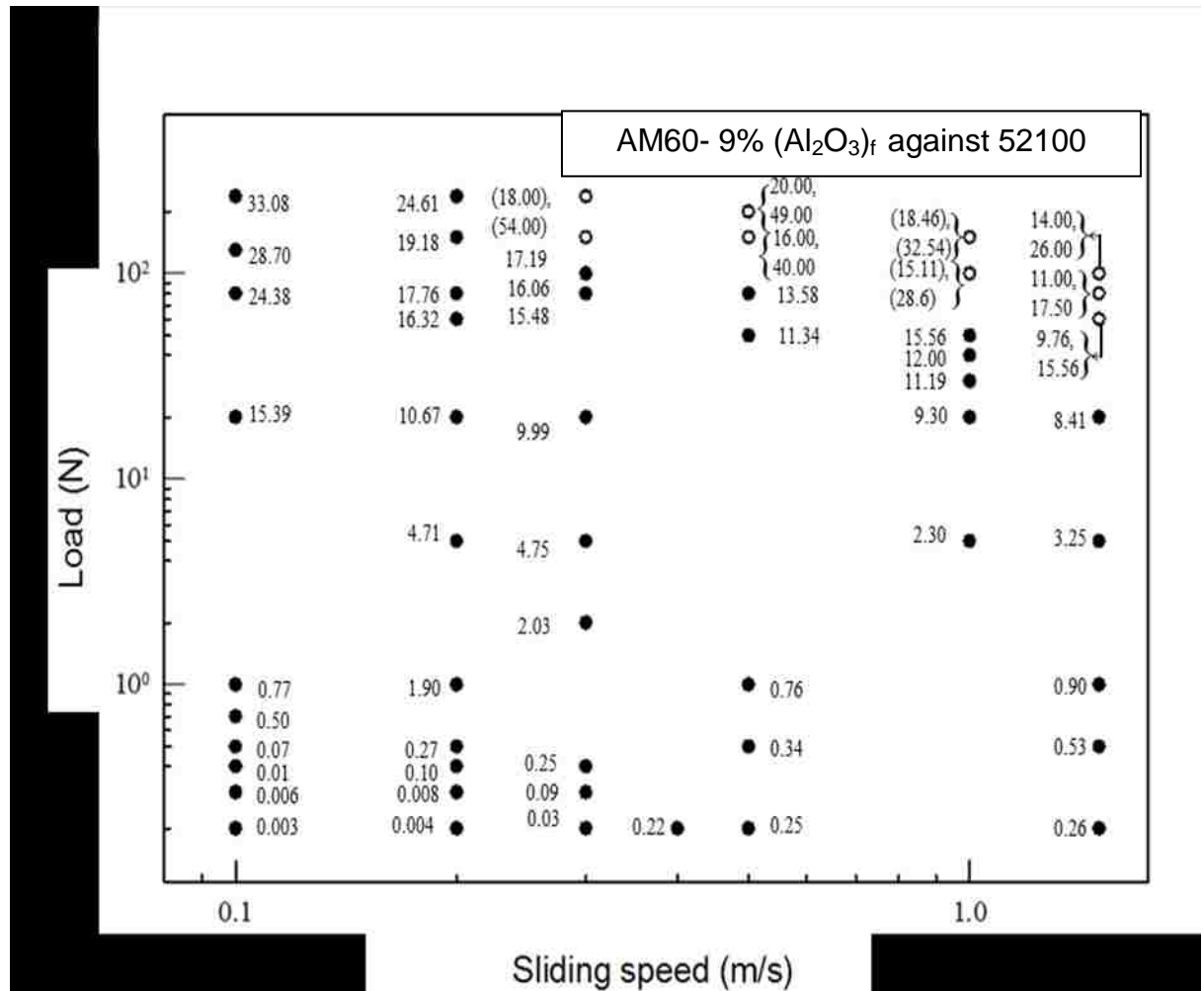
Figure 4.43. Wear rate map for AM60-9% $(Al_2O_3)_f$ composite.

4.5. COF measurement during dry sliding wear

The effect of load on the coefficient of friction (COF) of AM60 with the sliding distance at speeds of 0.1, 0.3, 0.5, 1.0 and 1.5 m/s is shown in Fig. 4.44 - 4.48. It can be seen that the coefficient of friction increases with an increase in load. The coefficients of friction for the mild wear regime (Figs. 4.44-4.46) attained a steady state as shown by COF vs sliding distance plots for 60.0N and 237.8 N at 0.1 m/s (Fig. 4.44), 100.0 and 150.0 N at 0.3 m/s and 0.1 N, 80.0 N, 150.0 N and 200.0 N at 0.5 m/s. However, a continuous rise was noticed in COF for transient and severe wear regime as in the case of 130.0 N at 1.0 m/s (Fig. 4.47) and 80.0 N and 100.0 N at 1.5 m/s (Fig. 4.48). A COF map constructed from such measurements (Fig. 4.49) shows that the COF for mild wear was measured to be less than 0.25 while a COF value greater than 0.45 corresponded to severe wear. The transient wear showed a COF value in the range of 0.25-0.45. The COF values corresponding to the mild wear are the steady state COF value observed from the respective COF plots, while in case of transient and severe wear regimes, the highest measured value during the course of sliding wear tests were plotted in the COF map

Similar COF measurements were carried out for AM60-9% $(Al_2O_3)_f$ composite distance at speeds of 0.1, 0.3, 1.0 and 1.5 m/s is shown in Fig. 4.50 to 4.53. The resulting COF map (Fig.4.54) showed a rise in COF up to 0.65 in the mild wear regime. Transient wear regime showed a decrease in COF 0.35 which was later stabilized at 0.40. In severe wear regime, the COF again shows a rise up to 0.60.

Comparison of the COF maps for AM60 alloy and AM60-9% $(Al_2O_3)_f$ composite show a maximum COF value of 1.10 for AM60 alloy and 0.65 for AM60-9% $(Al_2O_3)_f$ composite

in the mild wear regime. In the severe wear regime, AM60 alloy and AM60-9% $(Al_2O_3)_f$ composite showed almost similar COF of 0.50 and 0.60 respectively.

The COF value for both AM60 alloy and AM60-9% $(Al_2O_3)_f$ composite decreased as the transition from mild to severe wear occurred. This can be attributed to the softening of the sliding surface at higher loads due to frictional heating which is described in detail in section 4.6 and chapter 5.
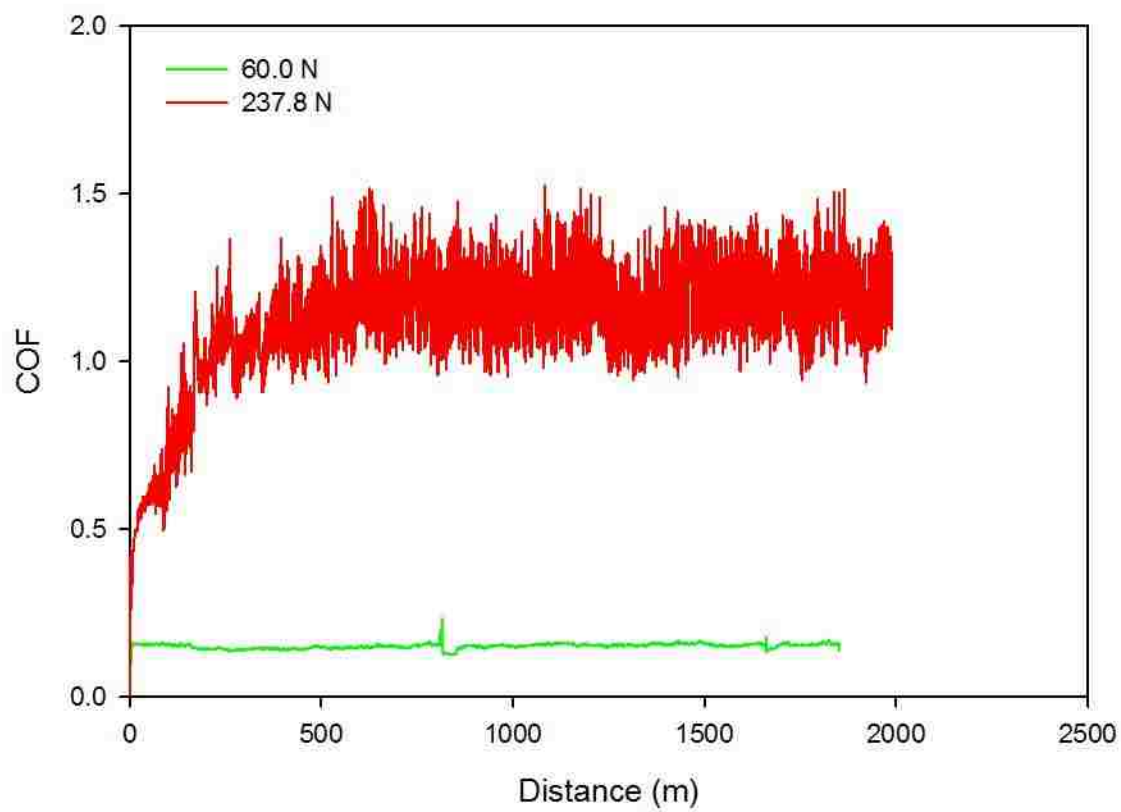
Figure 4.44. COF plots for AM60 alloy tested at 0.1 m/s
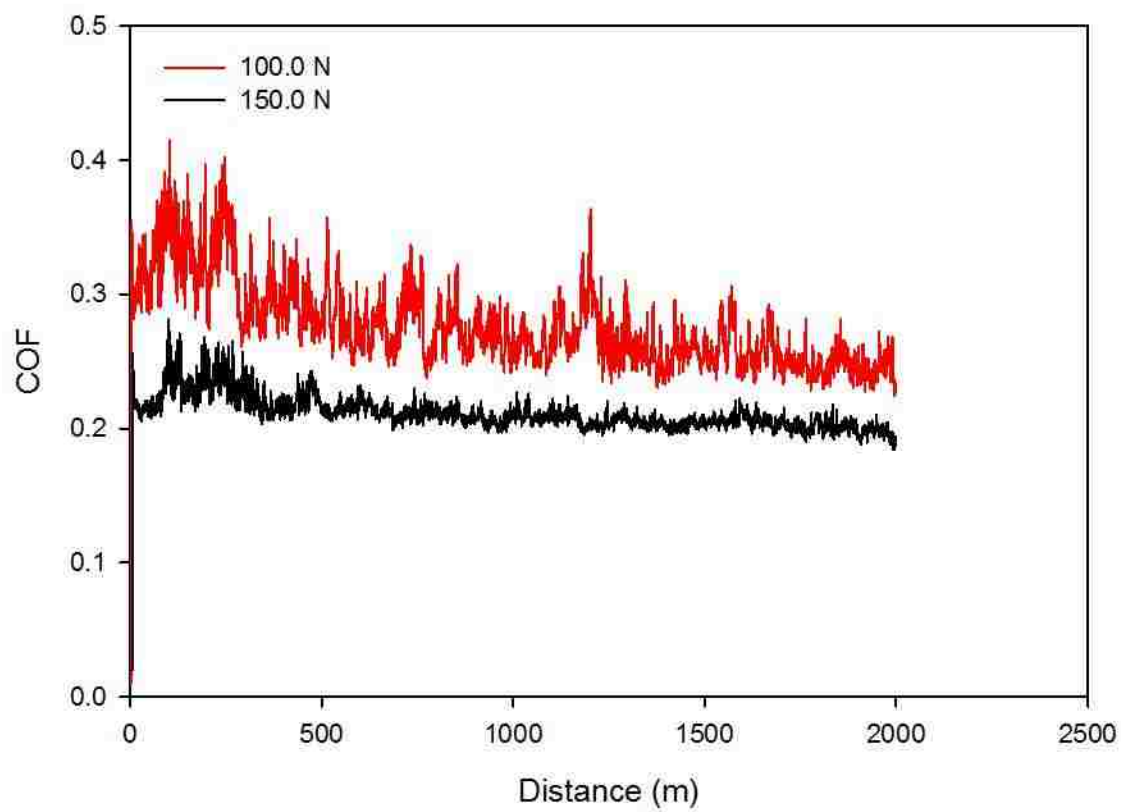
Figure 4.45. COF plots for AM60 alloy tested at 0.3 m/s
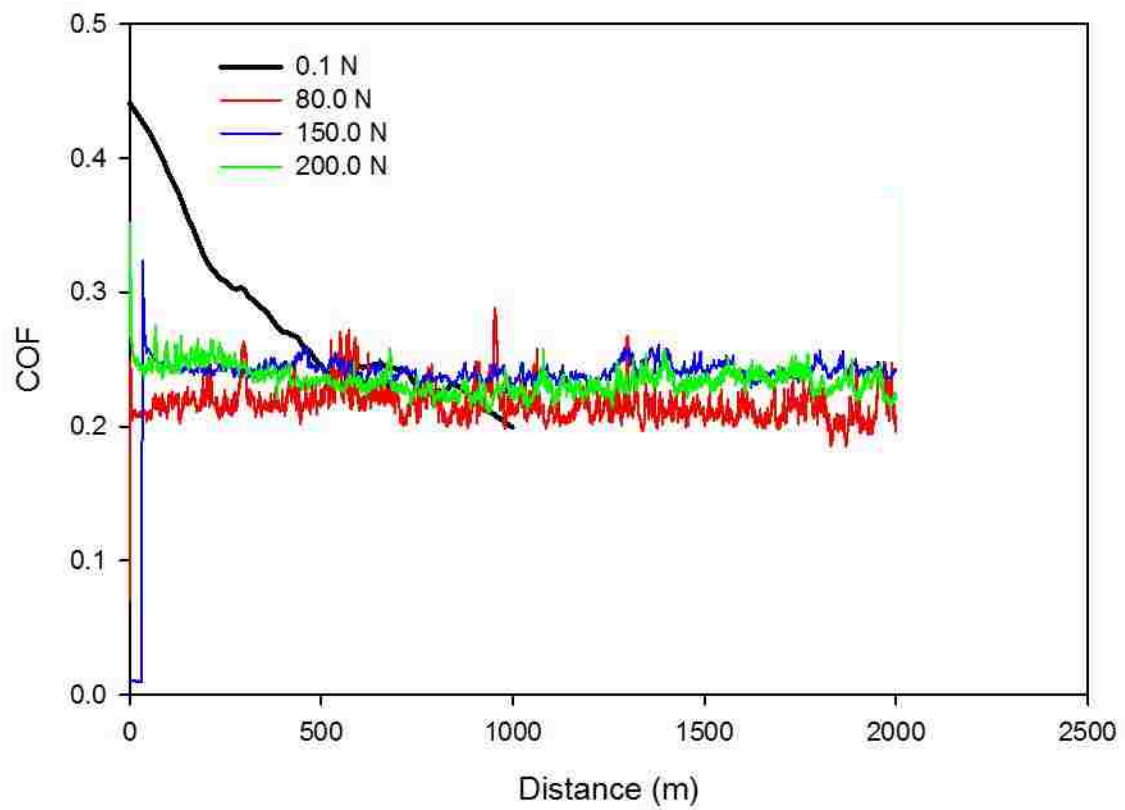
Figure 4.46. COF plots for AM60 alloy tested at 0.5 m/s
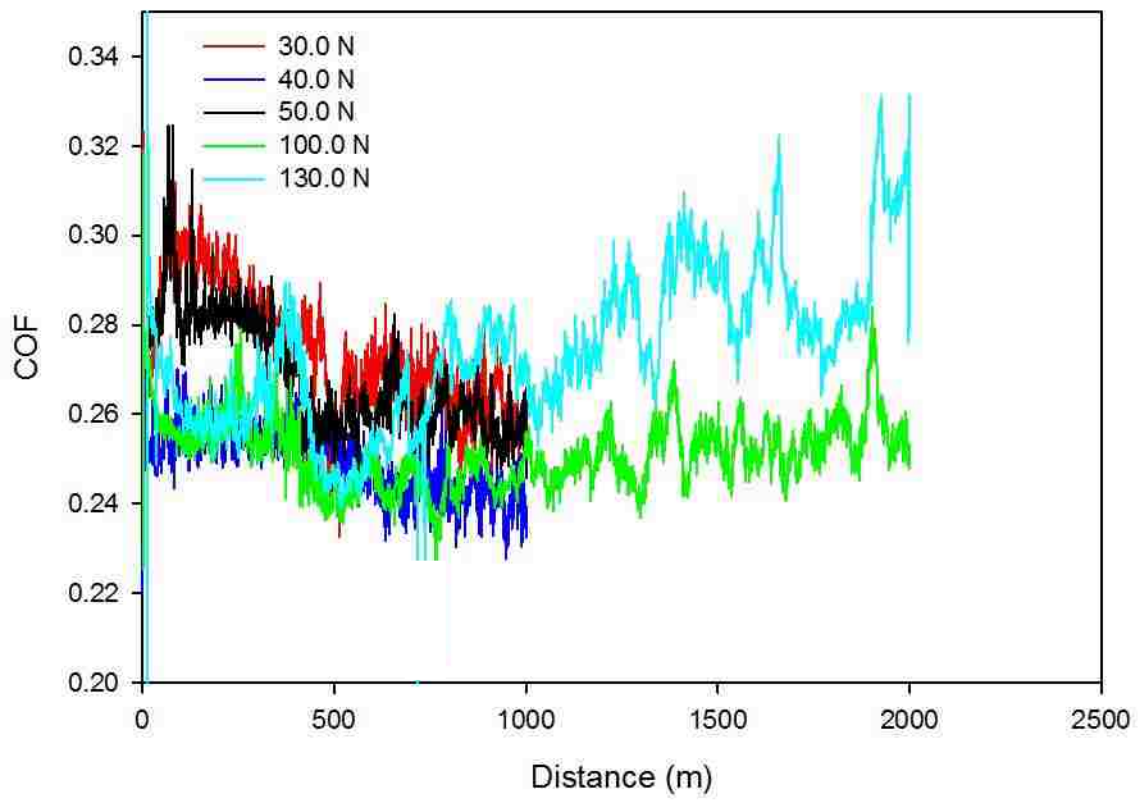
Figure 4.47. COF plots for AM60 alloy tested at 1.0 m/s
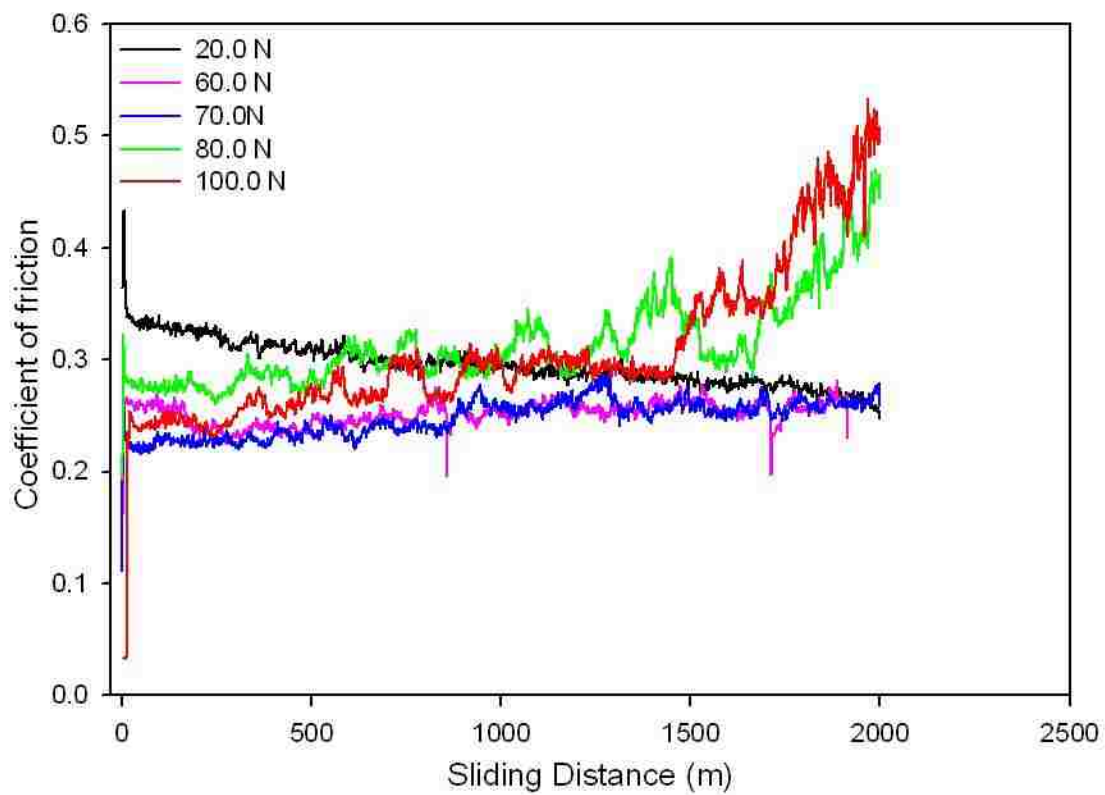
Figure 4.48. COF plots for AM60 alloy tested at 1.5 m/s
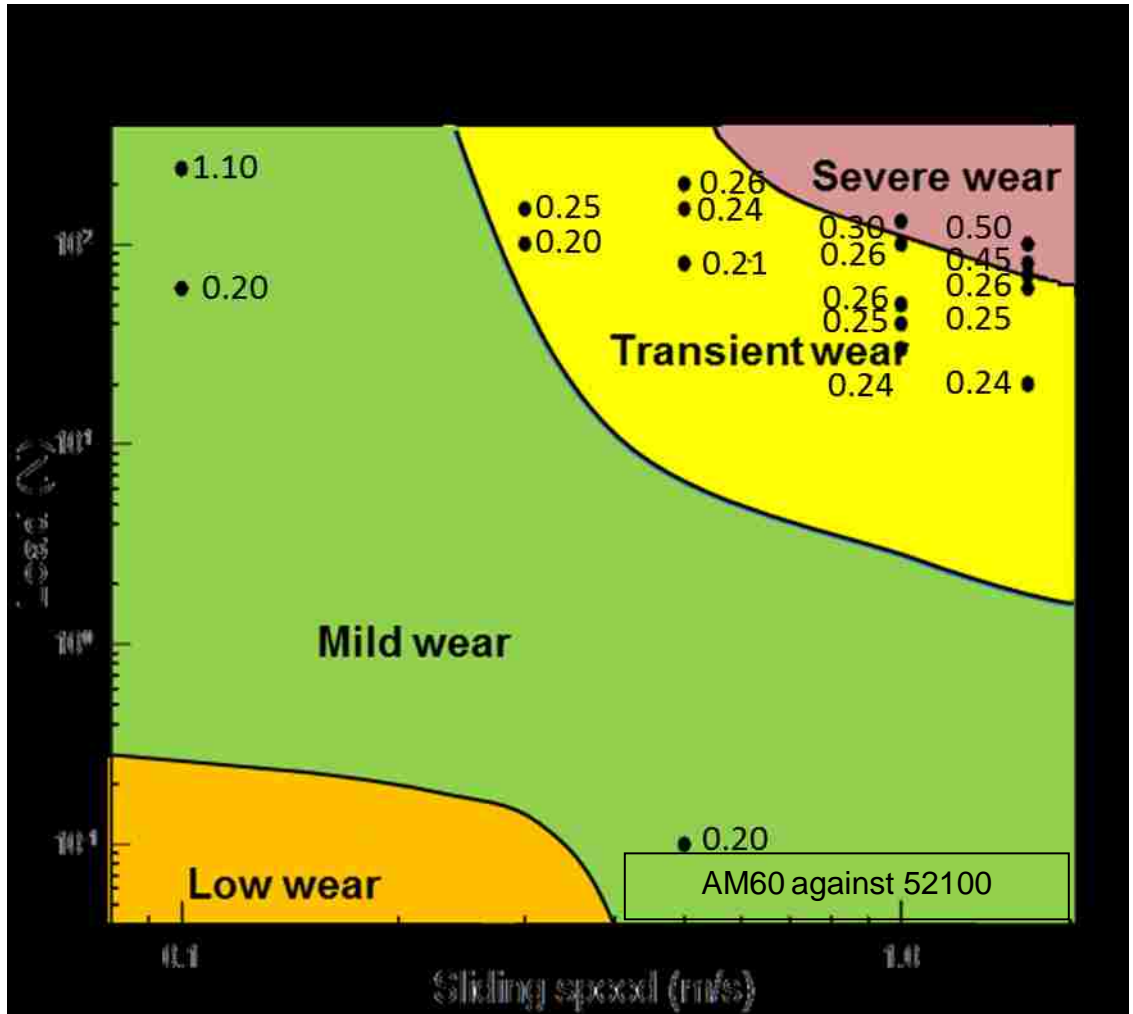
Figure 4.49. COF map for AM60 alloy.
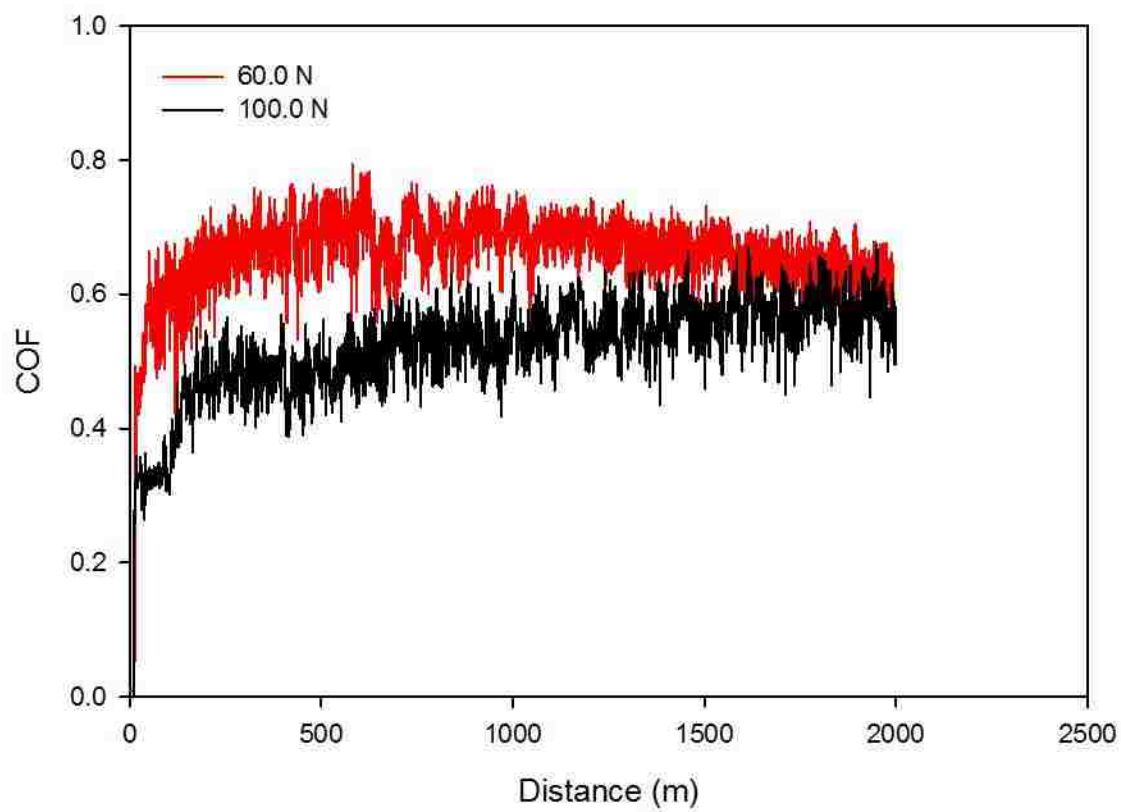
Figure 4.50. COF plots forAM60-9% $(Al_2O_3)_f$ composite tested at 0.1 m/s
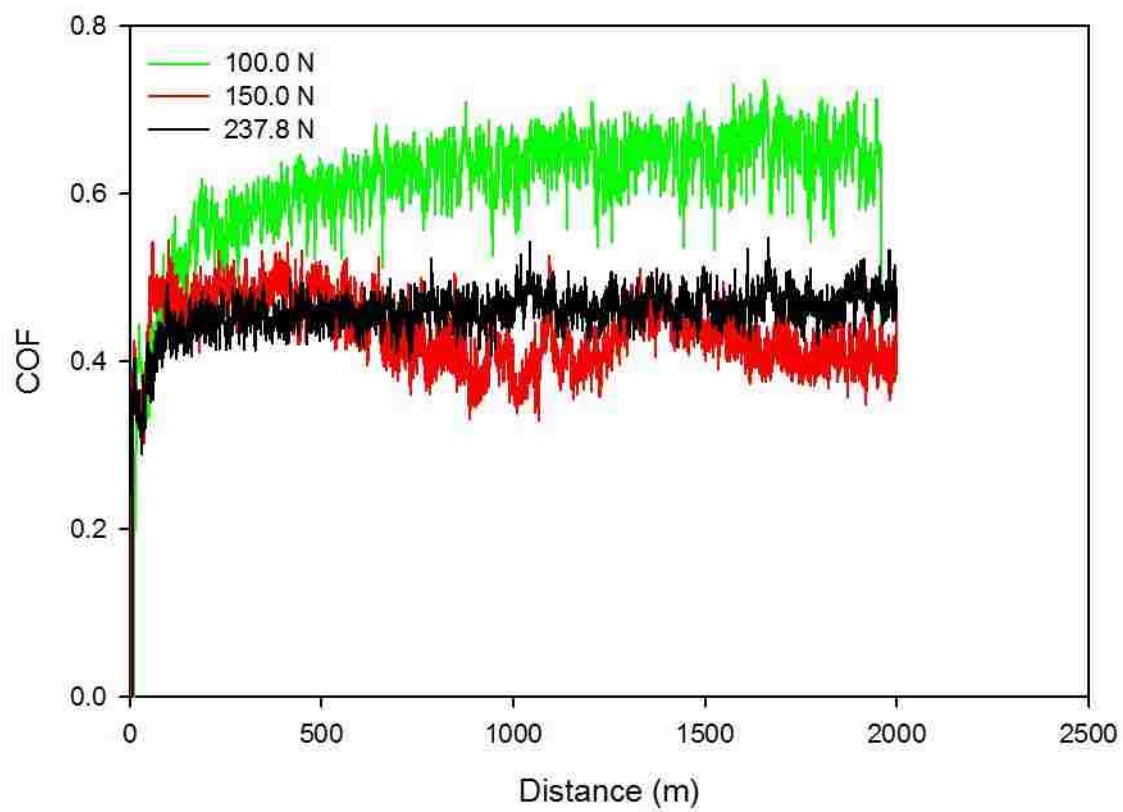
Figure 4.51. COF plots forAM60-9% $(Al_2O_3)_f$ composite tested at 0.3 m/s
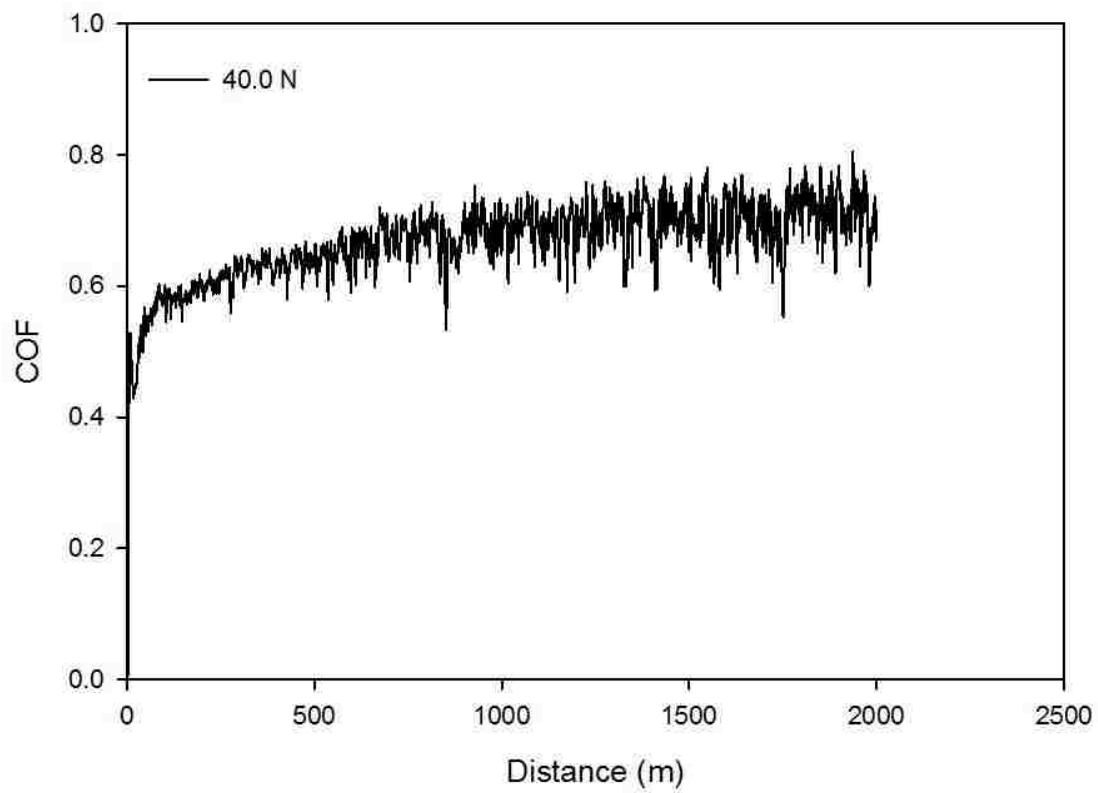
Figure 4.52. COF plots forAM60-9% $(Al_2O_3)_f$ composite tested at 1.0 m/s
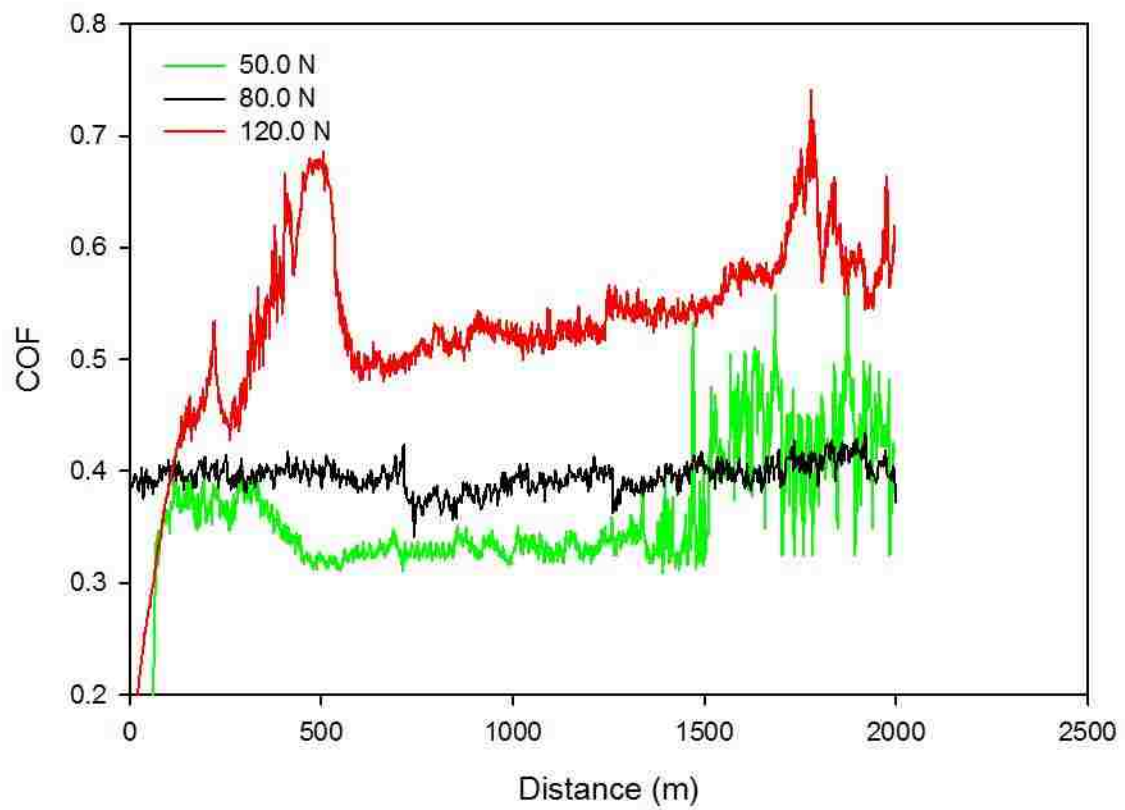
Figure 4.53. COF plots forAM60-9% $(Al_2O_3)_f$ composite tested at 1.5 m/s
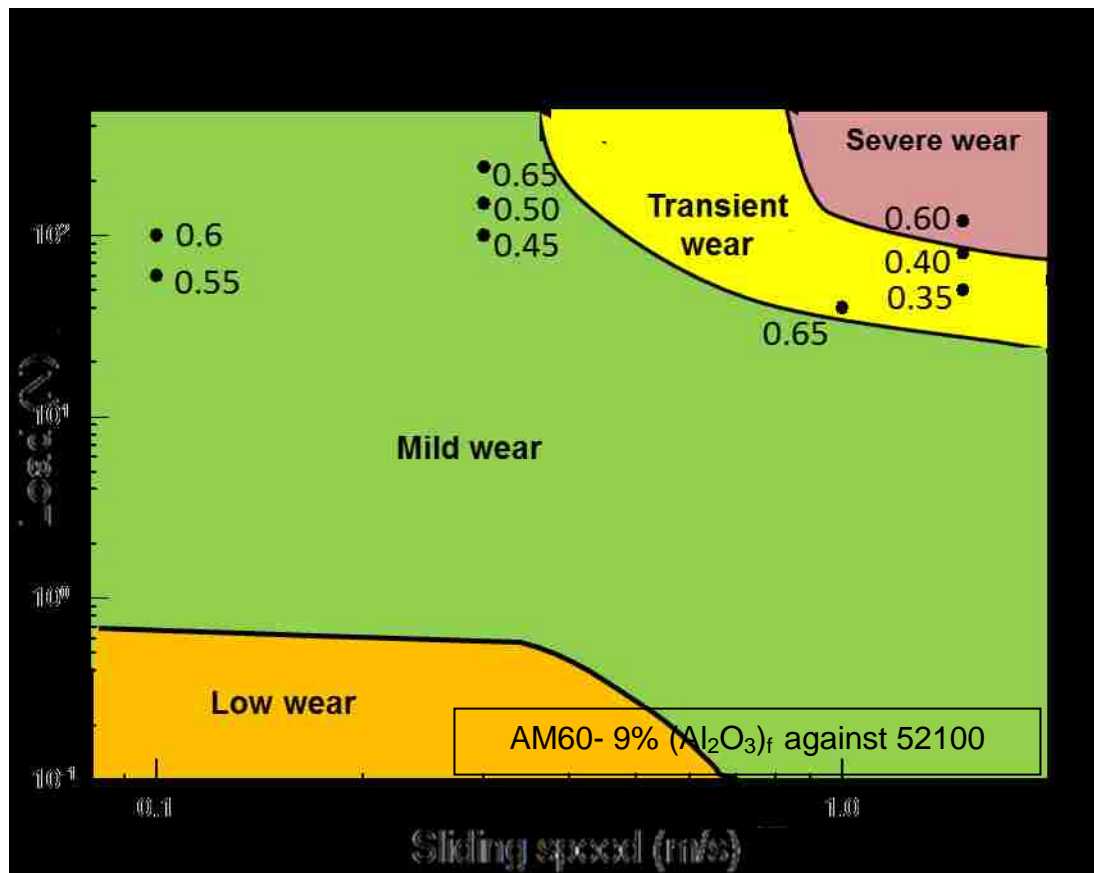
Figure 4.54. COF map for AM60-9% $(Al_2O_3)_f$ composite.

4.6. Temperature increase during dry sliding wear

The effect of load on the surface temperature change of AM60 with the sliding distance at speeds of 0.1, 0.5 and 1.5 m/s is shown in Fig. 4.55-4.57 and Fig. 4.58 for AM60-9% $(Al_2O_3)_f$. It can be seen that the temperature increases with an increase in load. Steady state temperature plots were observed under mild wear regime as shown in case of 0.1 m/s and 0.5 m/s. The discontinuity in the temperature plots for 80.0 N and 150.0 N at 0.5 m/s can be observed due to the shifting of the thermocouple from one hole to another. This shifting was necessary to prevent damage to the thermocouple during the sliding wear test in cases where extensive wear occurred to the sample. A temperature of up to 340 K was measured in the mild wear regime. At 60.0 N and 1.5 m/s, a slow rise in temperature was observed up to 386 K. Such slow increase in temperature above a critical temperature value of 349 K was observed to be a characteristic of transient wear. However, temperature plot for severe wear exhibited a continuous increase up to 548 K at 100.0 N for AM60 alloy and 654 K at 120.0 N for AM60-9% $(Al_2O_3)_f$ composite. Such rise in temperature resulted in the thermal softening of the sliding surfaces of AM60 and AM60-9% $(Al_2O_3)_f$. The observed temperatures measured at each load and speed combination are summarized in the temperature maps for both materials are presented and discussed in detail along with the effect of temperature on the transition in Chapter 5.
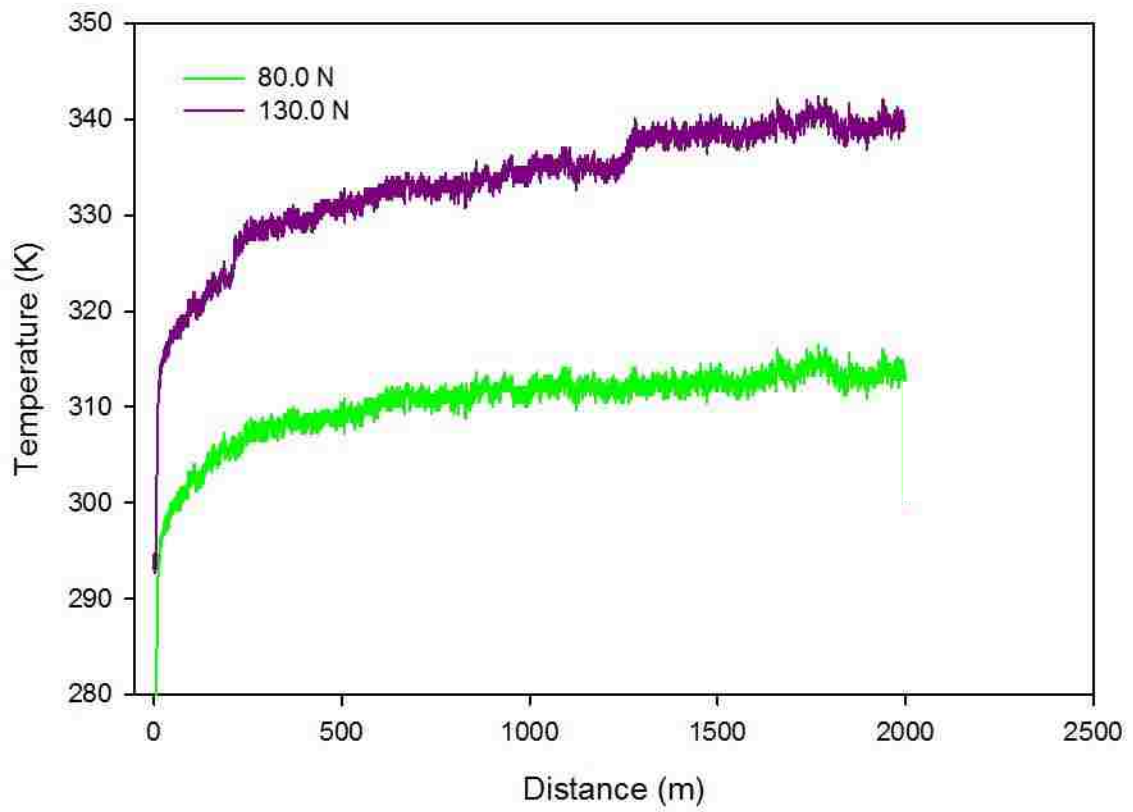
Figure 4.55.Temperature plots for AM60 alloy tested at0.1 m/s.
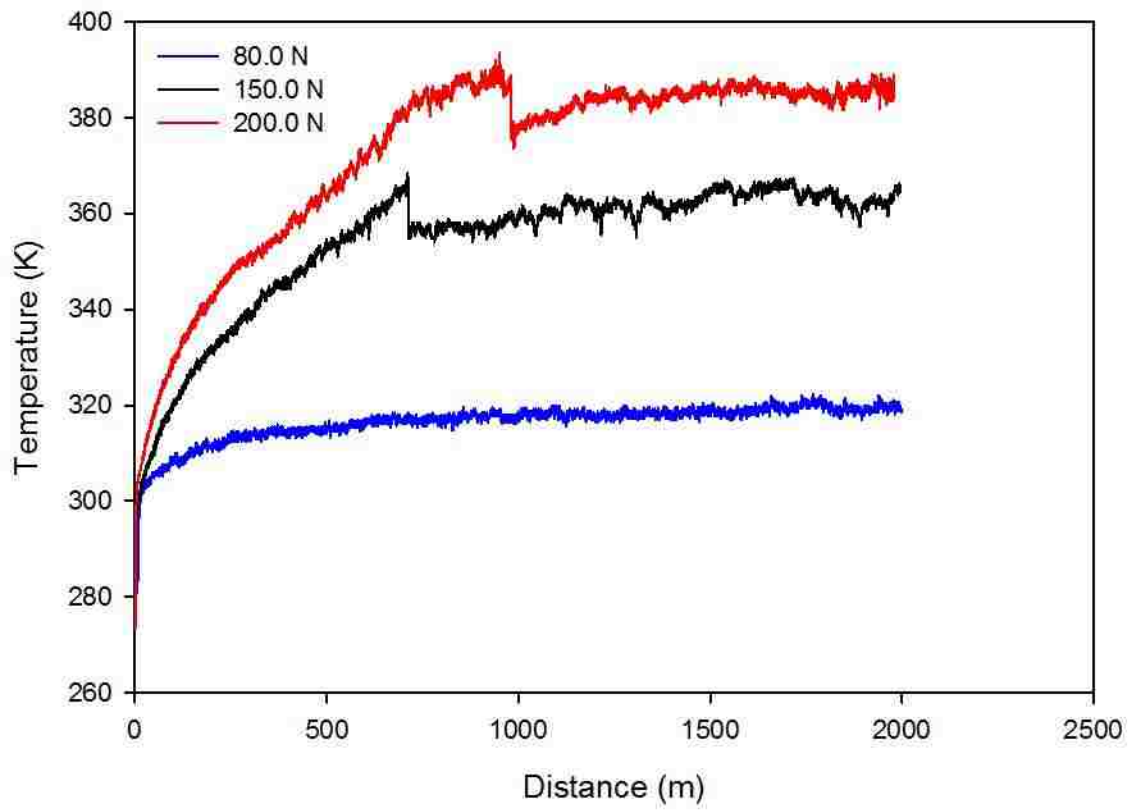
Figure 4.56.Temperature plots for AM60 alloy tested at0.5 m/s
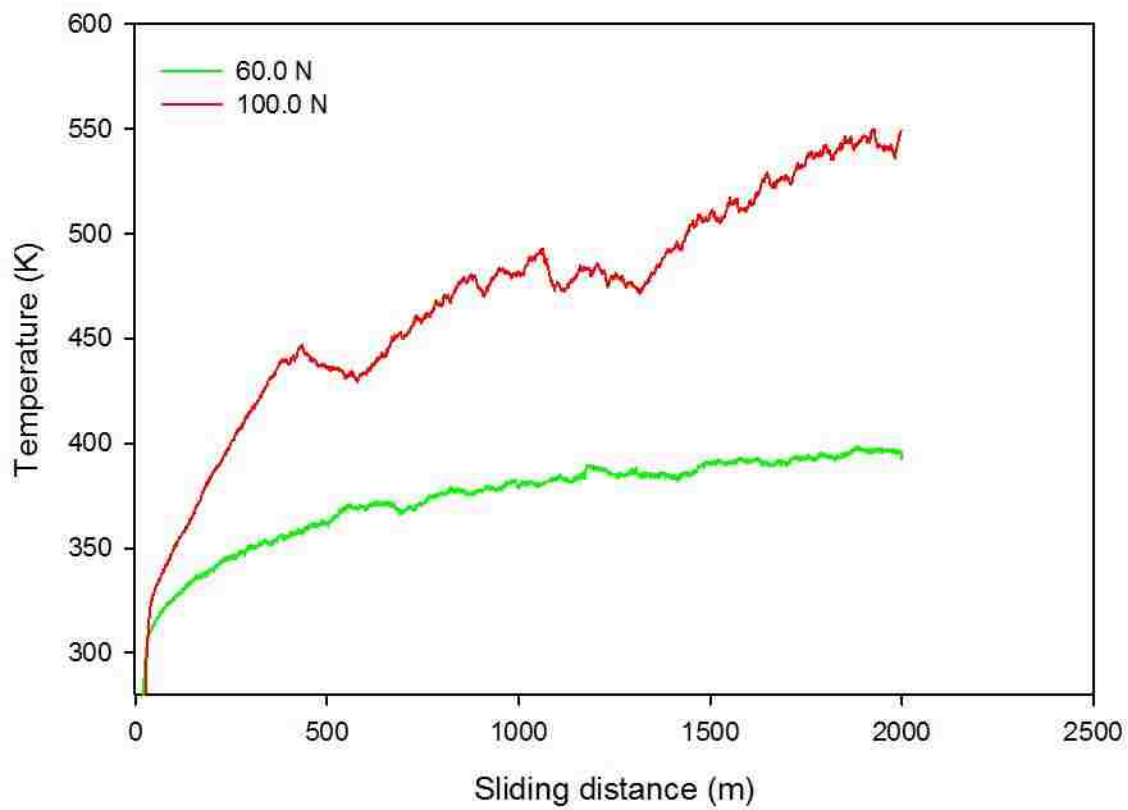
Figure 4.57.Temperature plots for AM60 alloy tested at1.5 m/s.
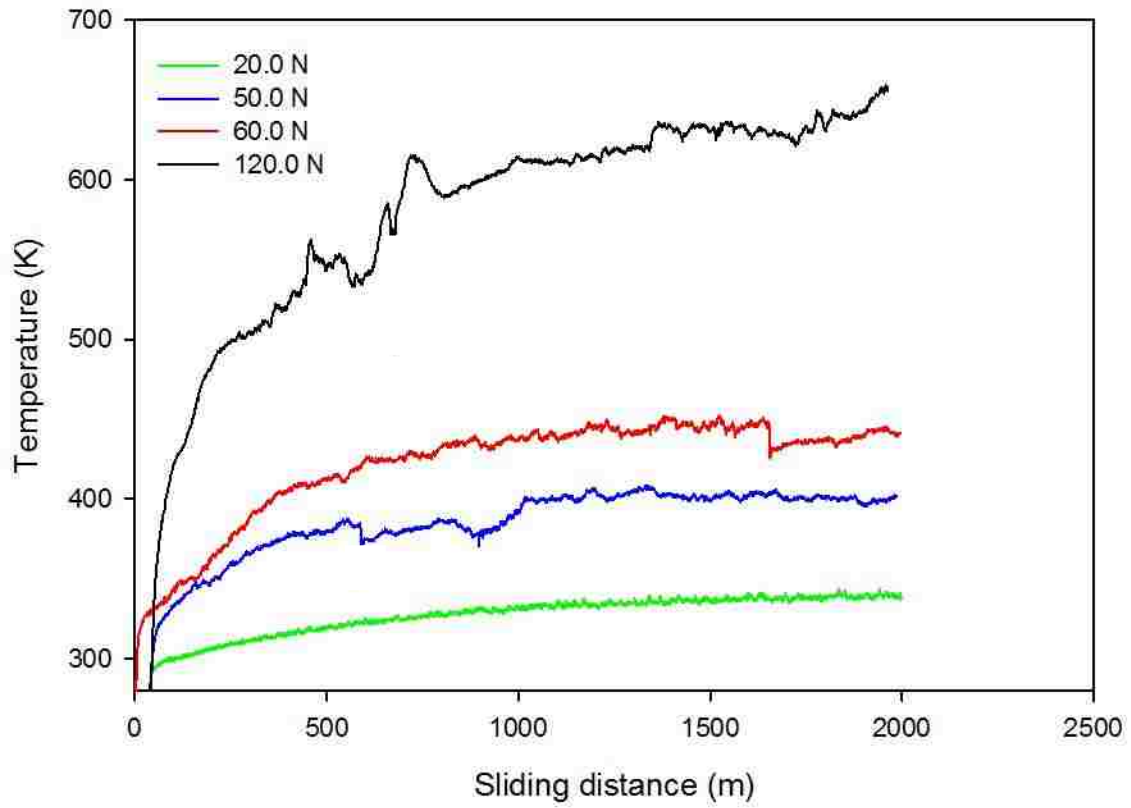
Figure 4.58.Temperature plots forAM60-9% $(Al_2O_3)_f$ composite tested at 1.5 m/s

Chapter 5: Discussion

5.1. Introduction

In the previous chapter, the wear maps for AM60 alloy and AM60-9% $(Al_2O_3)_f$ composite were constructed. The wear maps for both of these materials consisted of low, mild, transient and severe wear regimes. The transition from mild to severe wear was found to be not abrupt and an intermediate regime termed as transient wear regime was suggested to exist between mild and severe wear. The transition from mild to severe wear, however, was found to be dependent on the temperature. The transient wear regime initially showed characteristics of mild wear regime i.e. oxidation wear, while with the progression of the wear process, evidence of plastic deformation induced wear mechanism suggested the initiation of the severe wear regime. Severe wear occurred when the bulk temperature exceeded the critical transition temperature (T_c).

In this chapter, the dependence of temperature on the transition from mild to severe is further discussed in detail. Effort has been made to prove that oxidation wear is followed by plastic deformation induced wear as wear progresses in the transient wear regime. The critical transition temperature is shown to coincide with the recrystallization temperature as postulated by Ling and Saibel [72]. Results of forced cooling experiment, as previously performed by Zhang and Alpas [58], is also presented, supporting the argument that transition is dependent on the bulk temperature of the specimen. A delay in transition from mild to severe wear regime was also observed as the load is decreased within the transient wear regime.

5.2. Effect of temperature on the transition from mild to severe wear

As explained in chapter 4, a steady-state wear is observed in the mild wear regime (Fig. 5.1). However, for a particular sliding speed, the wear rate is accelerated upon increasing the applied load. Fig. 5.2 shows the example of transient wear at 50.0 N and 1.5 m/s, where, mild wear prevails up to 1000 m with a wear rate of 8 x 10^{-3} mm^3/m after which accelerated wear was observed increasing the wear rate up to 22 x 10^{-3} mm^3/m. Similarly, a slight increase in load shows a shorter mild wear region with a wear rate of 10 x 10^{-3} mm^3/m after which accelerated wear was observed increasing the wear rate up to 30 x 10^{-3} mm^3/m. A further increase in the load exhibited an abrupt rise in wear rate up to 44 x 10^{-3} mm^3/m which suggested the beginning of severe wear regime.

The temperature measurements at these loads-speed combinations showed that the sliding conditions at which the temperature remained below 349 K (recrystallization temperature for Mg) exhibited mild wear condition. Occurrence of dynamic recrystallization, as proven earlier by various researchers [65,73,74] was evident along the subsurface strain gradients was evident. The extent to which the surface temperatures were higher than the critical temperature determined the category of the wear process among transient and severe wear. The temperatures for 50.0 N and 60.0 N were measured to be 397 K and 428 K respectively. The wear process under these sliding conditions was categorized as transient wear in contrast to 120.0 N for which the temperature exceeded 600 K. Within the transient wear, the distance at which transition occurred also coincided with the distance at which the temperature exceeded T_c.
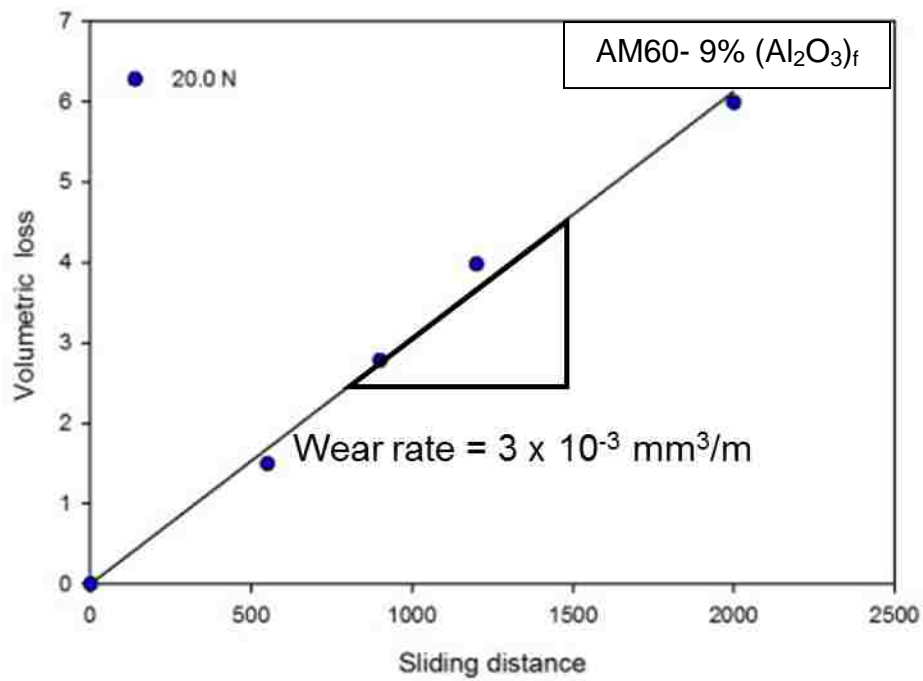
Figure 5.1. Volumetric loss vs. Sliding distance plot for AM60-9% $(Al_2O_3)_f$ composite at 20.0 N and 1.5 m/s
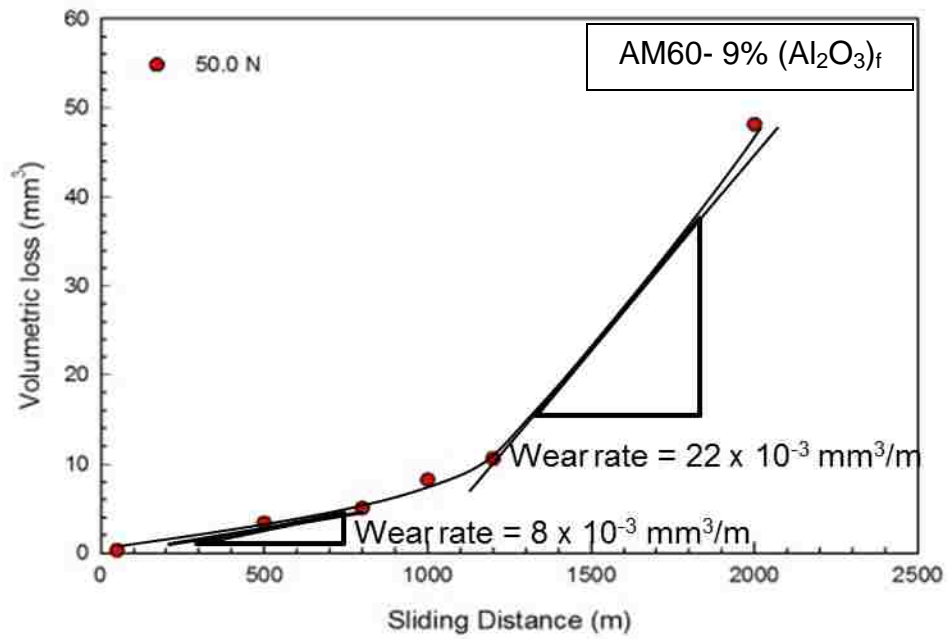
Figure 5.2. Volumetric loss vs. Sliding distance plot for AM60-9% $(Al_2O_3)_f$ composite at 50.0 N and 1.5 m/s
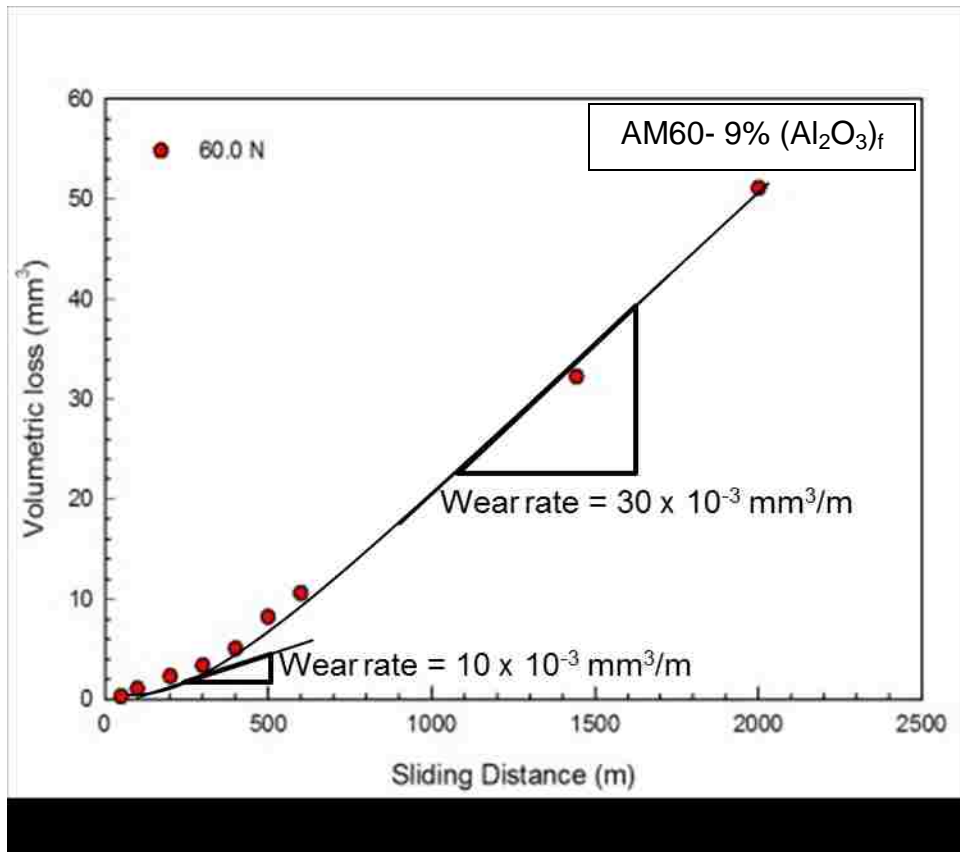
Figure 5.3. Volumetric loss vs. Sliding distance plot for AM60-9% $(Al_2O_3)_f$ composite at 60.0 N and 1.5 m/s.
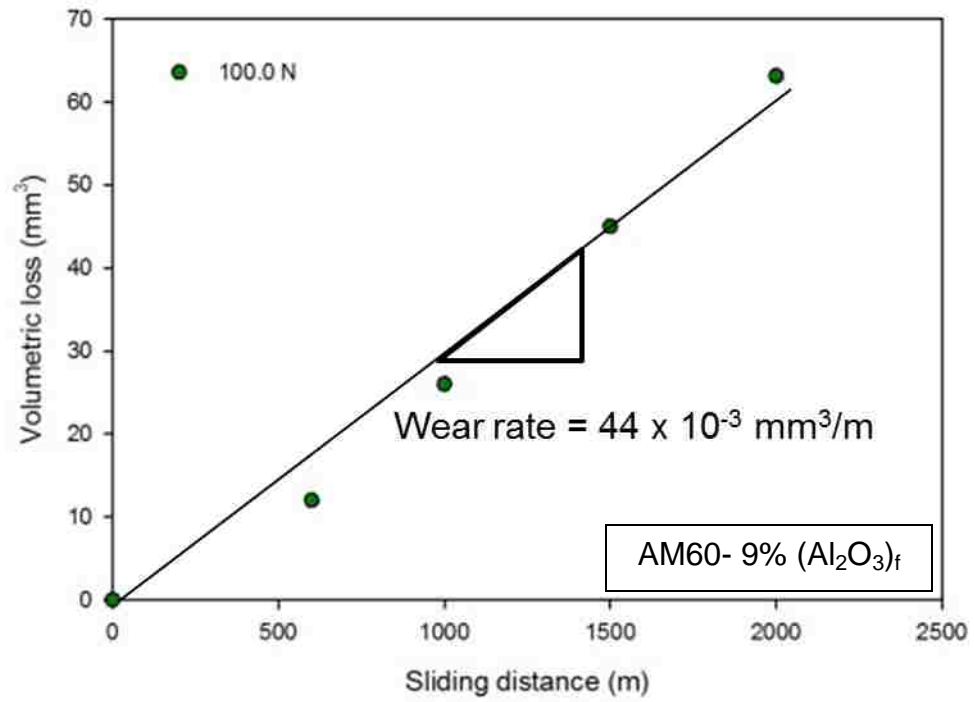
Figure 5.4. Volumetric loss vs. Sliding distance plot for AM60-9% $(Al_2O_3)_f$ composite at 120.0 N and 1.5 m/s.
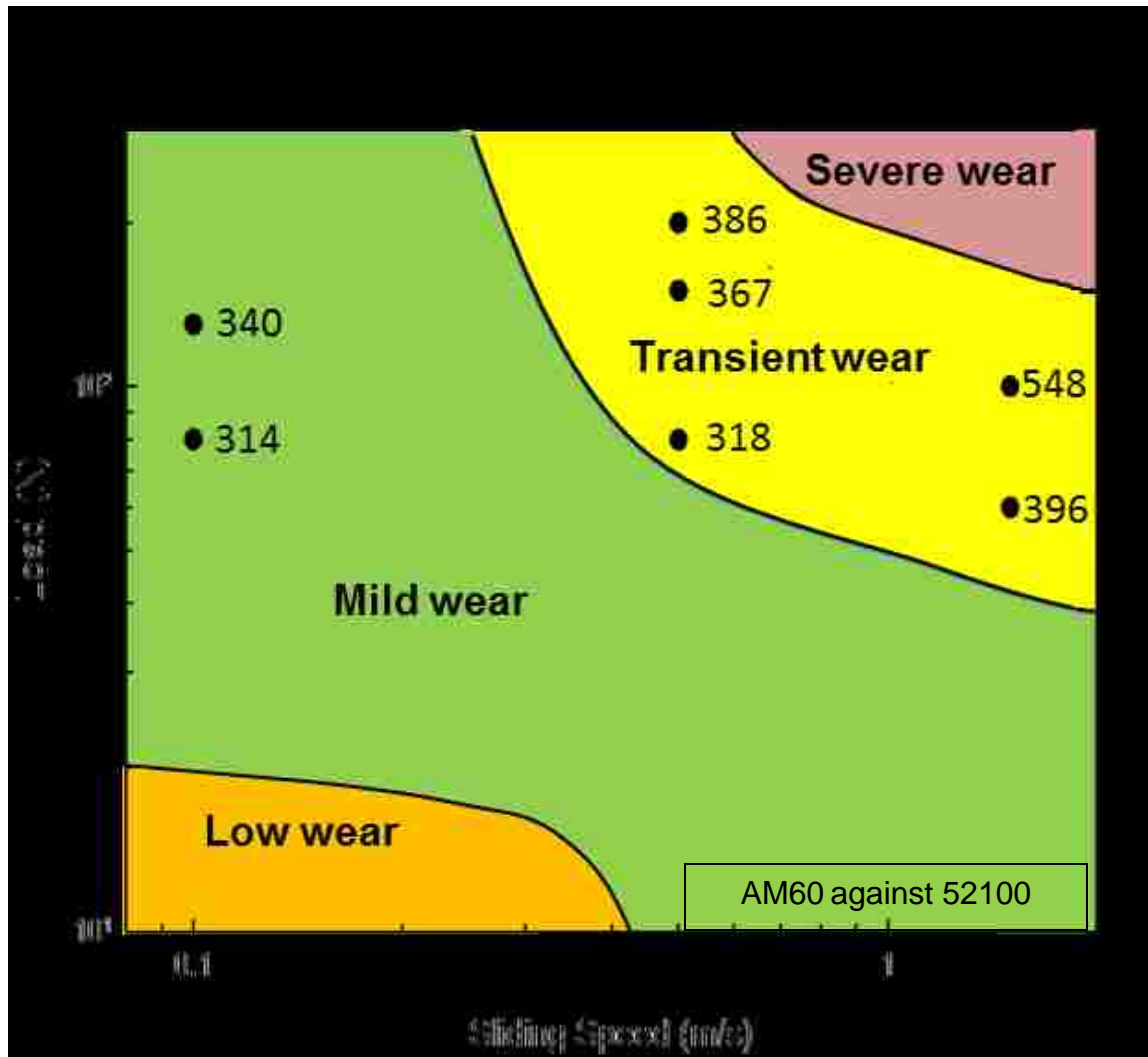
Figure 5.5.Temperature map for AM60 alloy.
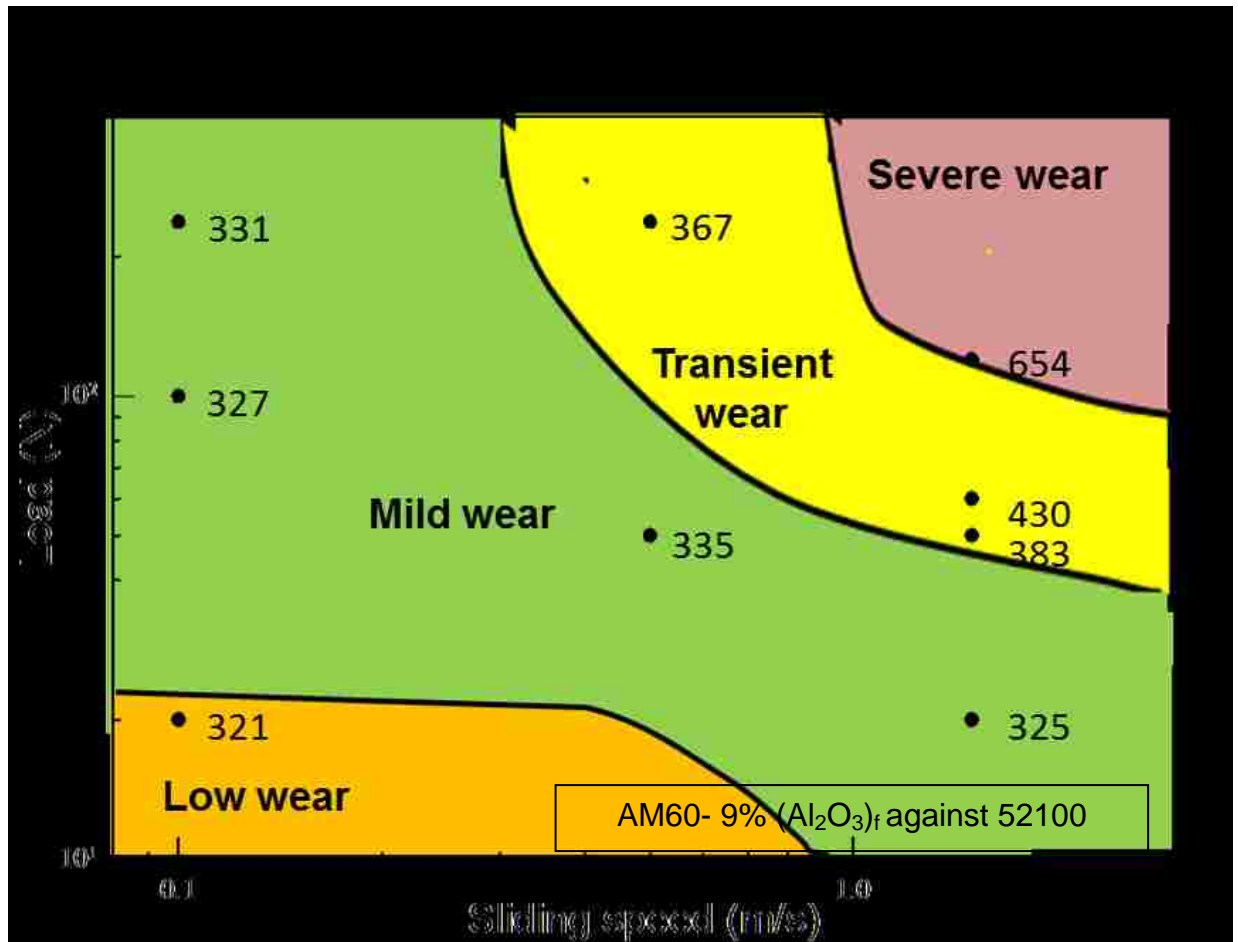
Figure 5.6. Temperature map forAM60-9% $(Al_2O_3)_f$ composite.

5.3. Delay in transition from mild to severe wear

When comparing the wear process of 50.0 N and 60.0 N at 1.5 m/s, it is important to note that there is a delay in transition from mild to severe wear within transient wear regime (Fig. 5.12). At 50.0 N, the distance at which transition occurs is 1000 N, while at 60.0 N, the distance to transition is 500 m. This delay in transition can be attributed to the attainment of the transition temperature (Fig. 5.13) [49].

5.4. Roughness measurement of the worn surfaces

Besides the compositional changes mentioned in section 4.3, the roughness of the worn surfaces also provide a basis to distinguish between mild and severe wear. This criteria was followed to investigate the transition from mild to severe wear in the transient wear regime using optical profilometer WYKO NT-1100. At 60.0 N and 1.5 m/s, it was observed that the roughness was initially high up to 2.08 µm at 50 m (Fig. 5.6). The high roughness was maintained up to 500 m (Fig. 5.7). However, at 600 m, a low average roughness around 0.50 µm was observed (Fig. 5.8) This low roughness feature was observed up to 2000 m. Here, it is important to note that the transition from mild wear at the above mentioned sliding condition was also observed to occur around 600 m. An average roughness value of 2.25 µm in the mild wear regime at 20.0 N and 1.5 m/s was found to prevail up to 2000 m (Fig. 5.9). This value was found to match the average roughness value of the worn surface that showed mild wear in the transient wear regime (Fig. 5.10 a and b). However, the roughness of the worn surface after transition showed similar value as that of the severe wear at 120.0 N and 1.5 m/s i.e. ~ 0.5 µm (Fig. 5.11).
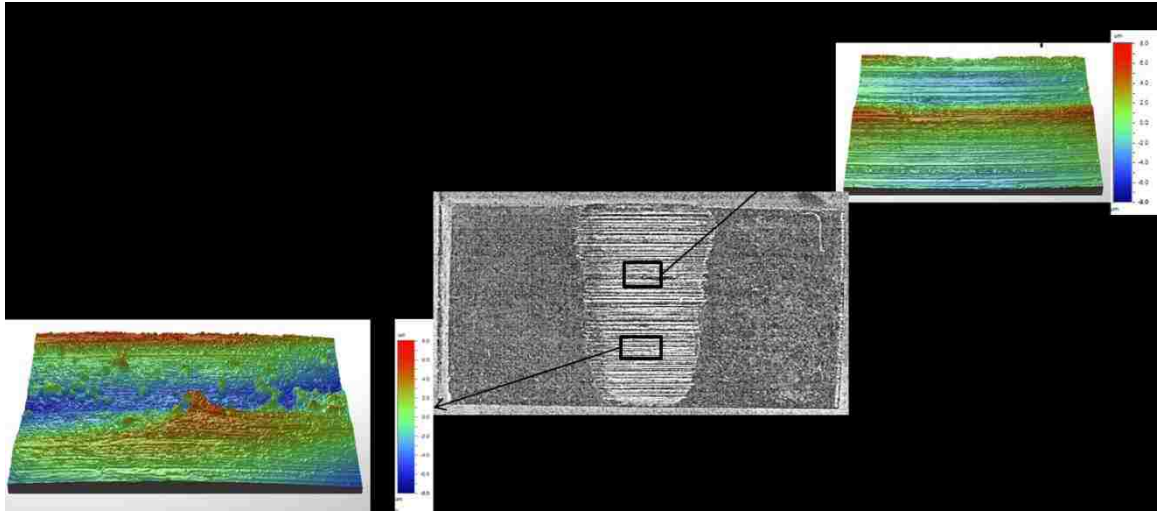
Figure 5.7. 3D profiles showing high roughness all over the worn surface mapped on stereo micrograph for worn surfaces obtained at 60.0 N and 1.5 m/s at 50 m.
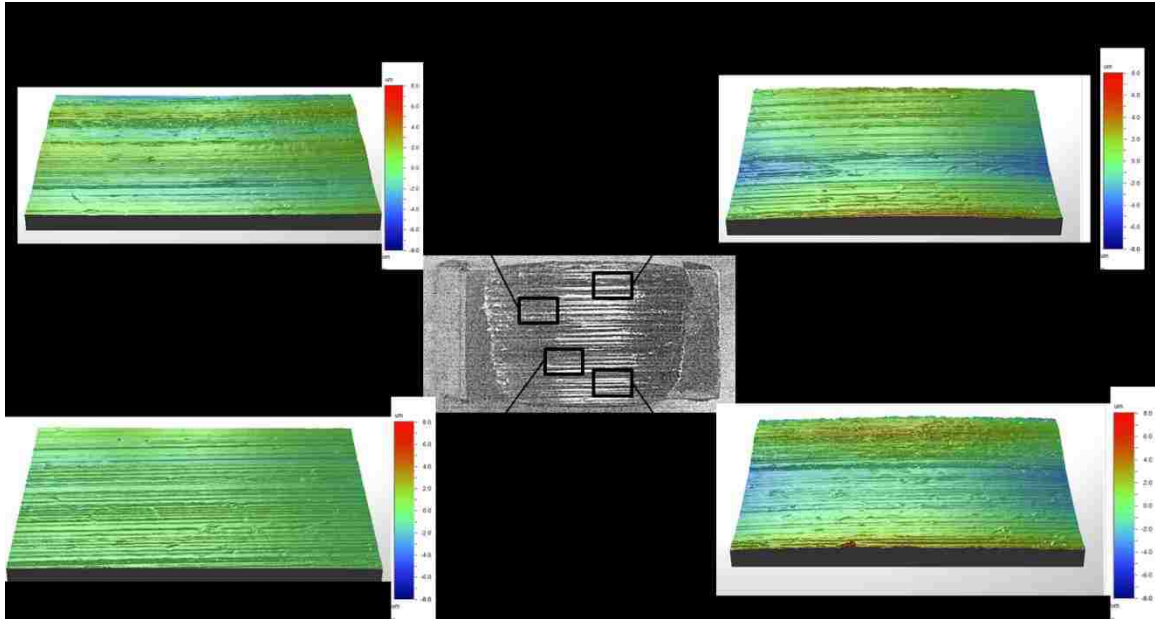
Figure 5.8. 3D profiles showing fluctuating roughness mapped on stereo micrograph for worn surfaces obtained at 60.0 N and 1.5 m/s at 500 m
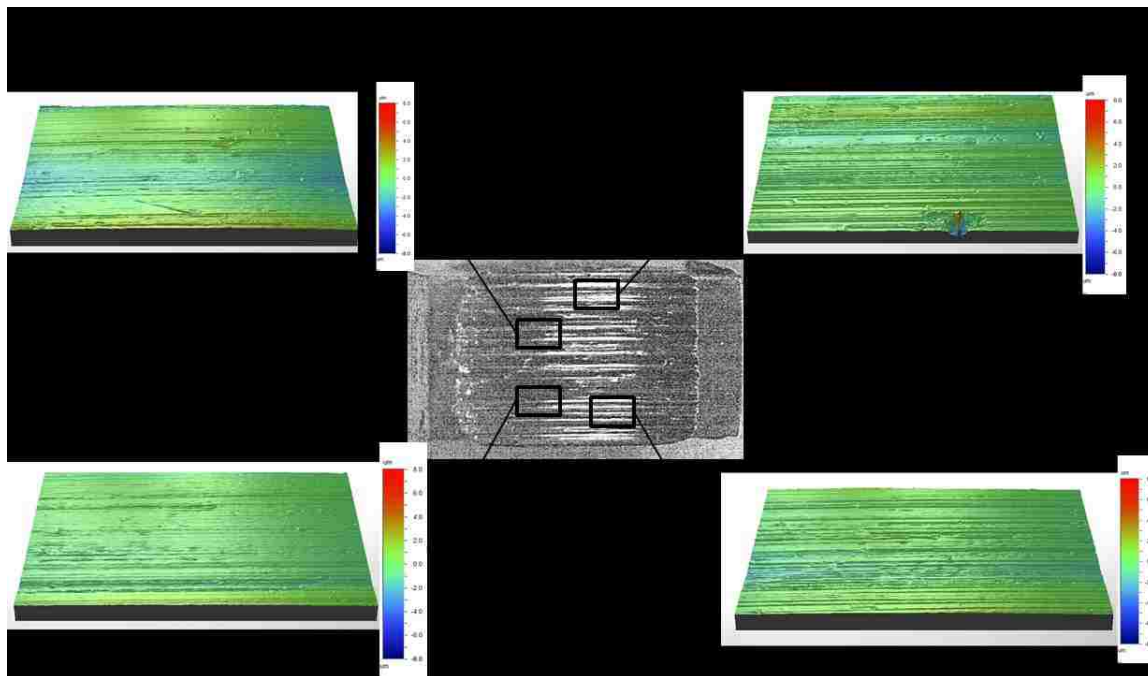
Figure 5.9. 3D profiles showing low roughness throughout the worn surface mapped on stereo micrograph for worn surfaces obtained at 60.0 N and 1.5 m/s at 600 m
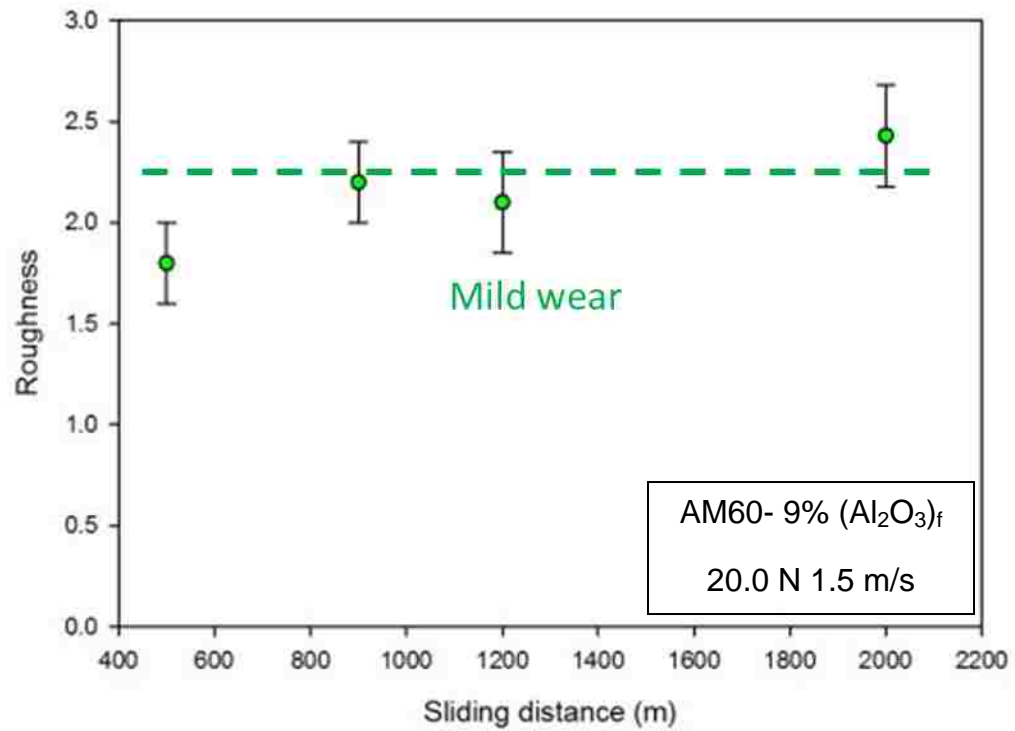
Figure 5.10. Roughness plot for AM60-9% $(Al_2O_3)_f$ composite at 20.0 N and 1.5 m/s.
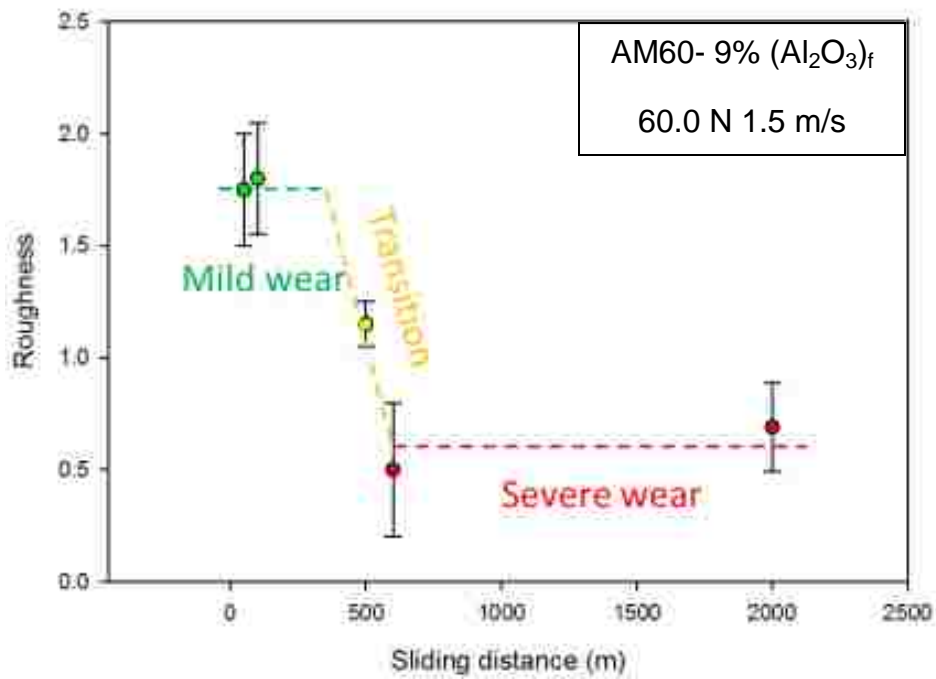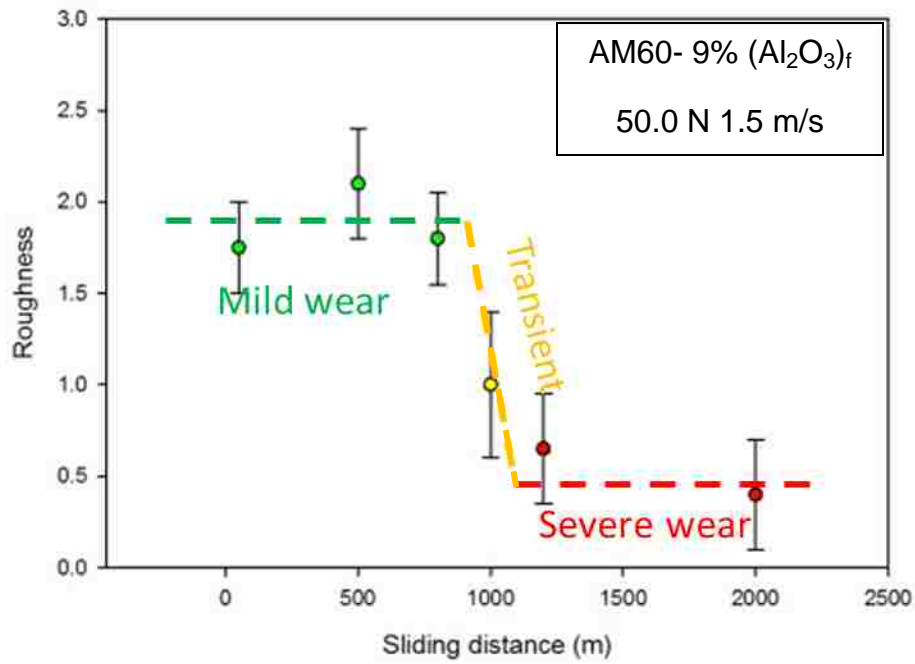
Figure 5.11. Roughness plot for AM60-9% $(Al_2O_3)_f$ composite at (a) 50.0 N, (b) 60.0 N and 1.5 m/s.
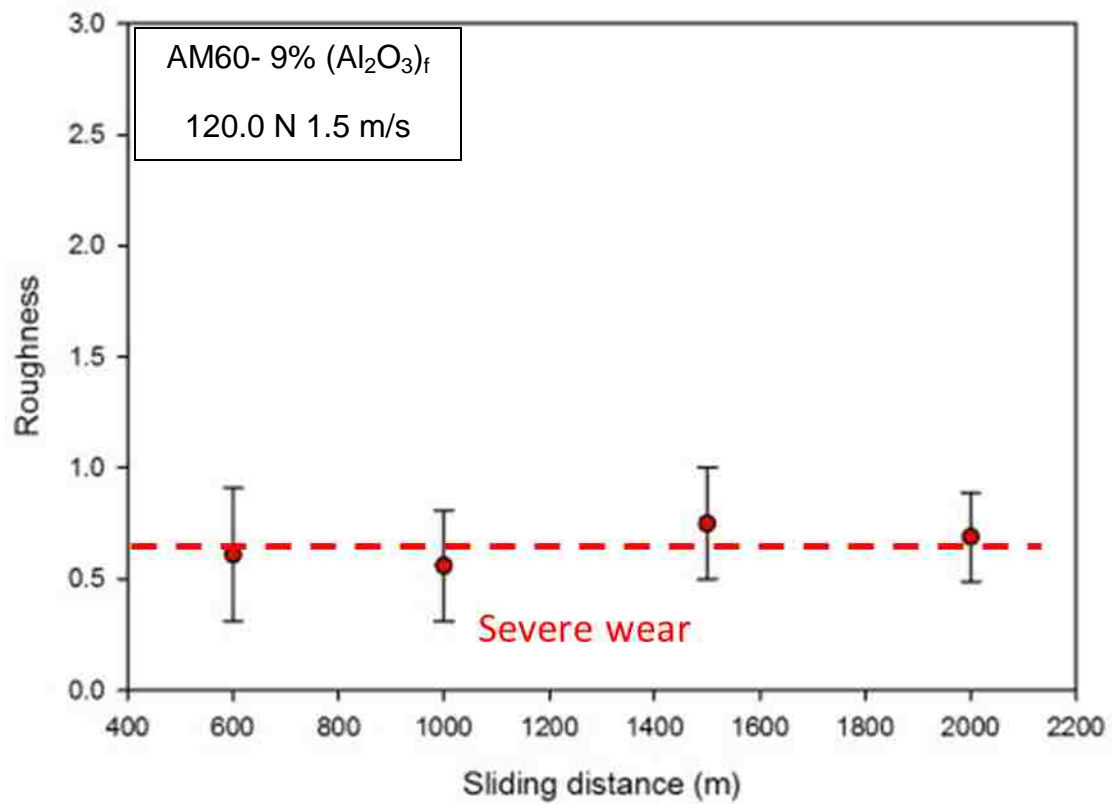
Figure 5.12. Roughness plot for AM60-9% $(Al_2O_3)_f$ composite at 120.0 N and 1.5 m/s.

5.5. Forced cooling experiment

An efficient method of delaying the transition from mild to severe wear is by cooling the sample below transition temperature [49]. Forced cooling experiment 60.0 N and 1.5 m/s, at which transient wear has been observed previously, was carried out by cooling down the sample block using ethanol. A hole was drilled in the sample and ethanol was passed through the sample through these whole using the nozzles (Fig. 5.14). The comparison of the volumetric loss vs. sliding distance plot for the un-cooled and force-cooled specimens is shown in figure 5.15(a). The force-cooled specimen exhibited mild wear because the temperature of the specimen was restricted below 349 K (Fig. 5.15). The transition from mild to severe wear was hindered in the force-cooled specimen as the flash temperature for the force-cooled specimen was limited to 340 K in contrast to 450 K for the uncooled specimen. The flash temperatures were calculated using the following equations in table 5.1.

By observing the temperature plots in figure 4 (b) and 5 (a), (b) and (c), it was concluded that the transition was observed to take place beyond 349 K i.e. recrystallization temperature for Mg.

Table 5-1. Calculation of flash temperature for uncooled and force-cooled experiments.

Test parameters	T_b (K)	COF	F	A_r	K_s	K_c	l_s	l_c	V	$\mu F V / A_r$	$(K_s/l_s)+(K_c/l_c)$	ΔT (°C)	T_f (K)
AM60-9% $(Al_2O_3)_f$ vs. 52100 steel													
60.0 N, 1.5 m/s	450	0.4	60	0.00005	61	46	0.01	0.11	1.5	720000	6146.11	117.14	567.14
60.0 N, 1.5 m/s forced cooling	340	0.5	60	0.00005	61	46	0.01	0.11	1.5	810000	6146.11	131.79	471.79
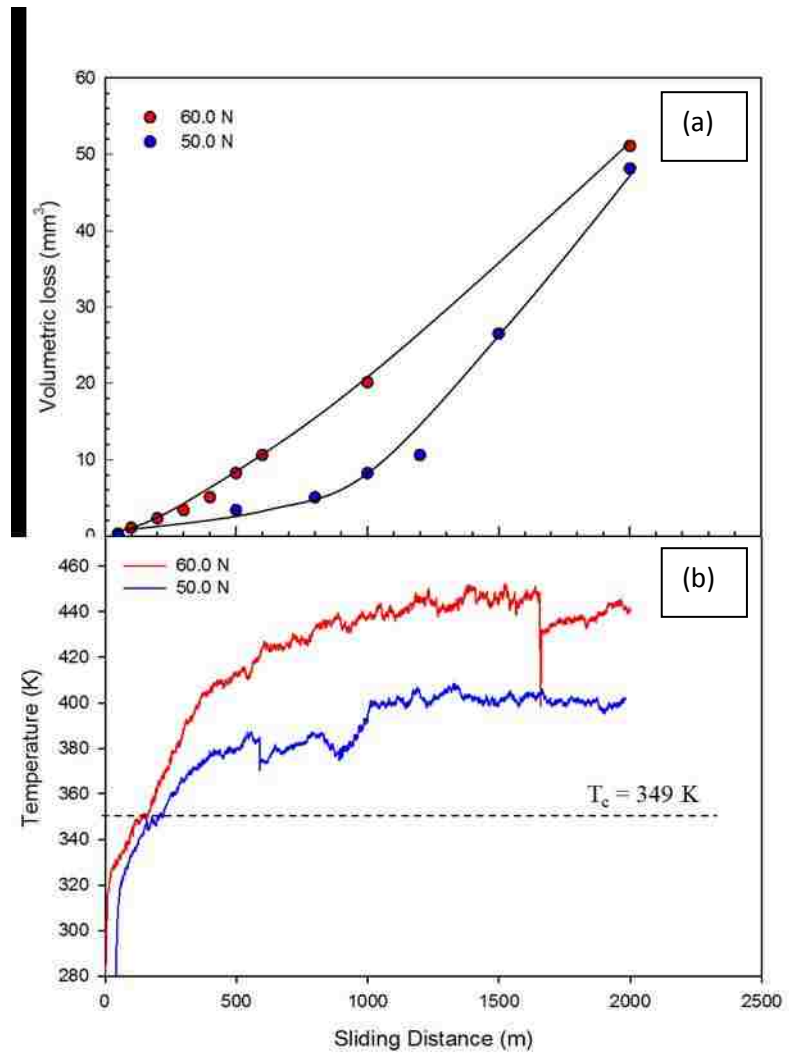
Figure 5.13. (a) Volumetric loss vs. sliding distance plot (b) Temperature plot for AM60-9% $(Al_2O_3)_f$ composite at 50.0 N and 60.0 N at 1.5 m/s.
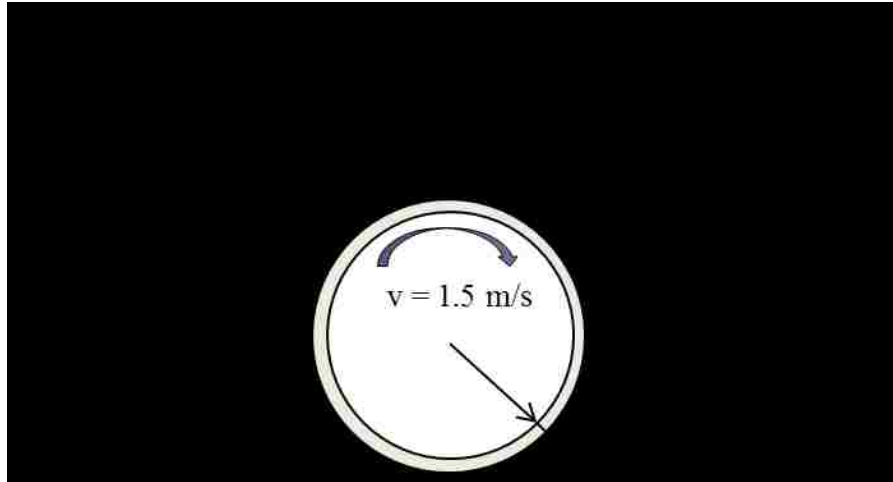
Figure 5.14.Scematic presentation of forced cooling experiment for AM60-9% $(Al_2O_3)_f$ composite at 60.0 N and 1.5 m/s
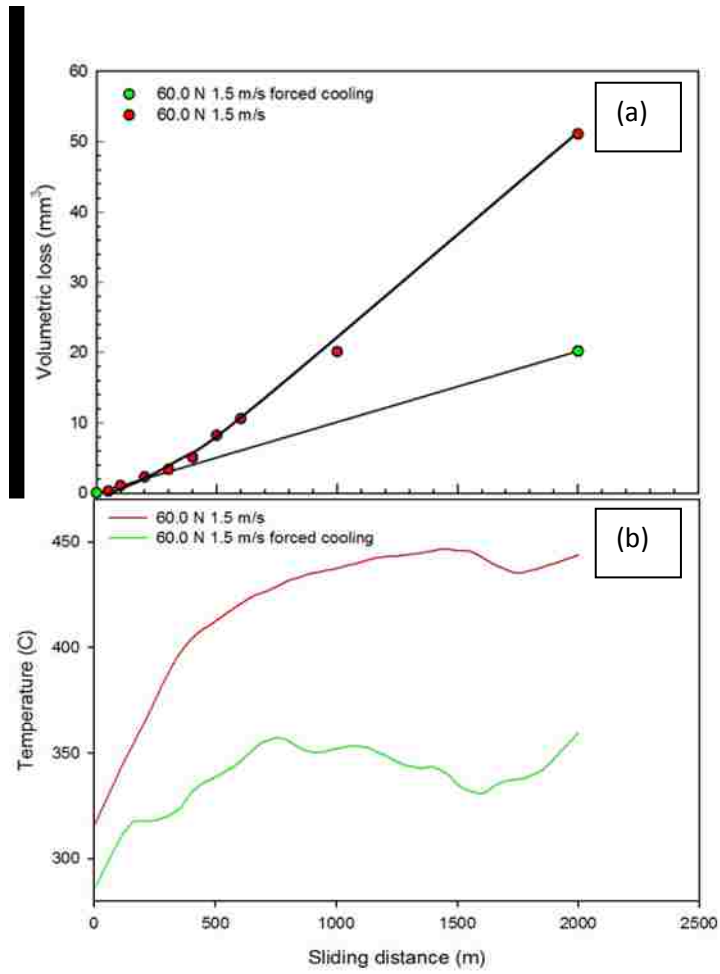
Figure 5.15.(a) Volumetric loss vs. sliding distance plot (b) Temperature plot for AM60-9% $(Al_2O_3)_f$ composite at 60.0 N and force-cooled 60.0 N at 1.5 m/s.

Chapter 6: Conclusions and future work

6.1. Conclusions

The aim of this study was to understand the wear behaviour of magnesium based materials AM60 alloy and AM60-9% $(Al_2O_3)_f$ composite under dry sliding condition to simulate the oil starvation condition in a running internal combustion (IC) engine, as the application of Mg based materials in the fabrication of IC engines and other powertrain components can facilitate the reduction of the weight of automotive vehicles. The dry sliding wear tests were performed to understand the damage mechanisms involved during the wear of these materials. Four wear regimes namely (i) low wear, (ii) mild wear, (iii) transient wear and (iv) severe wear were observed in which wear was controlled by various wear mechanisms. It was suggested that the transition from mild to severe wear regime was not abrupt and an intermediate wear regime existed which was termed as transient wear regime. Observations suggested that oxidational wear was operative under low and mild wear regimes while plastic deformation induced wear and melt wear were dominant wear mechanisms in transient and severe wear regimes respectively. It was suggested that the transition from mild to severe wear was controlled by bulk temperature of the specimens which was induced as a result of frictional heating. The transition from mild to severe wear occurred at 349 K and prevention of the rise of the bulk temperature above this critical transition temperature inhibited the transition, restricting the damage mechanism to the mild wear regime showing oxidational wear.

6.2. Future work

The construction of wear maps prompted the study of wear regimes and wear mechanisms operating under dry sliding conditions. This study helped in understanding the various wear mechanisms that operate under dry sliding condition for a range of load and velocity for Mg alloy AM60 and its composite AM60-9% $(Al_2O_3)_f$. However, further studies on the the following points would help in understanding the damage mechanisms which, in turn, would facilitate in further improvement of these materials:

i) Study of the wear behaviour of Mg alloys and composites under lubricated sliding condition and construction of lubricated sliding wear maps for these materials which can facilitate designers and engineers to predict the behaviour of these materials under normal running conditions in automotive engines and other powertrain components.

ii) Study the wear behaviour of Mg alloys and composites under dry and lubricated sliding condition against DLC coated counterface which will explain the wear behaviour of these materials against the DLC coated piston rings.

iii) Analyze the damage mechanisms under low loads and velocities to explain the damage mechanism and identify the presence of any intermediate regime that might exist between low wear and mild wear like the transient wear regime suggested in this study.

Original Contributions to Science and Technology

This work revealed the following aspects of the tribological behaviour of Mg based materials for the first time:

1. Besides the mild and severe wear regime, an intermediate wear regime called transient wear regime also existed which showed traits of mild and severe wear during the course of sliding. The traits of mild wear gradually diminished as the load and speed were increased and the transition to severe wear finally occurred.

2. Cooling the Mg composite sample during dry sliding tests showed characteristics of mild wear at the sliding parameters which would otherwise show transient or sever wear. This showed that cooling Mg composite components in dry sliding condition helps prevent the transition from mild to severe wear.

3. Mild and severe wear regimes were found to be able to be distinguished on the basis of roughness criterion. It was found that mild wear had an

References

[1] Cole, G. S., and A. M. Sherman. "Lightweight materials for automotive applications." Materials characterization 35.1 (1995) 3-9.

[2] Raynor, Geoffrey Vincent. The physical metallurgy of magnesium and its alloys.Vol. 5.Pergamon, 1959.

[3] Friedrich, H., and S. Schumann. "Research for a "New age of magnesium" in the automotive industry." Journal of Materials Processing Technology 117.3 (2001) 276-281.

[4] Aghion, E., B. Bronfin, and D. Eliezer. "The role of the magnesium industry in protecting the environment." Journal of Materials Processing Technology 117,3 (2001) 381-385.

[5] K Maruyama, M Suzuki, H Sato. Creep strength of magnesium-based alloys, Metall Mat Trans A Phys Metall Mat Sci. 33 (2002) 875-882.

[6] M.G. Fontana (Ed.), Corrosion Engineering, McGraw-Hill, New York, 1987, p. 71.

[7] ASM Failure, Analysis and Prevention, in: Metals Handbook, vol. 11, ASM, Metals Park, OH, 1986, p. 155.

[8] Majumdar, J. Dutta, D., Galun, R., Mordike, B. L., & Manna, I. "Effect of laser surface melting on corrosion and wear resistance of a commercial magnesium alloy." Materials Science and Engineering: A 361.1 (2003) 119-129.

[9] Lim, C. Y. H., S. C. Lim, and M. Gupta. "Wear behaviour of SiC p-reinforced magnesium matrix composites." Wear 255.1 (2003) 629-637.

[10] Tung, S. C., and S. Hartfield-Wünsch. "Advanced engine materials: current development and future trends." NIST (National Inst. of Science and Technology), Engine Materials and Tribology Workshop (1995) 4-7.

[11] Hill, Stephen H., Susan E. Hartfield-Wünsch, and Simon C. Tung. "Bench wear testing of common gasoline engine cylinder bore surface/piston ring combinations." Tribology transactions 39.4 (1996) 929-935.

[12] Jost K. Engine testing improves GM premium Vs. Automotive Engineering 1996 104(3):67

[13] Jaconsen EG. General motors 390 aluminum alloy 60 degree V6 engine. SAE paper no. 830006. Warrendale, PA: SAE; 1983.

[14] Ye, Haizhi. "An overview of the development of Al-Si-alloy based material for engine applications." Journal of Materials Engineering and Performance 12.3 (2003) 288-297.

[15] Kainer, Karl U., ed. Metal matrix composites: custom-made materials for automotive and aerospace engineering. John Wiley & Sons, 2006.

[16] Chafle, Girish B., et al. "Decentralized orchestration of composite web services."Proceedings of the 13th international World Wide Web conference on Alternate track papers & posters. ACM, 2004.

[17] Barbezat, Gérard. "Advanced thermal spray technology and coating for lightweight engine blocks for the automotive industry." Surface and Coatings Technology 200.5 (2005) 1990-1993.

[18] Bobzin, K., et al. "Coating bores of light metal engine blocks with a nanocomposite material using the plasma transferred wire arc thermal spray process." Journal of Thermal Spray Technology 17.3 (2008) 344-351.

[19] Kulekci, Mustafa Kemal. "Magnesium and its alloys applications in automotive industry." The International Journal of Advanced Manufacturing Technology39.9-10 (2008) 851-865.

[20] Blawert C, Hort N, Kainer KV (2004) Automotive applications of magnesium and its alloys. Trans Indian Inst Met 57(4) 397–408.

[21] Eliezer D, Aghion E, Froes FH (1998) Magnesium science and technology. Adv MatPerformance 5:201–212.

[22] Polmear, I. J.. (2006). Light Alloys - From Traditional Alloys to Nanocrystals (4th Edition), Chapter 5, "Magnesium Alloys".

[23] A Luo. Processing, microstructure, and mechanical behavior of cast magnesium metal matrix composites, Metallurgical and Materials Transactions A. 26 (1995) 2445-2455.

[24] Hu, H. "Squeeze casting of magnesium alloys and their composites." Journal of materials science 33.6 (1998) 1579-1589.

[25] Zhang, Xuezhi, Qiang Zhang, and Henry Hu. "Tensile behaviour and microstructure of magnesium AM60-based hybrid composite containing Al_2O_3 fibres and particles." Materials Science and Engineering: A 607 (2014) 269-276.

[26] Z Wang, RJ Zhang. Mechanical behavior of cast particulate SiC/AI (A356) metalmatrix composites, Metallurgical Transactions A. 22 (1991) 1585-1593.

[27] A Luo. Development of matrix grain structure during the solidification of a Mg (AZ91) SiCP composite, ScriptaMetallurgica et Materiala. 31 (1994) 1253-1258.

[28] EO Hall. Variation of hardness of metals with grain size [5], Nature. 173 (1954) 948-949.

[29] GE Dieter. Mechanical Metallurgy. JR. McGraw-Hill Book Company, INC. New York, Toronto, London 1961, 189.

[30] Zhang, Q., H. Hu, J Lo, Solidification of discontinuous Al 2O 3 fiber reinforced magnesium (AM60) matrix composite, Defect and Diffusion Forum. 312-315 (2011) 277-282.

[31] Zhang, X., Wang, M., Sun, Z., & Hu, H. "Section thickness-dependent tensile properties of squeeze cast magnesium alloy AM60." China Foundry 9.2 (2012) 122-125.

[32] Zhang, X., and H. Hu. "Solidification of Magnesium (AM50A)/vol%.SiCp composite." IOP Conference Series: Materials Science and Engineering. Vol. 27.No. 1.IOP Publishing, 2012.

[33] H. Fukuda, T. Chou. "An advanced shear-lag model applicable to discontinuous fiber composites", J.Composite Mater. 15 (1981) 179-191.

[34] V.C. Nardone, KM Prewo. "On the strength of discontinuous silicon carbide reinforced aluminum composites", ScriptaMetallurgica. 20 (1986) 43-48.

[35] Ye, H. Z., & Liu, X. Y. "Review of recent studies in magnesium matrix composites." Journal of materials science 39.20 (2004) 6153-6171.

[36] Ray, S. "MTech dissertation." Indian Institute of Technology, Kanpur (1969).

[37] Luo, A. "Processing, microstructure, and mechanical behavior of cast magnesium metal matrix composites." Metallurgical and Materials Transactions A 26.9 (1995) 2445-2455.

[38] Zhou, W., and Z. M. Xu. "Casting of SiC reinforced metal matrix composites."Journal of Materials Processing Technology 63.1 (1997) 358-363.

[39] Mikucki, B. A., Mercer, W. E., & Green, W. G. "Extruded magnesium alloys reinforced with ceramic particles" (No. 900533). SAE Technical Paper.

[40] Luthringer, B. J., Hort, N., & Feyerabend, F. "Metal Matrix Composites: Magnesium." Wiley Encyclopedia of Composites (2011).

[41] Inem B. and Pollard G., DGM Informations gesellschaft M.B.H., Germany, 1992, p. 439.

[42] T. E. WILKS and J .F .KING,DGM Informationsgesellschaft M.B.H., Germany, 1992, p. 431.

[43] N. HARNBY, M. F .EDWARD and A. W. NIENOW, "Mixing in Process Industries" (Butterworths, London, 1985).

[44] Luo, Alan, Renaud, J., Nakatsugawa, I., & Plourde, J. "Magnesium castings for automotive applications." Jom 47.7 (1995): 28-31.

[45] Yue, T. M., & Chadwick, G. A. "Squeeze casting of light alloys and their composites." Journal of materials processing Technology 58.2 (1996): 302-307.

[46] Murthy G. R. K. and Satyanarayan K. R., Trans.Indian Inst. Met.41(1) (1988) 65.

[47] Yong M. S . and Clegg A. J ., Foundryman March (1999) 71.

[48] Surappa M. K., J. Mater. Proc. Tech. **63** (1997) 325.

[49] Rabinowicz, E. "The relation between friction and wear for boundary-lubricated surfaces." Proceedings of the Physical Society. Section B 68.9 (1955) 603.

[50] JF Archard, W Hirst. "The Wear of Metals under Unlubricated Conditions", Proceedings of the Royal Society of London.Series A, Mathematical and Physical Sciences.236 (1956) 397-410.

[51] Tabor, David. "Status and direction of tribology as a science in the 80s."Proceedings of the International Conference Tribology in the 80s, NASA Lewis Research Centre, Cleveland, Ohio. 1983.

[52] Lim, S. C., and M. F. Ashby. "Overview no. 55 wear-mechanism maps." Actametallurgica 35.1 (1987): 1-24.

[53] Ashby, M. F., J. Abulawi, and H. S. Kong. "Temperature maps for frictional heating in dry sliding." Tribology Transactions 34.4 (1991): 577-587.

[54] Welsh, N. C. "Frictional heating and its influence on the wear of steel." Journal of Applied Physics 28.9 (1957): 960-968.

[55] Zhang, J., and A. T. Alpas. "Wear regimes and transitions in Al 2 O 3 particulate-reinforced aluminum alloys." Materials Science and Engineering: A161.2 (1993): 273-284.

[56] Alpas, A. T., and J. Zhang. "Effect of microstructure (particulate size and volume aluminum matrix composites." Metallurgical and Materials Transactions A 25.5 (1994): 969-983.

[57] J Zhang, AT Alpas. "Transition between mild and severe wear in aluminium alloys", ActaMaterialia. 45 (1997) 513-528.

[58] M Elmadagli, T Perry, AT Alpas. "A parametric study of the relationship between microstructure and wear resistance of Al-Si alloys", Wear. 262 (2007) 79-92.

[59] M Elmadagli, AT Alpas. "Progression of wear in the mild wear regime of an Al-18.5% Si (A390) alloy", Wear. 261 (2006) 367-381.

[60] Chen, H., and A. T. Alpas. "Sliding wear map for the magnesium alloy Mg-9Al-0.9 Zn (AZ91)." Wear 246.1 (2000) 106-116.

[61] H. Chen, Ph.D. Thesis "Tribological behaviour of Mg-9.0% Al-0.9% Zn alloy (AZ91) and composite AZ91+10%SiC$_p$", 1999, University of Windsor.

[62] Riahi, A. R., and A. T. Alpas. "Wear map for grey cast iron." Wear 255.1 (2003): 401-409.

[63] Baker, H. "Magnesium races ahead." Advanced materials & processes 136.3 (1989): 35-42.

[64] Evans, G. B. "Applications of magnesium in aerospace." Magnesium technology(1986) 103-109.

[65] Das, S., A. T. Morales, and A. T. Alpas. "Microstructural evolution during high temperature sliding wear of Mg–3% Al–1% Zn (AZ31) alloy." Wear 268.1 (2010) 94-103.

[66] Sharma, S. C., B. Anand, and M. Krishna. "Evaluation of sliding wear behaviour of feldspar particle-reinforced magnesium alloy composites." Wear 241.1 (2000): 33-40.

[67] Alahelisten, A., Bergman, F., Olsson, M., & Hogmark, S. "On the wear of aluminium and magnesium metal matrix composites." Wear 165.2 (1993) 221-226.

[68] Alpas, A. T., and J. Zhang. "Effect of SiC particulate reinforcement on the dry sliding wear of aluminium-silicon alloys (A356)." wear 155.1 (1992) 83-104.

[69] Zhang, Z. F., L. C. Zhang, and Y. W. Mai. "Wear of ceramic particle-reinforced metal-matrix composites." Journal of materials science 30.8 (1995) 1967-1971.

[70] Lim, C. Y. H., et al. "Wear of magnesium composites reinforced with nano-sized alumina particulates." Wear 259.1 (2005) 620-625.

[71] Banerji, A., H. Hu, and A. T. Alpas. "Sliding wear mechanisms of magnesium composites AM60 reinforced with Al_2O_3 fibres under ultra-mild wear conditions." Wear 301.1 (2013) 626-635.

[72] Ling, F. F., and Edward Saibel. "On kinetic friction between unlubricated metallic surfaces." Wear 1.3 (1957) 167-172.

[73] Singh, J., and A. T. Alpas. "High-temperature wear and deformation processes in metal matrix composites." Metallurgical and Materials Transactions A 27.10 (1996) 3135-3148.

[74] Kuo, S. M., and D. A. Rigney. "Sliding behavior of aluminum." Materials Science and Engineering: A 157.2 (1992) 131-143.

Vita Auctoris

Name:	Muhammad Zafar Ullah Khan
Place of Birth:	Karachi, Sindh, Pakistan
Year of Birth:	1988
Eductaion:	Bachelor of Engineering (B.E.), Materials Engineering, NED University of Engineering and Technology (NEDUET), Karachi, Sindh, Pakistan. 2007-2010.
	Master of Applied Science (M.A.Sc.), Engineering Materials, University of Windsor, Windsor, Ontario, Canada. 2013-2015.